Neuchâtel University
Physics Department

Thesis presented for the Degree of
Doctor ès Sciences

Developments for double-beta-decay techniques, related to the EXO experiment

Patrick Weber

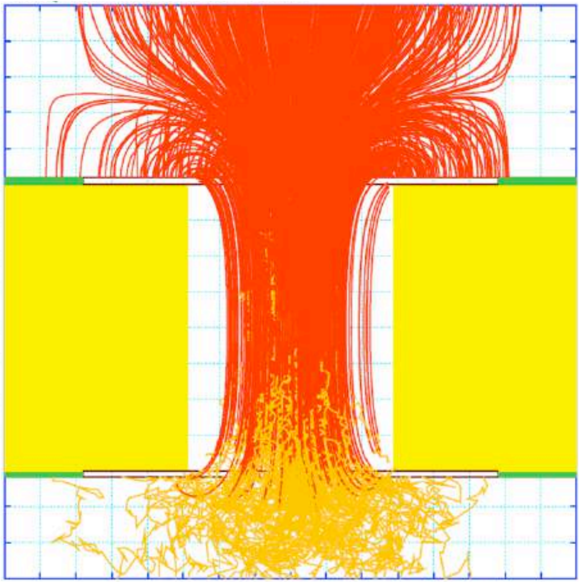

Thesis presented on December 21, 2006, to the jury, composed by :

Prof. Dr. J-L. Vuilleumier (Thesis advisor); Neuchâtel University
Dr. F. Juget; Neuchâtel University
PD. Dr. D. Twerenbold; METAS and Neuchâtel University
Dr. R. Luescher; CCLRC Rutherford Appleton Laboratory
Prof. Dr. R. De Voe; Stanford University

Université de Neuchâtel unine

FACULTE DES SCIENCES
Secrétariat-Décanat de la faculté
- Rue Emile-Argand 11
- CP 158
- CH-2009 Neuchâtel

IMPRIMATUR POUR LA THESE

Developments for double-beta-decay techniques related to the EXO experiment

Patrick WEBER

UNIVERSITE DE NEUCHATEL

FACULTE DES SCIENCES

La Faculté des sciences de l'Université de Neuchâtel,
sur le rapport des membres du jury

MM. J.-L. Vuilleumier (directeur de thèse),
D. Twerenbold, F. Juget,
R. Luscher (Chilton Didcot, UK)
et R.G. de Voe (Stanford University, USA)

autorise l'impression de la présente thèse.

Neuchâtel, le 3 mai 2007

Le doyen :
T. Ward

UNIVERSITE DE NEUCHATEL
FACULTE DES SCIENCES
Secrétariat-décanat de la faculté
Rue Emile-Argand 11 - CP 158
CH-2009 Neuchâtel

Ward

A Capucine, à Mahé

Abstract

This thesis work has been done in the Particles Physics Group from Neuchâtel University and within the EXO international collaboration. It presents the EXO experiment current status and the contributions from Neuchâtel to this neutrino experiment.
EXO — acronym for Enriched Xenon Observatory for double-beta decay — is aimed to study the intrinsic behavior of neutrino, particularly their Majorana or Dirac nature and moreover measure their incredibly small but non-vanishing mass. Neuchâtel played a significant role in the detector prototype development, named EXO-200, which is now almost ready for data taking and in the $\beta\beta$ event identification for the final version.

Key words : Double-Beta Decay — Neutrino Physics

Mots Clés : Désintégration Beta Double — Physique du Neutrino

Table of Contents

List of Figures

List of Tables

Introduction

This thesis work reports on several developments made for double-beta decay experiments, directly or indirectly related to EXO :

Chapter 1 gives a brief overview of the present knowledge in neutrino physics, and explains in particular neutrinoless double-beta decay, which motivates the EXO experiment.

Chapter 2 gives a general introduction of the EXO experiment, the current status of the prototype construction — called EXO-200 — as well as the developments made for the final version, which should be equipped with a barium ion identification system, allowing a background-free measurement of every double-beta decay events.

Chapter 3 presents a possible way to build a radioactive ^{137}Ba ions source. A barium source is necessary to test the barium tagging process, and the radioactivity of this source allows a live observation of the different tagging phases.

Chapter 4 describes the development of a new electron amplification system for Time Projection Chamber detectors (TPC), combined with an $x - y$ readout plane. This could be useed in a gaseous version of the final EXO detector. Its robustness, ability to build a large grid and energy resolution around the percent at 2 MeV, are valuable assets for large gaseous TPCs, and particularly in the case of double-beta decay detectors.
This chapter includes also a section dedicated to secondary scintillation detection with an optical fibers array. Secondary scintillation measurement is complementary to the charge measurement on the amplification grid.

Chapter 5 reports on germanium gamma analysis of samples for EXO-200 detector construction. It presents the germanium detector characteristics and abilities, as well as the radioactivity calculation method for the different isotopes.

Chapter 6 shows an application of germanium gamma countings dedicated to meteorites analysis. Some meteorites were measured in our detector, leading to interesting results on meteorites terrestrial ages and initial position of fragments from the original meteorite. This newly built collaboration with Bern University is ongoing.

Chapter 1

Neutrino overview, double-beta decay

Neutrino physics lies in a thrilling period. Results from the last decade showed evidence of predicted theoretical models, and opened the way to new exciting perspectives. Neutrino properties are not known in detail yet, but oscillation experiments demonstrated that masses and mixings are non vanishing, in particular neutrino mass has only upper limits. Neutrino physics can be seen also as a probe for weak interaction and physics beyond the particles standard model. The challenge for the coming years in neutrino physics will be

- θ_{13} precision measurement
- Neutrino mass scale
- Neutrino nature (*Majorana* or *Dirac*)
- Neutrino hierarchy

θ_{13} precision measurements can be done with oscillation experiments, with or without neutrino factories, depending on the amplitude of this value. Double-beta decay is the most promising way to explore the neutrino mass scale and neutrino nature. Hierarchy is measured in β and $\beta\beta$ experiments.

1.1 Neutrinos

The theoretical framework of neutrino oscillations is described in the lepton mixing matrix [1] :

$$\nu_l = U_{PMNS} \cdot \nu_i \ (l = e, \mu, \tau; i = 1, 2, 3)$$

$$\begin{pmatrix} \nu_e \\ \nu_\mu \\ \nu_\tau \end{pmatrix} = \begin{pmatrix} c_{12}c_{13} & s_{12}c_{13} & s_{13}e^{-i\delta} \\ -s_{12}c_{23} - c_{12}s_{23}s_{13}e^{i\delta} & c_{12}c_{23} - s_{12}s_{23}s_{13}e^{i\delta} & s_{23}c_{13} \\ s_{12}s_{23} - c_{12}c_{23}s_{13}e^{i\delta} & -c_{12}s_{23} - s_{12}c_{23}s_{13}e^{i\delta} & c_{23}c_{13} \end{pmatrix} \begin{pmatrix} e^{i\alpha_1/2}\ \nu_1 \\ e^{i\alpha_2/2}\ \nu_2 \\ \nu_3 \end{pmatrix}$$

Weak interaction eigenstates $\nu_l, l = e, \mu, \tau$ are linear combinations of mass eigenstates $\nu_i, i = 1, 2, 3$. The Pontecorvo, Maki, Nakagawa and Sakata matrix (U_{PMNS})

is unitary, s is used for sine and c for cosine. For 3 neutrinos, the mixing matrix is parametrized by 3 angles θ_{12}, θ_{13} and θ_{23}, one CP-violating phase δ and two Majorana phases α_1, α_2. This neutrino mixing matrix is similar to the quark mixing matrix, although for the case of quarks, interaction eigenstates are also mass eigenstates.

U_{PMNS} matrix can be factorized into

$$U = \underbrace{\begin{pmatrix} 1 & 0 & 0 \\ 0 & c\theta_{23} & s\theta_{23} \\ 0 & -s\theta_{23} & c\theta_{23} \end{pmatrix}}_{\substack{Atmospheric \\ K2K, Minos \\ \theta_{23} \sim 45^o}} \underbrace{\begin{pmatrix} c\theta_{13} & 0 & e^{-i\delta} s\theta_{13} \\ 0 & 1 & 0 \\ -e^{-i\delta} s\theta_{13} & 0 & c\theta_{13} \end{pmatrix}}_{\substack{CHOOZ, Palo\ Verde \\ Off\ axis, \nu\ factories \\ \theta_{13} < 7^o\ (90\%\ C.L.)}} \underbrace{\begin{pmatrix} c\theta_{12} & s\theta_{12} & 0 \\ -s\theta_{12} & c\theta_{12} & 0 \\ 0 & 0 & 1 \end{pmatrix}}_{\substack{Solar \\ KamLAND \\ \theta_{12} \sim 32^o}} \underbrace{\begin{pmatrix} 1 & 0 & 0 \\ 0 & e^{-i\alpha_1/2} & 0 \\ 0 & 0 & e^{-i\alpha_2/2} \end{pmatrix}}_{0\nu\beta\beta}$$

1.2 Neutrino oscillations

In vacuum, the probability for a transition $l \rightarrow l'$ is given by [2]

$$P(\nu_l \rightarrow \nu_{l'}) = \Big| \sum_i U_{li} U^*_{l'i} e^{-i(m_i^2/2E)L} \Big|^2$$

For two flavors mixing, this becomes

$$P(\nu_l \rightarrow \nu_{l'}) = sin^2(2\theta)\ sin^2\Big[1.27\Delta m^2(eV^2)\frac{L_{osc}(km)}{E_\nu(GeV)}\Big]$$

When neutrinos travel in matter, all active neutrino (and antineutrino) flavors interact with matter by neutral current (NC, exchange of Z^0 boson) and only ν_e (and $\overline{\nu}_e$) interact by charged current (CC) with $W^\pm$ exchange. An additionnal contribution to the phase appear in this case, leading to corrections on $P(\nu_l \rightarrow \nu_{l'})$. Moreover, CP conservation implies $P(\nu_l \rightarrow \nu_{l'}) = P(\overline{\nu}_l \rightarrow \overline{\nu}_{l'})$, but matter effects can induce inequality, so one has to be careful in data analysis. It is interesting to notice that CP-violation disappear if $\theta_{13} = 0$, and it will be difficult to measure any CP-violating effect if θ_{13} has non-zero value but very close to zero.

Neutrino oscillation experiments are classified into atmospheric, solar, reactor, accelerator and cosmology experiments.

1.2.1 Atmospheric neutrinos

Super-Kamiokande measured the ν_μ and ν_e fluxes from the atmospheric $\pi^\pm$ decay

$$\pi^+ \rightarrow \mu^+ + \nu_\mu$$

$$\mu^+ \rightarrow e^+ + \nu_e + \overline{\nu}_\mu$$

(π^- and μ^- decay are charge conjugates of the above relations). The ν_μ/ν_e ratio was expected to be ~ 2, but Super-Kamiokande measured $\nu_\mu/\nu_e \sim 1$, which was a first evidence of $\nu_e \rightarrow \nu_\mu$ flavour oscillation.

1.2.2 Solar neutrinos

Numerous oscillations experiments progressively constrained neutrino properties to tight values. The neutrino hierarchy is not yet established, however. Normal hierarchy is defined as $m_1 \approx m_2 \ll m_3$, while inverted hierarchy is $m_1 \approx m_2 \gg m_3$ and finally the degenerate case is set as $m_1 \approx m_2 \approx m_3$. Fig (1.1) illustrates the different possibilities.

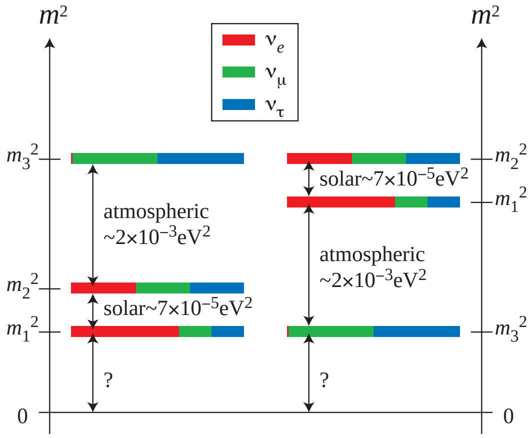

Figure 1.1: Normal and Inverted hierarchy cases.

In 2002, SNO gave an irrefutable proof of solar neutrino oscillations by resolving the 30 years old solar neutrino problem. SNO collaboration compared neutrino-deuterium interactions by charged current (CC), occuring only for ν_e with matter (e^-) and neutral current (NC), where all neutrino flavors $l = e, \mu, \tau$ contribute.

$$\nu_e + d \rightarrow e^- + 2p \ (CC)$$

$$\nu_l + d \rightarrow \nu_l + p + n \ (NC)$$

with $l = e, \mu, \tau$. The total neutrino flux ($\nu_e + \nu_\mu + \nu_\tau$) — determined by NC interactions — is compatible with the Standard Solar Model (SSM) prediction, but ν_e flux — determined by CC interactions — is supressed Fig(1.2).

$$\frac{\Phi_{CC}}{\Phi_{NC}} = \frac{\Phi_{\nu_e}}{\Phi_{\nu_e+\nu_\mu+\nu_\tau}} = 0.036 \pm 0.026^{(stat)} \pm 0.024^{(syst)}$$

.

SNO leads to large mixing angle $\theta_{12} = 32.5^{+2.4}_{-2.3}$ and $\Delta m^2_{12} = 7.1^{+2.1}_{-0.6}\ 10^{-5} eV^2$. KamLAND observed antineutrino oscillations. The oscillation distance had to be $\sim 200 km$ to be sensitive to the solar parameters.

Figure 1.3 shows a compilation of various solar neutrino experiments and Figure 1.4 shows the precise solar neutrino parameters.

Other experiments are under preparation to lower the sensitivity on neutrino parameters and to investigate the $\nu_\mu \rightarrow \nu_\tau$ oscillation channel (OPERA)

Table 1.1 summarizes the most recent parameters from neutrino oscillations experiments.

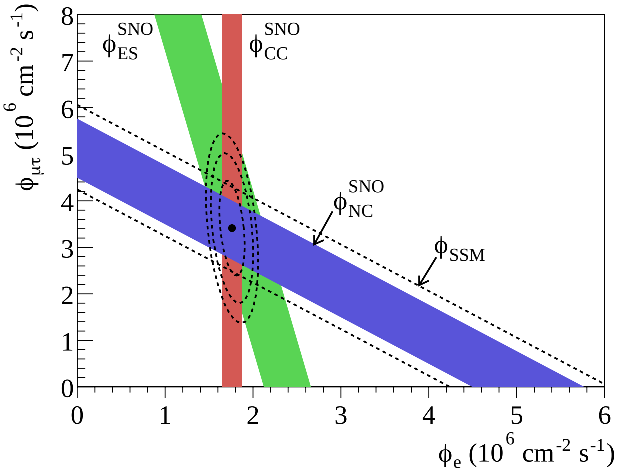

Figure 1.2: Measured solar neutrino fluxes for NC and CC from SNO. Elastic scattering events (ES) and SSM predictions are also represented.

Parameter	Value $\pm 1\sigma$	Comment
Δm^2_{12}	$7.1^{+1.2}_{-0.6}\ 10^{-5}\ eV^2$	For $\theta_{13} = 0$
θ_{12}	$32.5^{+2.4}_{-2.3}$	
$\|\Delta m_{32}\|^2$	$2.0^{+0.6}_{-0.4}\ 10^{-3}\ eV^2$	
$sin^2(2\theta_{23})$	> 0.94	For $\theta_{13} = 0$
$sin^2(2\theta_{13})$	< 0.11	For $\Delta m^2_{atm} = 2\ 10^{-3} eV^2$

Table 1.1: Latest results from neutrino oscillation experiments.

1.3 Direct mass measurements

A non-vanishing neutrino mass modifies the phase space and leads to a change of the electron spectrum near endpoint, as shown on Figure 1.5.

Direct electron neutrino mass measurements can be achieved with beta-decay experiments. However, several aspects have to be considered; The number of electrons with an energy close to the endpoint is small, that's why isotopes with low Q-values, such as tritium, are needed. Tritium decay is

$$^3H \rightarrow ^3 He + e^- + \overline{\nu}_e$$

But even in tritium case, only a fraction of 10^{-9} of all electrons have an energy 20 eV below the endpoint. Moreover, a good energy resolution is needed.
Mainz and Troitzk experiments — after resolving the negative squared neutrino mass due to experimental unknown systematic effects — raised to the results

$$m^2_\nu = -1.2 \pm 2.2^{(stat)} \pm 2.1^{(syst)}\ eV^2 \rightarrow m_{\nu_e} < 2.2\ eV(95\%C.L)\ Mainz$$

$$m^2_\nu = -2.3 \pm 2.5^{(stat)} \pm 2.0^{(syst)}\ eV^2 \rightarrow m_{\nu_e} < 2.2\ eV(95\%C.L)\ Troitzk$$

Next generation spectrometer-based detectors, such as KATRIN, are designed to lower the sensitivity down to $m_{\overline{\nu}_e} \sim 0.2\ eV$, exploring mainly the degenerate

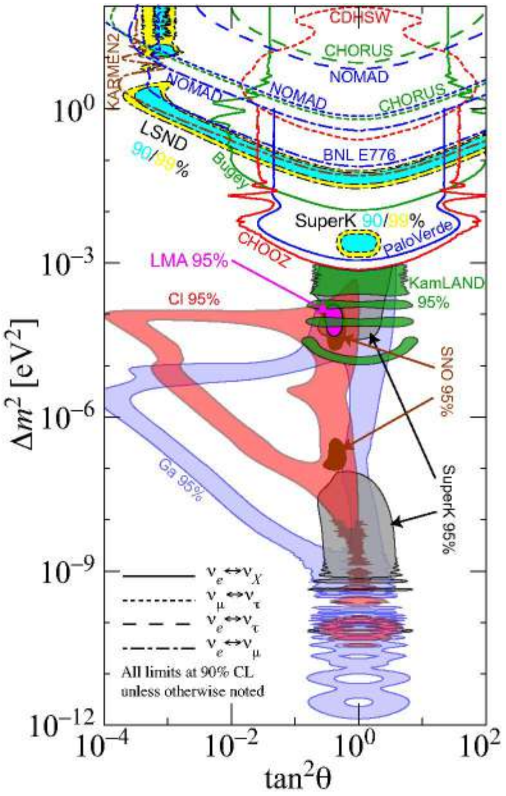

Figure 1.3: Solar neutrino parameters from various solar experiments [4]

hierarchy case, as one can see on Figure 3.3.
Limits on muon neutrino can be obtained by measuring pion decay. Neutrino mass is then

$$m^2_{\nu_\mu} = m^2_{\pi^+} + m^2_{\mu^+} - 2m_{\pi^+} + \sqrt{p^2_{\mu^+} + m^2_{\mu^+}}$$

Precision measurements on π-decay have been performed at PSI, leading to

$$m_{\nu_\mu} < 190\ keV\ (90\%\ C.L)$$

Limits on tau neutrino mass has been studied at ALEPH and other LEP experiments with reaction $e^+e^- \rightarrow \tau^+\tau-$. And

$$\tau \rightarrow \nu_\tau + 5\pi^\pm(\pi^0)$$

Combined ALEPH and LEP experiments lead to

$$m_{\nu_\tau} < 15.5\ MeV$$

1.4 Cosmic neutrinos

Cosmological constraints on neutrino mass can be deduced from observation of cosmic microwave background (CMB) and matter distribution in the universe. When

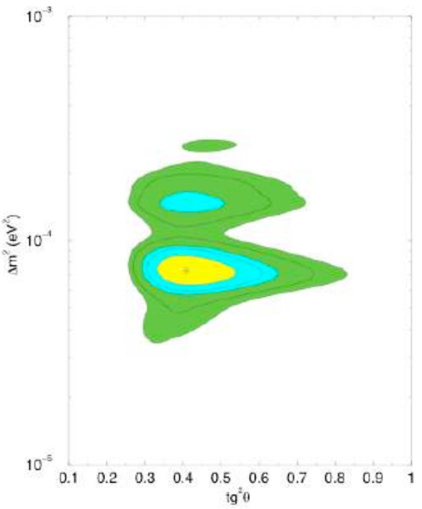

Figure 1.4: Solar neutrino parameters from solar experiments (SNO, KamLAND, etc).

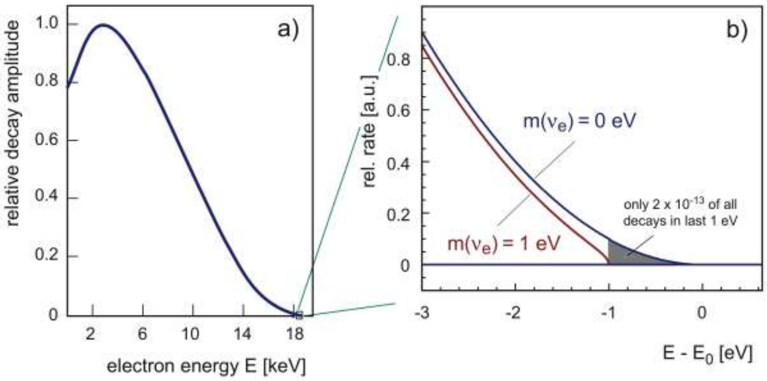

Figure 1.5: Electron sum spectrum near endpoint.

universe temperature was $T > 1MeV$, weak interactions occur with high rate due to high matter density. This lead to a large neutrino density. When the universe cooled down, the weak interaction rate decreased and neutrinos decoupled from matter. $\sim 10^5$ years later, the universe cooled enough so that atoms formed and radiation decoupled from matter. The presently observed radiation distribution (WMAP) — the CMB power spectra in particular — and the density fluctuations of matter distribution in the Universe (2dFGRS) are sensitive to massive neutrinos. Combined WMAP and 2dFGRS analysis lead to

$$\sum_i m_\nu^i < 0.7\ eV\ (95\%\ C.L)$$

[7] Another limit of $\sum_i m_\nu^i < 1.0\ eV$ is given in the litterature [8]; those limits depend on values given with errors, such as Hubble constant, bias, etc.

WMAP and 2dFGRS data cannot rule out neither the evidence of neutrinoless double-beta decay from Heidelberg-Moscow experiment, nor the LSND result. Moreover, when Big-Bang Nucleosynthesis (BBN) constraints are added to the data, the

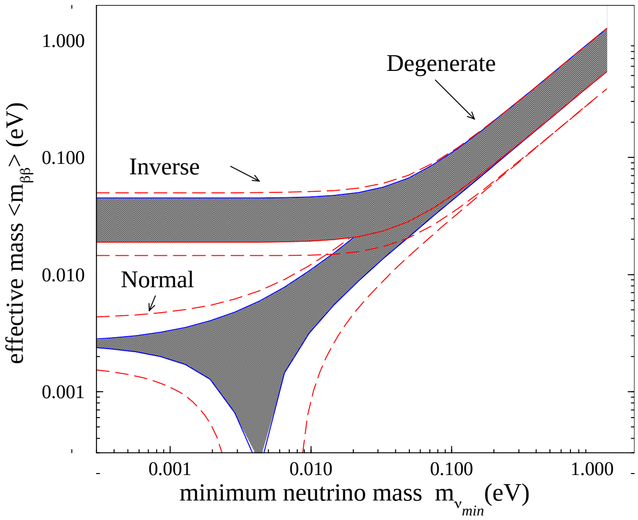

Figure 1.6: Effective neutrino mass, as a function of the absolute mass of the lightest neutrino [5].

number of active neutrinos is bound [8] :

$$N_\nu = 2.6^{+0.4}_{-0.3} \; (95\% \; C.L)$$

1.5 Double-beta decay

1.5.1 Theoretical framework

Double beta decay with two neutrinos ($2\nu\beta\beta$) is a rare transition occuring in some nuclei, described by [6]

$$(A, Z) \rightarrow (A, Z + 2) + 2e^- + 2\overline{\nu}_e$$

This decay occurs only if the initial nucleus is less bound than the final one, but both must be more bound than the intermediate one. This condition is fulfilled only for some even-even nuclei. The example of ^{136}Xe is shown on Figure 3.4. ^{136}Xe can decay under double-beta, but is stable under simple beta decay.

Double-beta decay of many nuclei have been measured, with $T_{1/2} \sim 10^{20}\ years$. $2\nu\beta\beta$ observations allows to constrain the nuclear matrix elements. Large Q-values are advantageous since the rate scales $\sim Q^5$ and background suppression is easier for larger Q. Table 1.2 is a compilation of $\beta\beta$ emitters with Q-values above 2 MeV [3].

Neutrinoless double-beta decay ($0\nu\beta\beta$) is also assumed to happen — if the masses are of the Majorana type — as :

$$(A, Z) \rightarrow (A, Z + 2) + 2e^-$$

Leptonic number is violated in $0\nu\beta\beta$ and moreover, neutrino and antineutrino are the same particle (Majorana particles). $0\nu\beta\beta$ decay is thus physics beyond the particles Standard Model.

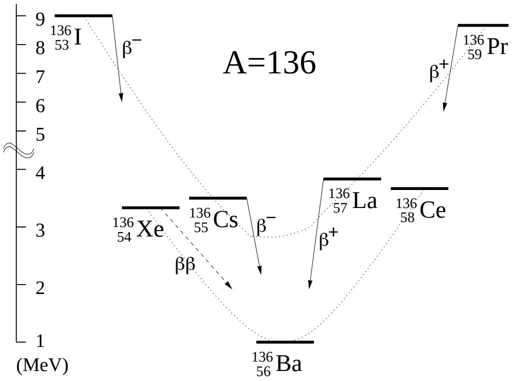

Figure 1.7: β and 2β decays for nuclei with $A = 136$.

Transition	Q-value (keV)	Nat ab (%)	$[G^{0\nu}]^{-1}$ (yr)	$[G^{0\nu}]^{-1}$ (yr)
$^{48}Ca \rightarrow^{48} Ti$	4271	0.19	4.10 10^{24}	2.52 10^{16}
$^{76}Ge \rightarrow^{76} Se$	2039	7.8	4.09 10^{25}	7.66 10^{18}
$^{82}Se \rightarrow^{82} Kr$	2995	9.2	9.27 10^{24}	9.27 10^{24}
$^{96}Zr \rightarrow^{96} Mo$	3350	2.8	4.46 10^{24}	5.19 10^{16}
$^{100}Mo \rightarrow^{100} Ru$	3034	9.6	5.70 10^{24}	1.06 10^{17}
$^{110}Pd \rightarrow^{110} Cd$	2013	11.8	1.86 10^{25}	2.51 10^{18}
$^{116}Cd \rightarrow^{116} Sn$	2802	7.5	5.28 10^{24}	5.28 10^{24}
$^{124}Sn \rightarrow^{124} Te$	2288	5.6	9.48 10^{24}	5.93 10^{17}
$^{130}Te \rightarrow^{130} Xe$	2533	34.5	5.89 10^{24}	2.08 10^{17}
$^{136}Xe \rightarrow^{136} Ba$	2479	8.9	5.52 10^{24}	2.07 10^{17}
$^{150}Nd \rightarrow^{150} Sm$	3367	5.6	1.25 10^{24}	8.41 10^{15}

Table 1.2: $\beta\beta$ emitters with Q-value above 2 MeV

Experiments are trying to measure this decay; a first $0\nu\beta\beta$ experimental evidence was obtained in the Heidelberg-Moscow experiment. However, this result is subject to some controversy. New $\beta\beta$ experiments — and EXO in particular — will be performed to confirm (or infirm) it. Experimental study of neutrinoless double-beta decay is the most sensitive tool to study the Majorana nature of neutrinos and next generation $0\nu\beta\beta$ decay experiments, like EXO, should be able to reach the absolute scale of neutrino masses.

In a field theory of neutrinos, the mass comes from the mass term in the Lagrangian

$$-L_m = M^D_{il}\overline{\nu}_{iR}\nu_{lL} + \frac{1}{2}M^M_{ij}\overline{\nu}_{iR}\nu^c_{jR} + h.c.$$

The first term of the lagrangian is the Dirac term, conserving the total lepton number, while the second term is the Majorana term, violating the total lepton number by two units. Observed neutrinos are always left-handed (antineutrinos always right-handed). Big-Bang nucleosythesis, as well as LEP, constrain active neutrino flavors to 3. If we assume n sterile neutrinos, one can define

$$-L_M = \frac{1}{2}\overline{\nu}^c M_\nu \nu + h.c.$$

with

$$\nu = \begin{pmatrix} \nu_{lL} \\ \nu j R^c \end{pmatrix} \quad M_\nu = \begin{pmatrix} 0 & M^D \\ (M^D)^T & M^M \end{pmatrix}$$

M_ν has $3+n$ eigenstates ν_i, representing Majorana neutrinos. Let one discuss three different cases [6]

- M^M is very large $\Longrightarrow$ 3 light active Majorana neutrinos. In this case, called Seesaw mechanism, the very tiny neutrino mass comes from the large Majorana scale.
- M^M comparable to electroweak symmetry breaking scale $\Longrightarrow$ possibility to have more than 3 light Majorana neutrinos, mixings of active and sterile.
- $M^M = 0 \Longrightarrow$ 3 Dirac neutrinos.

Double-beta decay changes two neutrons into two protons in a nucleus. This process involves the exchange of virtual particles that can be Majorana neutrinos of course, but also right-handed current mediating W_R boson, Supersymmetric patricles, etc. In any case, $0\nu\beta\beta$ decay occurs only if neutrinos are massive Majorana neutrinos. For the case where $0\nu\beta\beta$ is mediated by the exchange of light Majorana neutrinos in the left-handed $V-A$ current, the decay rate is :

$$[T^{0\nu}_{1/2}(0^+ \to 0^+)]^{-1} = G^{0\nu}(Q,Z)\left| M^{0\nu}_{GT} - \frac{g_V^2}{g_A^2} M^{0\nu}_F \right|^2 \langle m_{\beta\beta} \rangle$$

where $G^{0\nu}$ is the phase space factor, calculable with precision, $M^{0\nu}_{GT}$ and $M^{0\nu}_F$ the Gamov-Teller and Fermi transitions nuclear matrix elements respectively and $\langle m_{\beta\beta} \rangle$ the effective neutrino mass

$$\langle m_{\beta\beta} \rangle = \left| \sum_i |U^2_{ei}| m_{\nu_i} e^{i\alpha_i} \right|$$

$T^{0\nu}_{1/2}$ is measured in an experiment; this sensitivity is approximately given by :

$$T^{0\nu}_{1/2} \sim a \sqrt{\frac{M\ t}{B\ \Delta E}}$$

where a is the isotopic abundance of the $0\nu\beta\beta$ emitter, M is the detector fiducial mass, t the measuring time, B the background index and ΔE the energy resolution at $0\nu\beta\beta$ peak position.
Uncertainty on the effective neutrino mass $\langle m_{\beta\beta} \rangle$ comes from the spread (of a factor ~ 3) in the different calculation methods used for the matrix elements.

For measured $2\nu\beta\beta$, the decay rate is

$$[T^{2\nu}_{1/2}(0^+ \to 0^+)]^{-1} = G^{2\nu}(Q,Z)\left|M^{2\nu}_{GT} + \frac{g_V^2}{g_A^2} M^{2\nu}_F\right|^2$$

One can notice that $2\nu\beta\beta$ decay is insensitive to neutrino mass.

1.5.2 Experimental results

The output signal in the sum energy spectrum of both electrons for $2\nu\beta\beta$ decay is a continous spectrum, as shown on Figure 1.8, while for neutrinoless $0\nu\beta\beta$ decay it is a peak at the Q value of the transition.

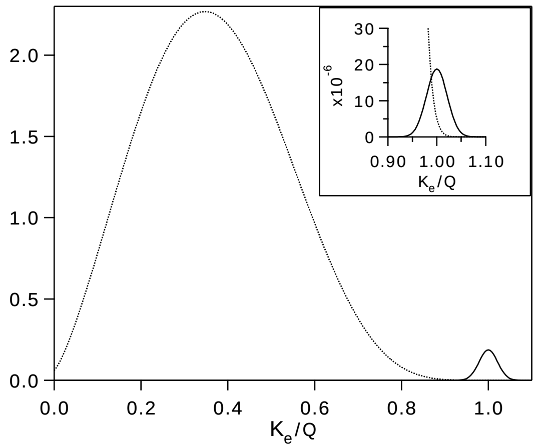

Figure 1.8: Illustration of $2\nu\beta\beta$ decay (dotted line, normalized to 1) and $0\nu\beta\beta$ decay (solid line) spectra, as a function of K_e, electron kinetic energy.

Numerous double-beta experiments measured the $2\nu\beta\beta$ spectrum since $2\nu\beta\beta$ decay first evidence with 36 events in 1987. NEMO-3 and other experiments collected thousands of double-beta events, as shown on NEMO-3 $2\nu\beta\beta$ spectrum (Figure 3.8).

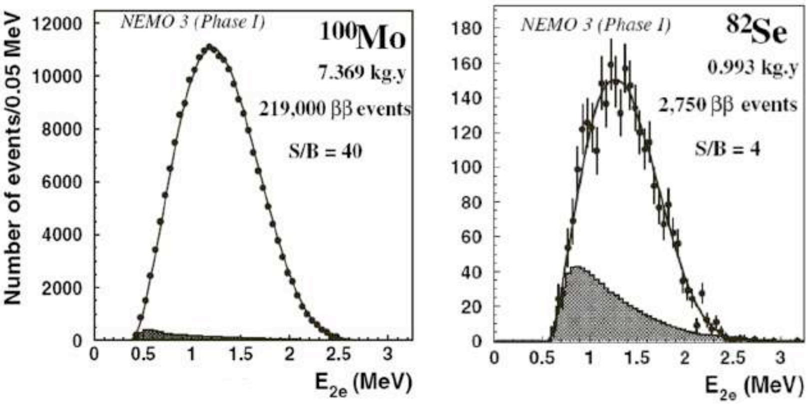

Figure 1.9: NEMO-3 energy sum spectrum of the two electrons for ^{100}Mo and^{82}Se double beta decays.

Transition	$T^{2\nu}_{1/2}$ $(10^{20}\ yr)$	$M^{2\nu}_{GT}$ (MeV^{-1})
$^{48}Ca \rightarrow ^{48}Ti$	$0.43^{+0.24}_{-0.11} \pm 0.14$	0.05
$^{76}Ge \rightarrow ^{76}Se$	$15.5 \pm 0.1^{+1.9}_{-1.5}$	0.15
$^{76}Ge \rightarrow ^{76}Se$	11.0 ± 1.5	0.15
$^{82}Se \rightarrow ^{82}Kr$	$0.89 \pm 0.10 \pm 0.10$	0.10
$^{100}Mo \rightarrow ^{100}Ru$	$0.115^{+0.03}_{-0.02}$	
$^{100}Mo \rightarrow ^{100}Ru$	$0.095 \pm 0.004 \pm 0.009$	
$^{100}Mo \rightarrow ^{100}Ru$	$0.068^{+0.004}_{-0.005} \pm 0.007$	0.22
$^{116}Cd \rightarrow ^{116}Sn$	$0.375 \pm 0.035 \pm 0.021$	0.12
$^{116}Cd \rightarrow ^{116}Sn$	$0.26^{+0.09}_{-0.05}$	
$^{116}Cd \rightarrow ^{116}Sn$	$0.26^{+0.07}_{-0.04}$	
$^{128}Te \rightarrow ^{128}Xe$	77000 ± 4000	0.025
$^{150}Nd \rightarrow ^{150}Sm$	$0.188^{+0.066}_{-0.039} \pm 0.019$	
$^{150}Nd \rightarrow ^{150}Sm$	$0.068^{+0.004}_{-0.004} \pm 0.007$	0.07
$^{238}U \rightarrow ^{238}Pu$	20 ± 6	0.05

Table 1.3: Experimental limits for $2\nu\beta\beta$ decay

A compilation of $2\nu\beta\beta$ decay results is shown in Table 1.3. $2\nu\beta\beta$ was never measured in ^{136}Xe.

The first $0\nu\beta\beta$ decay amplitude on neutrino mass is given by Heidelberg-Moscow experiment [5]. Sum spectrum of all five ^{76}Ge detectors from 1990 to 2003, representing $71.7 kg\ yr$ of data. Expected $0\nu\beta\beta$ peak at 2039 keV is shown on Figure 1.10.

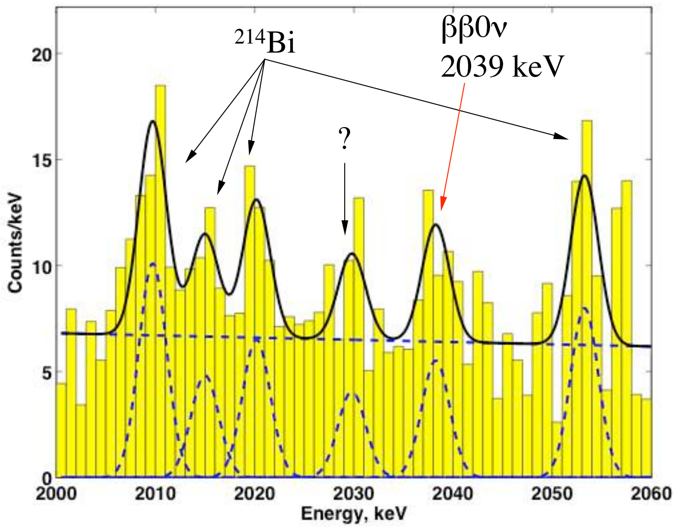

Figure 1.10: Heidelberg-Moscow first $0\nu\beta\beta$ decay peak at 2039 keV, after $71.7 kg\ yr$ (1990-2003)

A compilation of $0\nu\beta\beta$ decay results with the corresponding limits on neutrino masses is given on Table 1.4.

Transition	$T_{1/2}^{0\nu}$ (yr)	m_ν (eV)
$^{48}Ca \rightarrow ^{48} Ti$	$> 9.5\ 10^{21}$ (76% $C.L$)	< 8.3 (76% $C.L$)
$^{76}Ge \rightarrow ^{76} Se$	$1.2^{+0.3}_{-0.5}\ 10^{25}$ $(\pm 3\sigma)$	$0.24 - 0.58$ $(\pm 3\sigma)$
$^{82}Se \rightarrow ^{82} Kr$	$> 2.7\ 10^{22}$ (68% $C.L$)	< 5.0 (68% $C.L$)
$^{100}Mo \rightarrow ^{100} Ru$	$> 5.5\ 10^{22}$ (90% $C.L$)	< 2.1(90% $C.L$)
$^{116}Cd \rightarrow ^{116} Sn$	$> 7.0\ 10^{22}$ (90% $C.L$)	< 2.6 (90% $C.L$)
$^{128}Te \rightarrow ^{128} Xe$	$> 7.7\ 10^{24}$ (68% $C.L$)	< 1.1 (68% $C.L$)
$^{130}Te \rightarrow ^{130} Xe$	$> 2.1\ 10^{23}$ (90% $C.L$)	$< 0.85 - 2.1$ (90% $C.L$)
$^{136}Xe \rightarrow ^{136} Ba$	$> 4.4\ 10^{23}$ (90% $C.L$)	< 2.3 (90% $C.L$)
$^{150}Nd \rightarrow ^{150} Sm$	$> 2.1\ 10^{21}$ (90% $C.L$)	< 4.1 (90% $C.L$)

Table 1.4: Experimental limits for $0\nu\beta\beta$ decay

1.6 Discussion

Neutrino results are entangled and it is hoped that past, present and next generation experiments will provide a complete description of neutrino properties and of weak interation. Neutrino community has known very important successes during the last decade and the coming years appear to be very promising and exciting. In this particular environment, EXO will play a significant role, as described in Chapter 2.

Bibliography

[1] The absolute neutrino mass scale, Neutrino mass spectrum, Majorana CP-violation and Neutrinoless double-beta decay; S.Pascoli et. al.; hep-ph/0505226

[2] Neutrino physics; K. Zuber; Institute of Physics Publishing, 2004

[3] Neutrino masses and oscillations : Triumphs and Challenges; R.D. McKeown et. al; hep-ph/0402025, 2004

[4] Theory of neutrinos; R.N. Mohapatra et al; hep-ph/0412099

[5] Neutrinoless double beta decay and direct searches for neutrino mass; C. Aalseth et al; hep-ph/0412300

[6] Double-beta decay; S.R. Eliott et. al; hep/0202264

[7] Neutrino mass limits from SDSS, 2dFGRS and WMAP; V. Barger et al.; hep-ph/0312065

[8] Neutrino masses and the number of neutrino species from WMAP and 2dFGRS; S. Haanestad; astro-ph/0303076

Chapter 2

EXO, Enriched Xenon Observatory for double-beta decay

EXO, enriched Xenon Observatory is a double beta decay experiment based on a Time Projection Chamber detector. The final detector version, with a fiducial xenon mass of one ton will explore $0\nu\beta\beta$ decay with sensitivities down to $\sim 10\ meV$ [1]. EXO is considered as the ultimate double beta decay experiment due to its unique background suppression ability in the final version. The background is almost suppressed, thank to the possibility to identify the ^{136}Ba single ion, daughter nucleus from $\beta\beta$ decay of a ^{136}Xe nucleus. But prior to the 1 ton detector, a 200 kg Xe prototype will be comissioned. This prototype will be the biggest xenon TPC, exploring $2\nu\beta\beta$ decay in ^{136}Xe. It should provide the best $2\nu\beta\beta$ spectrum for ^{136}Xe, will allow a precise calculation of ^{136}Xe matrix elements and will be used to test EXO final detector components and technologies. It will also allow to test Heidelberg-Moscow result. Single barium tagging is currently under development for the final detector, but it will not equip the prototype version.

2.1 EXO and other double-beta decay experiments

Table 2.1 summarizes the next generation double-beta experiments; not only in ^{136}Xe, but in various $\beta\beta$-allowed isotopes. EXO will compete with some other experiments that are in a similar development phase, such as GERDA (^{76}Ge) [3], Majorana (^{76}Ge) [5], MOON (^{100}Mo) [4] and CUORE (^{130}Te). These experiments are also currently comissionning a prototype for a first data acquisition next year (2007).

2.2 EXO-200 : prototype version

2.2.1 Physics with EXO-200

A 200 kg ^{136}Xe prototype is currently under comissioning and testing phase at Stanford, before its installation at WIPP. EXO-200 will be the biggest ^{136}Xe double-beta detector ever made. It is aimed to

Experiment	$\beta\beta$ isotope	Detector	$T^{0\nu}_{1/2}$ sensit. (yr)	$\langle m_{\beta\beta}\rangle$ range (eV)
EXO	^{136}Xe	$1t$ Xe TPC	$8\ 10^{26}$	$0.05 - 0.12$
Xe	^{136}Xe	$1.56t$ Xe in liq. scint.	$5\ 10^{26}$	$0.06 - 0.15$
XMASS	^{136}Xe	$10t$ liq. Xe	$3\ 10^{26}$	$0.08 - 0.2$
CANDLES	^{48}Ca	$> 1t$ CaF_2 cryst. in liq. scint.	$1\ 10^{26}$	$0.16 - 0.3$
Majorana	^{76}Ge	$500kg$ Ge segmented diodes	$3\ 10^{27}$	$0.024 - 0.077$
GEM	^{76}Ge	$1t$ Ge in liq. N_2	$7\ 10^{27}$	$0.015 - 0.05$
GENIUS	^{76}Ge	$1t$ Ge in liq. N_2	$1\ 10^{28}$	$0.013 - 0.042$
GERDA	^{76}Ge	$1t$ Ge in liq. N_2 or Ar	$2\ 10^{26}$	$0.09 - 0.29$
NEMO-3	^{100}Mo	$10kg$ $\beta\beta$ isotopes + tracking	$4\ 10^{24}$	$0.27 - 1$
MOON	^{100}Mo	$34t$ Mo sheets in plastic scint.	$1\ 10^{27}$	$0.017 - 0.06$
CAMEO	^{116}Cd	$1t$ $CdWO_4$ cryst. in liq. scint.	$> 10^{26}$	$> 0.07 - 0.22$
CUORE	^{130}Te	$750kg$ TeO_2 bolom.	$2\ 10^{26}$	$0.05 - 0.17$
COBRA	^{130}Te	$10kg$ $CdTe$ semicond.	$1\ 10^{24}$	$0.7 - 2.4$
DCBA	^{150}Nd	$20kg$ Nd layers + tracking	$2\ 10^{25}$	$0.035 - 0.05$
GSO	^{160}Gd	$2t$ Gd_2SiO_5 cryst. in liq. scint.	$2\ 10^{26}$	0.065

Table 2.1: Compilation of next generation $0\nu\beta\beta$ experiments. $T^{0\nu}_{1/2}$ sensitivities and $\langle m_{\beta\beta}\rangle$ are normalized to 5 years data taking [6].

- measure $2\nu\beta\beta$ decay with the best sensitivity for ^{136}Xe and therefore contribute significantly to the 2ν nuclear matrix elements constraining.
- EXO-200 is also dedicated to test the technologies involved in the final detector design. In particular the accuracy of a ton-scale TPC with liquid Xenon and primary scintillation in LXe thank to avalanche photodiodes.
- understand backgrounds from radioactivity at this scale.
- test Heidelberg-Moscow

Table 2.2.1 shows the Majorana mass sensitivity for EXO-200. The calculated 40 backgrounds events correspond to 20 events/year radioactive background in $\pm 2\sigma$ interval centered around the 2481 eV endpoint ($Q_{\beta\beta}$ of ^{136}Xe). This calculation is based on a simulation of radioactive decays around $Q_{\beta\beta}$ with the measured radioactivities of the detector components.

Mass	Eff	Time	$\sigma(E)/E$	Bkgnd	$T^{0\nu}_{1/2}$	Majorana mass	
(ton)	(%)	(yr)	(%)		(yr)	QRPA	NSM
0.2	70	2	1.4	40	$6.4\ 10^{25}$	0.27 eV	0.38 eV

Table 2.2: EXO-200 sensitivity to Majorana mass

Moreover, EXO-200 is sensitive enough to confirm — or infirm — the presumed $0\nu\beta\beta$ result from Heidelberg-Moscow collaboration[1]

---

[1] Phys. Lett. B586 (2004), 198-212.

$$T^{0\nu}_{1/2}(Ge) = 1.2^{+0.3}_{-0.5}\ 10^{25}\ year\ (\pm 3\sigma)$$

corresponding to $0.24eV - 0.58eV$. With two years EXO-200 data acquisition, one will have

- In the worst case — i.e QRPA model, upper limit — 15 $\beta\beta$ events (around $Q_{\beta\beta}$) on top of 40 background events. This corresponds to 2σ.
- In the best case — i.e. NSM, lower limit — 162 $\beta\beta$ events on top of 40 background events. This corresponds to 8.5σ.

2.2.2 EXO-200 detector

EXO-200 prototype is a TPC with 200 kg liquid ^{136}Xe, enriched to $\sim 80\%$. The LXe chamber is made of $5mm$ thick ultralow radioactivity copper (NOSV). Figure 2.1 shows this LXe copper chamber.

Figure 2.1: 200 kg ^{136}Xe chamber design, made with 5 mm thick NOSV copper.

The LXe chamber has reinforced copper end caps and is mounted on the cryostat inner vessel door with four legs, also useful as feedthrough for LXe, high voltage and signal readout. Figure 2.2 shows LXe chamber mounted on the cryostat door.

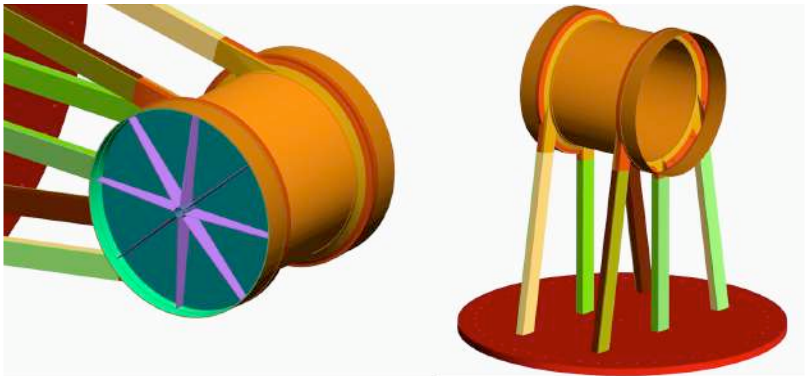

Figure 2.2: LXe chamber mounted on cryostat door with copper end caps.

Xenon is liquid for temperatures around -110^oC, depending on the pressure (-108^o to -110^o at 1 bar). The LXe chamber is thus in a cryostat made of two NOSV copper vessels. A refrigerant liquid circulates around the LXe chamber in the inner vessel and 3 heat exchangers are distributed on the top of it to keep the right temperature. Figure 2.3 shows LXe chamber, inner and outer vessels of the cryostat.

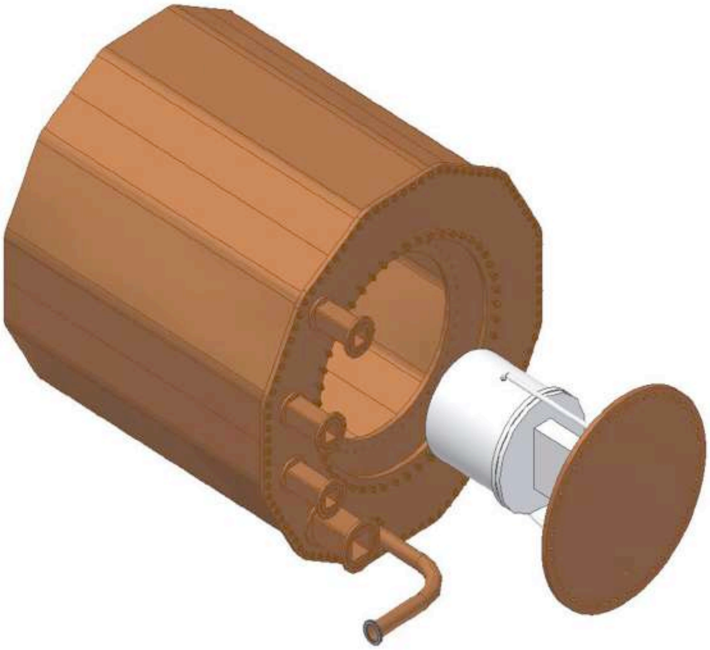

Figure 2.3: Outer vessel, inner vessel and 200 kg ^{136}Xe chamber.

The TPC inside LXe chamber has a NOSV copper frame with field rings for linear electrical field ($\overrightarrow{E}_{drift}$). Between the field rings are teflon reflectors to reflect the scintillation light. Fig 2.4 shows the TPC copper frame for the wires and APD's and the field rings. Teflon reflectors are also shown. EXO-200 TPC is made of two 1/2 TPC volumes.

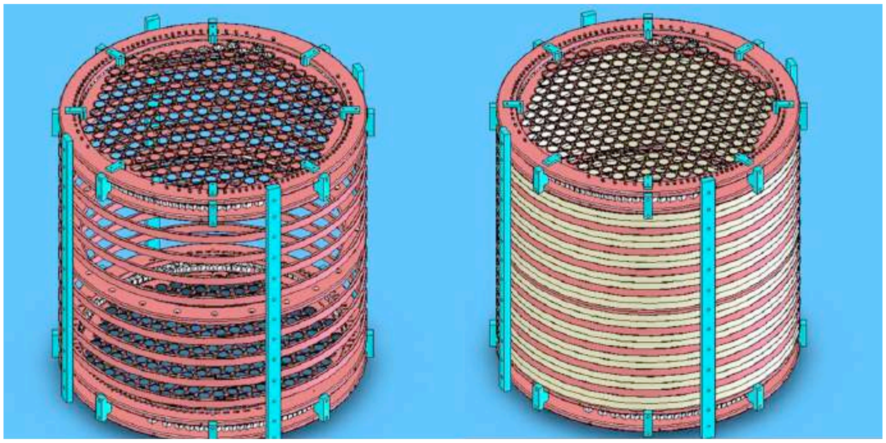

Figure 2.4: TPC frame.

A grid of 100 μm wires collect the charge deposited by ionization of both $\beta\beta$ electrons in LXe; wires are ganged in groups of 3; 48 in the x-axis and 48 in the y-axis. Charge readout with the wires give the x and y positions of the event.
The primary scintillation light is measured with avalanche photodiodes (APD) located behind the wire grid. The time between scintillation signal and electrons signal gives the drifting distance, i.e. the z position of the event. APD's disposal is shown on Figure 2.5.
The collabaration showed that the energy resolution is improved when measuring ionization and scintillation [7] :

$$\frac{\sigma(E)}{E} = 1.8\% \; at \; Q_{\beta\beta} \;\; : \;\; ionization \; alone$$

$$\frac{\sigma(E)}{E} = 1.4\% \; at \; Q_{\beta\beta} \;\; : \;\; ionization + scintillation$$

These values are calculated for an energy E corresponding to the $Q_{\beta\beta}$ value of ^{136}Xe , i.e. 2481 keV.

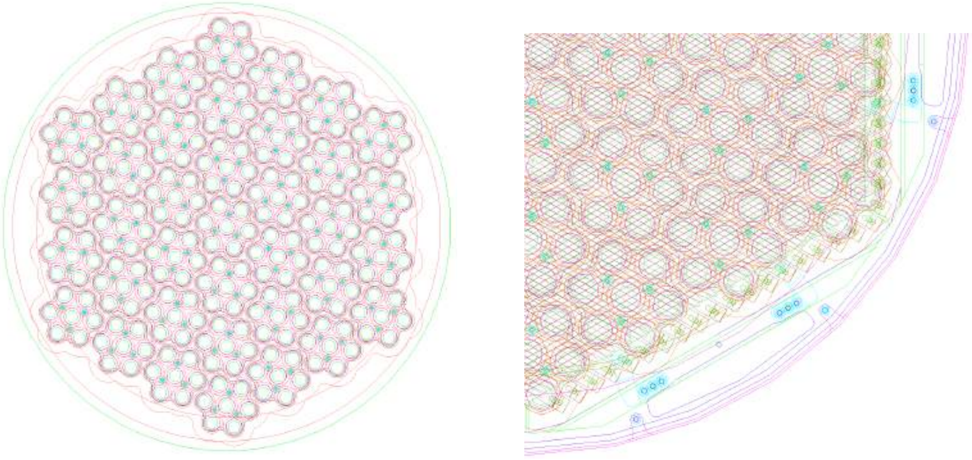

Figure 2.5: APD's disposal in EXO-200 detector

2.2.3 Radioactivity background

Radioactivity from materials used for the detector are source of intrinsic background. A considerable effort was applied for materials selection. Radioactivity measurements were performed with different methods :

- Mass spectrometry (Canada Standards)
- Gamma spectroscopy (Neuchâtel)
- Radon emanation (Laurentian)
- Neutron activation (Alabama)

A list of ~ 100 samples were measured and Monte-Carlo simulations with EXO detector geometry performed to calculate the induced background events around the $Q_{\beta\beta}$ value of ^{136}Xe [2]. As an example, EXO-200 cryostat is made of ultralow radioactivity NOSV copper. Electron gun welding in vaccuum was used to avoid adding impurities and thus extra radioactivity. Figure 2.6 shows the cryostat inner and outer vessels.

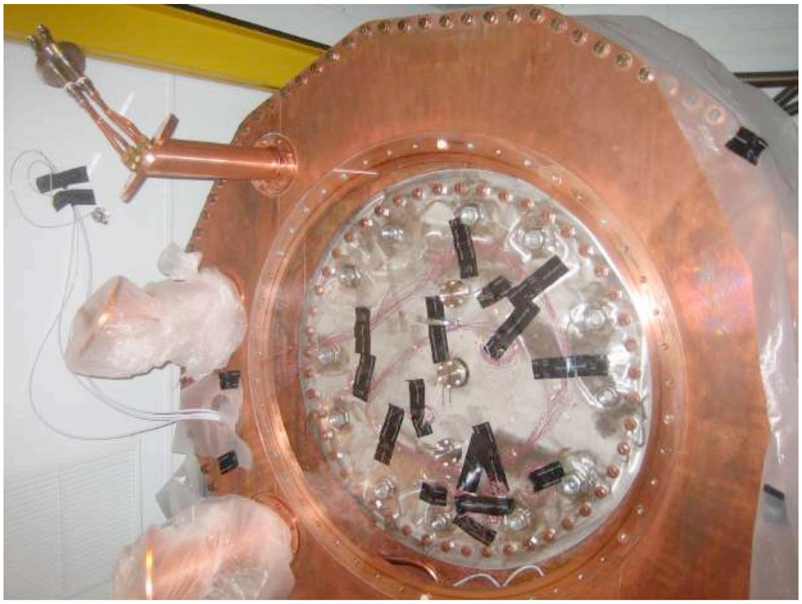

Figure 2.6: Copper cryostat installation in the cleanroom.

2.2.4 ^{136}Xe enrichment

^{136}Xe is extracted by air centrifugation and isotope separation. Xenon enrichment has been done in Krasnoiarsk, Russia. 200 kg of ^{136}Xe has been produced in Spring 2003. Table 2.3 shows natural and enriched xenon isotopes abundances, i.e. xenon isotopes before and after enrichment, respectively. Moreover, krypton isotope is negligibly small in enriched xenon

$$^{85}Kr/Xe < 3.4\ 10^{-7}\ (90\%\ C.L.)$$

2.2.5 EXO-200 experimental site

EXO-200 stands in a cleanroom environment and the detector is shielded against local radioactivity with ultrapure lead, as shown on Figure 2.7

The EXO-200 detector will be installed at WIPP (Waste Isolation Power Plant, New Mexico), which is 655 m deep, corresponding to a 2000 m water equivalent shielding. The rock is almost composed of halite ($NaCl$). This makes the site very clean in term of natural radioactivity, as shown on Table 2.4. The low ^{238}U concentration leads to ^{222}Rn concentration in the air lower than 7 Bq/m^3 with normal ventilation [1].

Xenon isotope	Natural ab. (%)	Enriched ab. (%)
124	0.096	$3.1\ 10^{-3}$
126	0.090	$7.5\ 10^{-3}$
128	1.920	$4.5\ 10^{-3}$
129	26.44	$7.6\ 10^{-3}$
130	4.080	$8.8\ 10^{-3}$
131	21.18	$2.7\ 10^{-2}$
132	26.89	0.33
134	10.44	19.3
136	8.870	80.3

Table 2.3: Xenon isotopes abundances before and after enrichment.

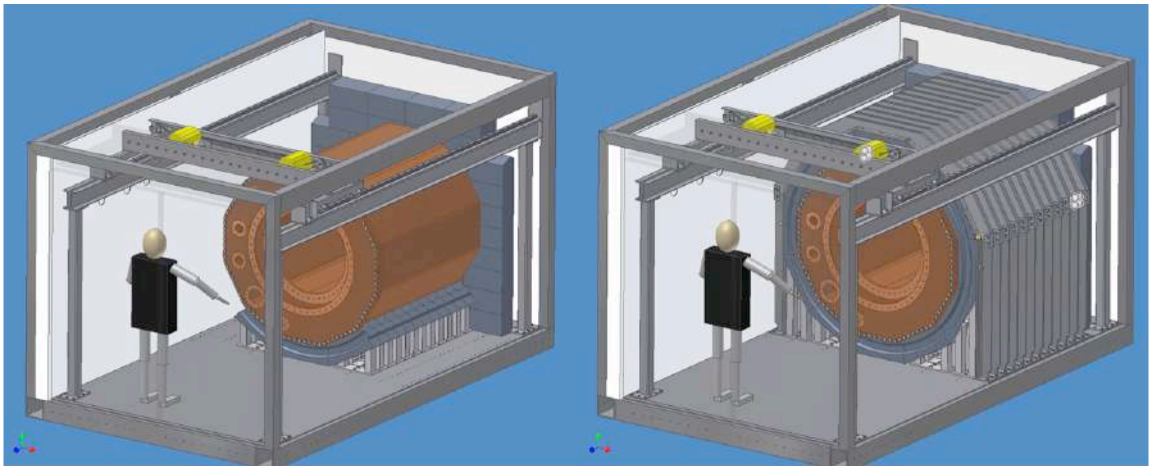

Figure 2.7: Detector installation at WIPP.

Isotope	WIPP	Gran Sasso	Kamioka	SNO
^{238}U (ppb)	$30-50$	$500-1000$	$600-1600$	1200
^{232}Th (ppb)	$70-80$	$100-1500$	$1800-2600$	5300
^{40}K (ppm)	$0.1-0.8$	$0.06-0.3$	$1.5-2.1$	not known

Table 2.4: Natural radioactivity concentrations at different underground experimental sites.

2.3 EXO-Full, final version

EXO-Full will be a one ton ^{136}Xe TPC, running with the unique ability of practically background free double-beta events identification. A liquid (LXe) or gaseous (GXe) version largely depends on EXO-200 conclusions. Table 2.5 summarizes advantages and disadvantages of both versions.

The physics aimed in the final version of EXO is shown in Table 2.3

1 ton ^{136}Xe	Gaseous 5 bar TPC (GXe)	Liquid TPC (LXe)
Fiducial volume	$\sim 5m^3$	$< 0.5m^3$
Spatial resolution	position + e^- tracks (β range $> 20cm$)	position but no e^- tracks
Event identification	in situ Ba tagging	Ba ion extraction

Table 2.5: Gaseous TPC (GXe) versus liquid TPC (LXe) versions.

EXO case	Mass (ton)	Eff (%)	Time (yr)	$\sigma(E)/E$ (%)	$T_{1/2}^{0\nu}$ (yr)	Majorana mass QRPA	Majorana mass NSM
conservative	1	70	5	1.4	$2\ 10^{27}$	50 meV	68 meV
agressive	10	70	10	1.0	$4.1\ 10^{28}$	11 meV	15 meV

Table 2.6: EXO-full Majorana mass sensitivity.

2.3.1 Barium grabbing and tagging

In a liquid TPC version, barium single ion must be extracted from liquid xenon and transferred to the linear trap for laser spectroscopy. In a gaseous TPC version, laser spectroscopy could be done in situ (R&D in progress) or after ion extraction.

^{136}Ba ion grabbing

Ion grabbing was demonstrated in liquid Xenon with ^{230}U decay daughter. Figure 2.8 shows the schematic of the probe cell operating in LXe and the decay chain of ^{230}U.

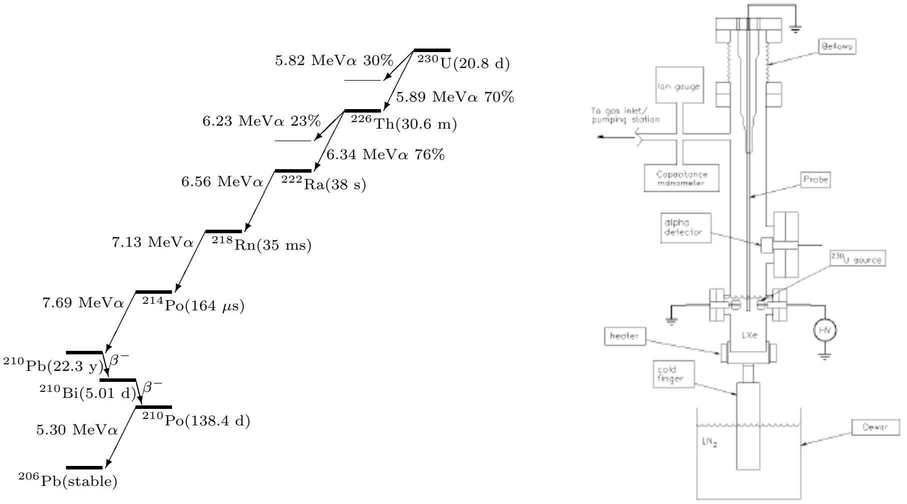

Figure 2.8: ^{230}U decay chain (left) and probe cell schematic (right).

^{230}U daughter ions are emitted in LXe and an electric field between the source and the tip attracts ions on the tip. The tip is then moved upwards, out of liquid xenon and placed in front of an alpha-counter. Figure 2.9 shows various peaks from ^{230}U decay measured in vacuum and from the tip after ^{230}U ions collection.

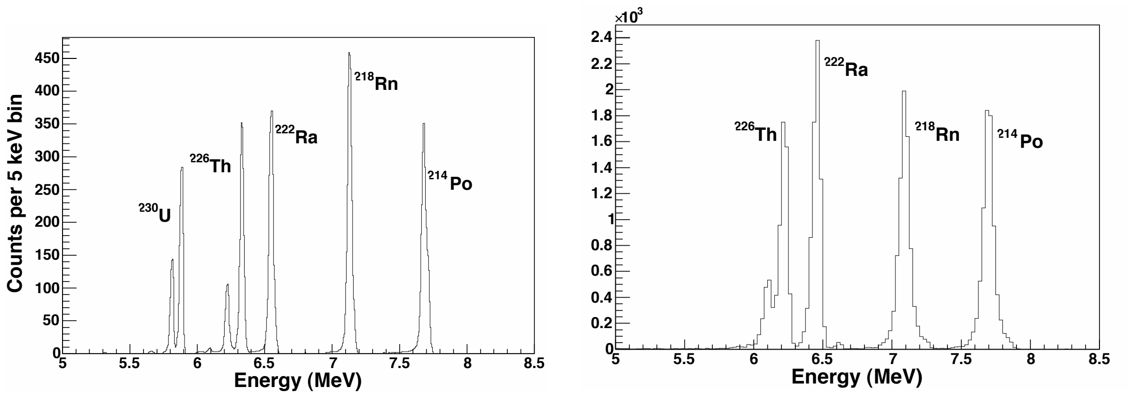

Figure 2.9: ^{230}U source, measured in vacuum (left) and ^{230}U ions collected on the tip (right).

Several different probes are under investigation at the moment

- *Field-emission probe*; an electical potential in this very sharp tip produces a huge electrical field at the sharp end of it, expelling the ion.
- *Cryoprobe*; the cryoprobe is made of two concentric tubes. A gas at high pressure circulates in the inner tube, expands at the probe end, cooling the probe by Joules-Thomson effect (this can be replaced by a LN_2 circulation). Xenon ice forms at the probe end and an electric field is applied to attract the ion in the ice. For releasing the ion, a light electric field is applied and the spectroscopy chamber is pumped out, so that xenon sublimate and the barium ion is released.

Field-emission probe and cryoprobe are shown on Figure 2.10

A grabber cell is currently being built. This cell will be able to collect a single barium ion on a tip in LXe, bring it to the linear trap and release it. The ^{136}Ba source is not defined yet, an other possibility could be to use the actual barium oven. In this case, the tip attracts and collects an ion in the linear trap; the tip moves then to the LXe dewar and releases the ion. The tip moves back to linear trap and laser spectroscopy checks ion has been released. The tip moves to the LXe dewar and collects the single ion again and moves backwards to the linear trap. Laser spectroscopy positively identifies barium ion. This process should show a clear proof of barium ion grabbing /release in liquid xenon and measure the efficiency, which is a crucial parameter.

^{136}Ba ion tagging

After grabbing, double-beta event identification is done by laser spectroscopy. The single ^{136}Ba ion is released in a linear trap and spacially stabilized. A 493 nm blue laser and 650 nm red laser excite the barium ion. An important amount of visible

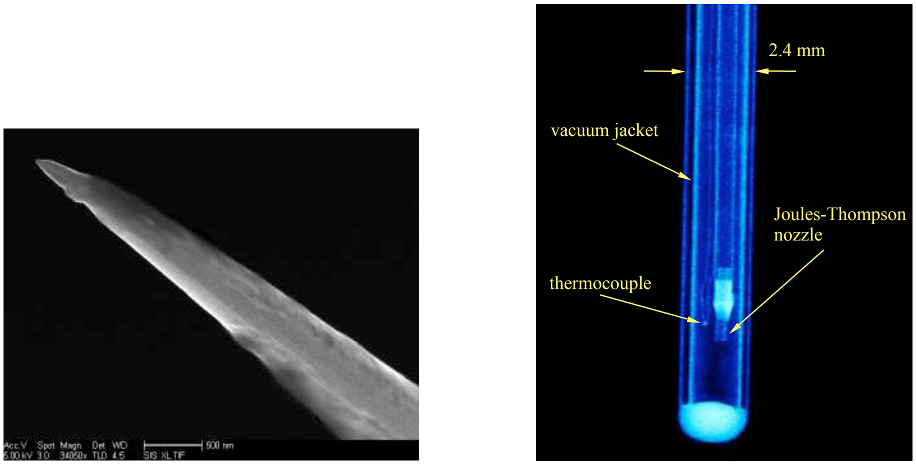

Figure 2.10: Field-emission probe SEM image (left) and Cryoprobe x-ray image (right).

photons ($\sim 10^7\ photons/sec.$) are emitted after barium desexcitation. These photons are measured with a CCD camera. Figure 2.11 shows the barium spectroscopy scheme.

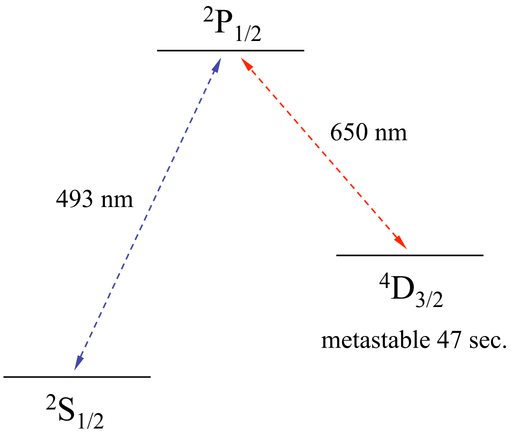

Figure 2.11: ^{136}Ba laser spectroscopy.

R&D of single ^{136}Ba ion tagging is currently under investigation. A linear trap equipped with a laser spectroscopy system was installed at Stanford. A barium-carbonate wire is used, on which - when heated up - an exothermic chemical reaction starts that releases barium vapor and CO2. The barium vapor goes with ballistic trajectories onto a tantalum foil, which can be heated and releases Ba vapor in a more controlled way. An electron gun ionizes part of the vapor. Barium ions follow ballistic trajectories, and part of those go into the upper section of the quadrupole trap.

The RF-field in the trap can only confine specific trajectories and specific phases, so that these particles are either good to be trapped, or hit a buffer gas atom to be turned in the right direction to be trapped.

Then they follow the DC bias on the trap segments to the lower section, where spectroscopy happens (Figure 2.12). However, the buffer gas needs to have a small mass, so that a collision does not change the angle of the motion too much (which is why xenon as buffer gas does not work, yet).

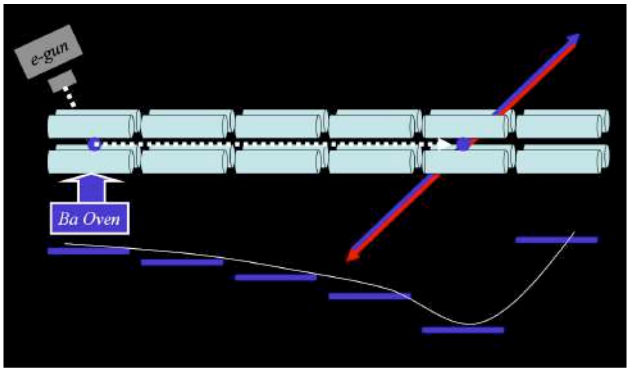

Figure 2.12: Single barium ion trapping and laser spectroscopy principle.

Lasers can be fine tuned so that frequency corresponds exactly to the frequency for barium spectroscopy. Blue and red lasers are shown on Figure 2.13, as well as the linear trap

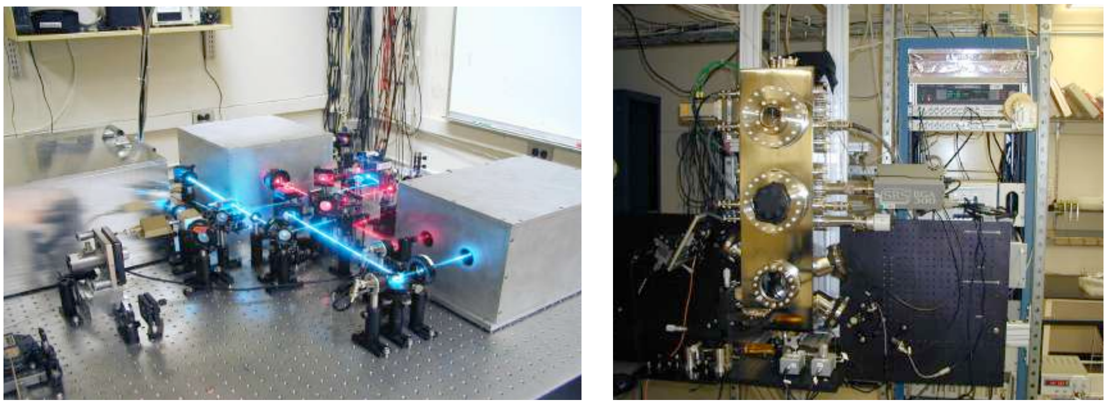

Figure 2.13: Blue and red lasers for laser spectroscopy (left). Linear trap installed in the lab (right).

The Ba-oven produces huge clouds of ions. The barium loading system is now done by turning on a cold cathode gauge, which ionizes a few bariums atoms. The trap is thus filled with a few ions only, typically 5-6. The loss mechanisms from the trap is basically caused by collisions with heavy gas, which changes the trajectory of the ion to higher radius orbits (which are less stable). The other mechanism is repulsive Coulomb interaction of the ion cloud. These processes help to reduce the number of ions. When there is only one ion left, we start measuring the lifetime. However, the same loss mechanism is now a problem, as we can loose our ion due to gas collisions. Figure 2.14 shows the barium ions quantization.

Single barium ion trapped and stabilized were exposed to laser spectroscopy. The

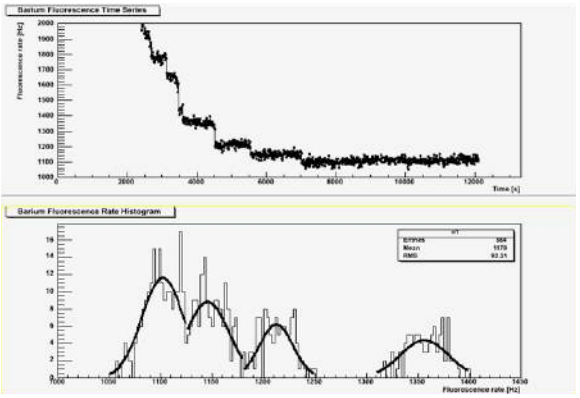

Figure 2.14: Barium ions quantization.

resulting photon emission was measured with a CCD camera. An image is shown on Figure 2.15 .

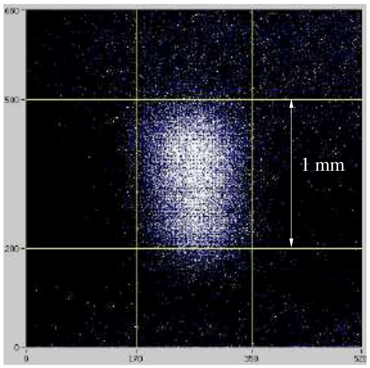

Figure 2.15: Laser spectroscopy of trapped single barium ion.

2.4 Discussion

The EXO collaboration has a 200 kg ^{136}Xe detector almost ready for data taking. This prototype detector will not only be a "proof-of-principle detector" to test the technologies involved in the full version, but above it will also have a good sensitivity to $2\nu\beta\beta$, aiming at fine tuned nuclear matrix elements of xenon. It will also allow to confirm or disprove the Heidelberg-Moscow result.

In the same time, developments for the final detector version look promising, with technologies able to collect a single ion — daughter nucleus from $\beta\beta$-decay of ^{136}Xe — raising to a background-free experiment, unique specificity in the world of future $\beta\beta$-decay experiments.

Bibliography

[1] EXO proposal, EXO collaboration, April 2000.

[2] EXO website and internal notes for collaborators (elog) : http://grattalab3.stanford.edu/exo_elog.

[3] Progress report to the LNGS scientific comitee; The GERDA collaboration; LNGS-EXP 33/05 add. 3/06

[4] Multilayer scintillation detector for the MOON double-beta decay experiment : Scintillation photon responses studied by a prototype detector MOON-1; The MOON collaboration; hep-ph/0609008

[5] The Majorana ^{76}Ge double-beta decay project; The Majorana collaboration; hep-ex/0201021

[6] Neutrino masses and oscillations : Triumphs and challenges; R.D. McKeown, P. Vogel; hep-ph/0402025

[7] Correlated fluctuations between luminescence and ionization in liquid xenon; E.Conti et. al; the EXO collaboration; Phys. Rev. B 68 (2003)

Chapter 3

Barium source for ^{136}Ba ion grabbing : a first attempt

Barium tagging and identification will be an important point in the EXO full detector. And for R&D of the barium tagging experimental setup, one need to have barium ions as in the detector. Radioactive ^{137}Ba ions can be used as markers because one can measure their radioactive decay and thus identify them. The goal of this project was thus to make a radioactive source of ^{137}Ba. This chapter shows a way to make such a barium source from a $^{137}CsCl$ commercial source, in a HCl solution.

3.1 ^{137}Cs decay

^{137}Cs decay is shown in Fig. 3.1. Cesium decay has $T_{1/2} = 30$ *years* while barium has $T_{1/2} = 153$ *sec.*, so that the photon emission rate measured within a few minutes or even hours is almost constant.

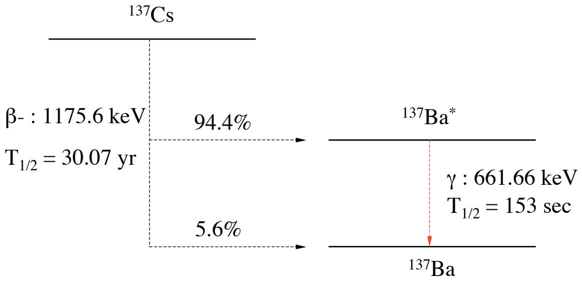

Figure 3.1: ^{137}Cs decay; Number of counts as a function of the analyser channel.

We used a NaI crystal detector coupled to a PMT[1]. Emitted photons were measured. Cesium decay spectrum is shown in Fig. 3.2.

---

[1] Saint-Gobain Crystals and Detectors, Crismatec, type 51 S 51

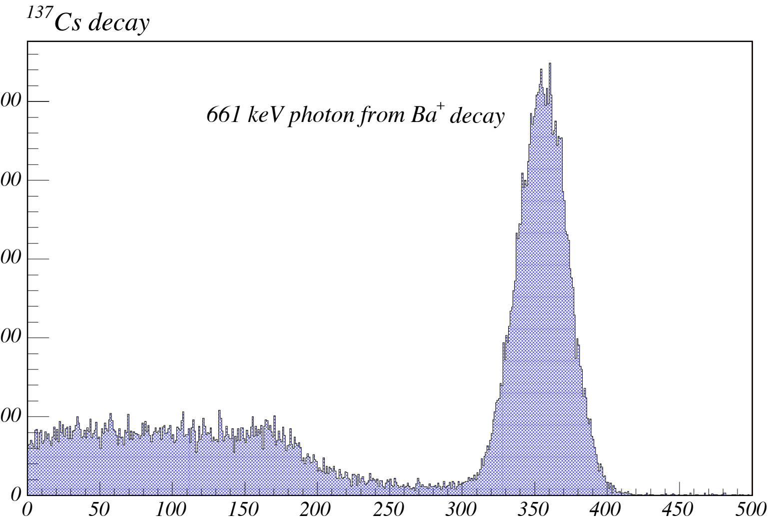

Figure 3.2: ^{137}Cs decay.

3.2 $^{137}CsCl$ in solid phase

In a first step, $CsCl$ in HCl solution droplets were deposited on a 1 cm^2 tungsten boat. After a few hours at room temperature, HCl evaporates and $CsCl$ crystal remains on tungsten. Activity of this source was measured and was 0.3 μCi.

3.3 $Cs - Cl$ photodissociation

The next step consisted in breaking the $CsCl$ bond to have ^{137}Cs ions (and thus ^{137}Ba ions, according to Fig 3.1). Electrons from 5 eV to 1000 eV, coming from an e-gun were used for this purpose in a first try, without success. An other possibility is the photodissociation of the molecule with photons. Fig 3.3 shows the absorption spectrum for the particular case of cesium chloride and thus the wavelength that can break $CsCl$ into Cs^+ and Cl^-. UV photons below 300 nm have to be used for this purpose. I tried first with a mercury short-arc lamp emitting a broad spectrum from 275 nm to the visible. But the deepest UV photons coming out from this lamp were only 275 nm and $CsCl$ absorption at this wavelength is not very efficient. Moreover the photon flux was quite low.

I used then an excimer KrF 248 nm UV laser[2]. This laser produces 248 nm photons in shots with a frequency from 1 Hz to 20 Hz, and with an energy of 1080 mJ. UV photons were shot on the $CsCl$ crystal and an electrical field was maintained between the tungsten boat containing the source and a tantalum plate, used to collect the cesium and barium positive ions, as shown in Fig. 3.4. It was possible to evaporate $CsCl$ in a buffer gas to realize the photodissociation. I tried it but $CsCl$ molecules went everywhere in the chamber and some only sticked to the

---

[2] Coherent Lambda Physik GmbH, Göttingen, Germany, KrF excimer laser, 248nm, model LX 300

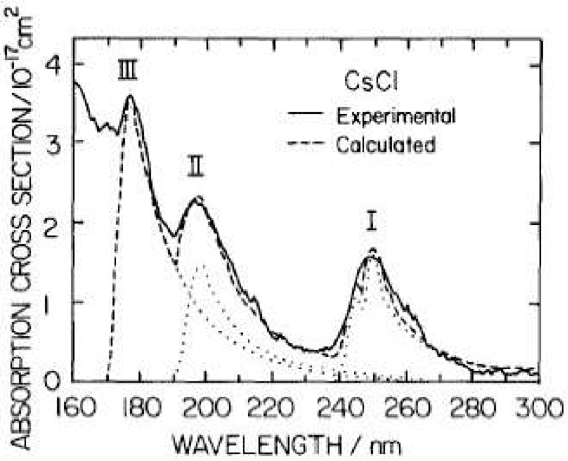

Figure 3.3: $Cs - Cl$ absorption spectrum [1].

collection plate. Photodissociation of cristalline $CsCl$ works and was much more easy to handle. With 120 laser shots, a 5.4 nCi ions source was obtained. Fig. 3.5 shows the numbers of photodissiociated Cs (and Ba) ions in terms of photons counted per 300 sec in the NaI detector (number of counts in the 661 keV peak).

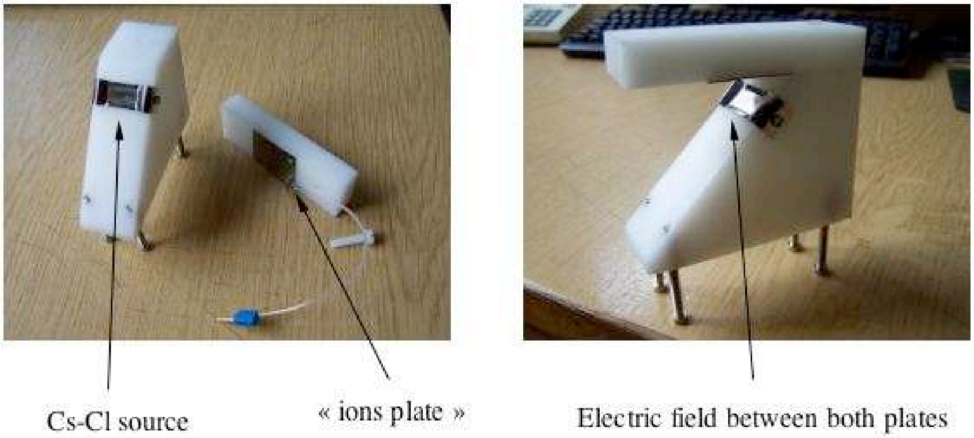

Figure 3.4: Setup for UV laser photodissociation in vacuum.

3.4 ions "confirmation"

To be sure that Cs and Ba ions were on the tantalum plate, instead of $CsCl$ (or $BaCl$), I used the setup shown in Fig. 3.7. The tantalum plate with ions was heated to 960 ^oC in argon atmosphere at 700 $mbar$. Tantalum plate was heated with a current passing through it; its temperature, as a function of the current is shown in Fig. 3.6.

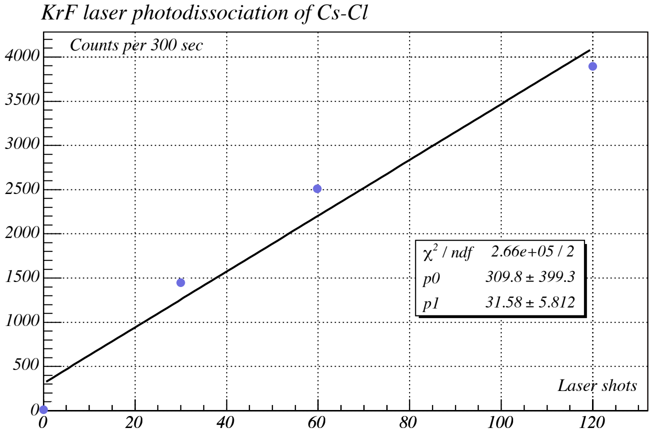

Figure 3.5: ion plate activity with various laser shots numbers.

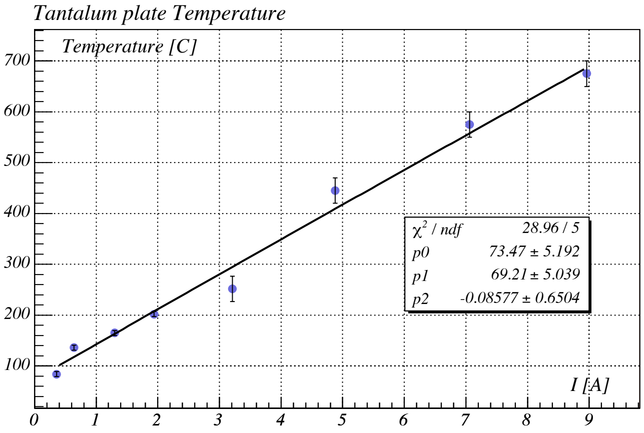

Figure 3.6: Tantalum plate temperature.

Ions were evaporated from the so-called ions plate. A positive potential was maintained on the deviation plate to deviate the ions and negative potential of the collection plate to collect them. With such a geometry of the different plates, it was not possible for particles to evaporate directly from ions plate to collection plate. Moreover, uncharged $CsCl$ would go straight to deviation plate. Ions in Ar atmosphere are much slower than in vacuum, so that it was possible to deviate them from their initial trajectories.

Ions plate, deviation plate and collection plate were gamma counted under NaI detector. The number of counts per 300 seconds in the 662 keV peak was measured. Deviation plate showed only a flat background (no 661 keV peak), so one can say that no $CsCl$ was evaporated. Source plate showed a smaller activity after 300 sec heating and an even smaller activity after 10 minutes heating. Collection plate was measured and the missing ions on the source plate observed on the collection plate, as shown in Fig 3.8. Ba and Cs ions went thus from the source plate to the collection plate.

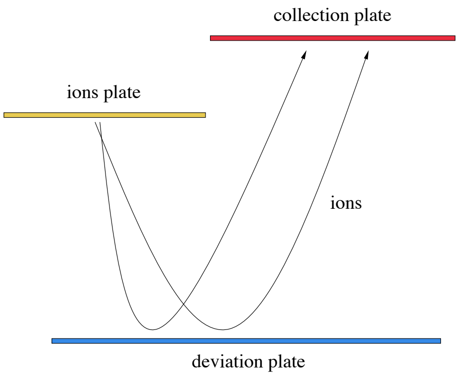

Figure 3.7: setup to identify ions.

Important notice : Cs^+ and Ba^+ ions are extremely unstable in the metallic form. They combine with O_2, CO_2, humidity, N_2, etc... . Experimentally, even if the process is done under very high vacuum, with rare gases and with ultraclean inert plates, barium quantity is very small and combines with remaining atoms or molecules in the chamber or with a remaining monolayer on the plates, so that Cs and Ba ions are always ionic compounds of Cs and Ba. It was the case in this simple setup.

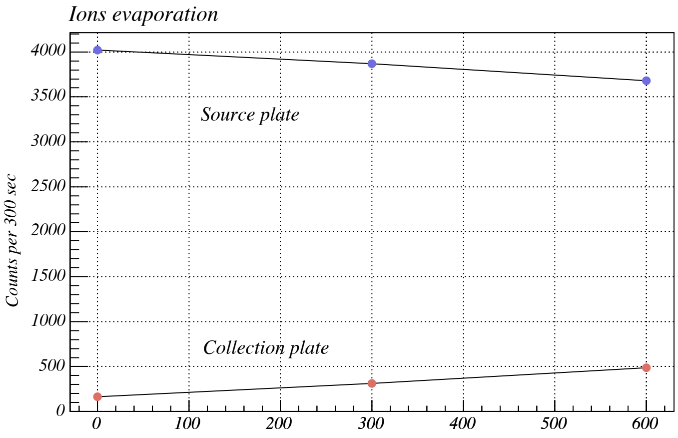

Figure 3.8: ions evaporation and collection, as a function of time [sec].

3.5 ^{137}Ba decay

Not only barium ions, but also cesium ions (ionic compounds) are on the collection plate. With a selective thermal desorption, one can evaporate cesium ions but not barium ions. In 0.1 $mbar$ vacuum, metallic cesium evaporates at 200 ^oC and metallic barium at 720 ^oC. Those temperatures are similar for $CsCl$ and $BaCl$ and for other Cs and Ba compounds. Ion plate was thus heated to approximately 500 ^oC for 30 minutes. An important fraction of cesium ions evaporated, so that cesium-barium equilibrium was broken. It was not easy to find the right heating time of the ion plate to evaporate most of the ^{137}Cs ions.

Finally, barium decay can be observed by measuring the number of counts in the 661 keV peak every 10 seconds. $T_{1/2}$ can be calculated according to the exponential fit parameters, as shown in Fig. 3.9. One find : $T_{1/2} = 147.6 \pm 3.1$ sec (barium decay has $T_{1/2} = 153$ sec). Then barium comes to a new equilibrium with cesium, after a few minutes.

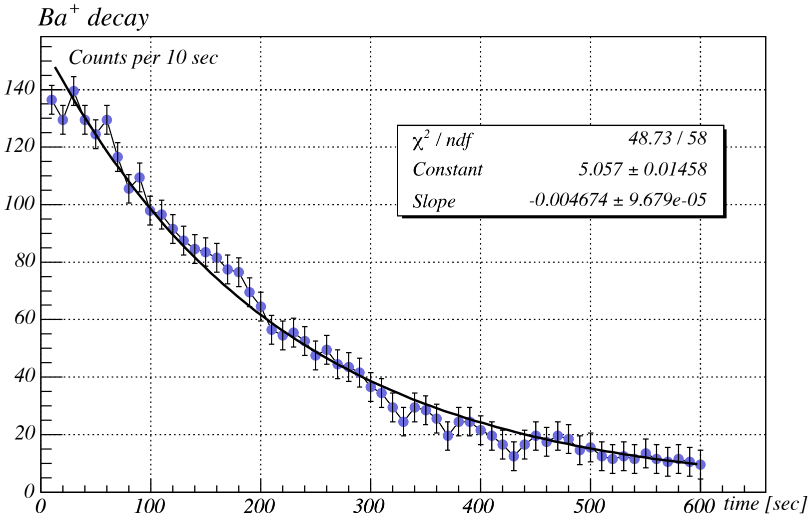

Figure 3.9: $^{137}Ba^+$ decay.

If one measures the gamma activity of the chamber after this selective evaporation, an increase of 662 keV photons can be observed, with the same $T_{1/2} = 153$ sec (see Ralph's talk, EXO week 2005).

Observation : if one rinse the ion plate under hot water (60 ^oC) for 30 sec to 1 min, ions are totally released from the plate.

3.6 Discussion

It has been shown that it was possible to have ^{137}Ba ions (or at least Ba ionic compounds) on a tantalum substrate. From a 0.3 μCi (11.1 kBq) $^{137}CsCl$ crystal, one obtained finally (with 120 laser shots of 1.08 J) a 5.4 nCi (200 Bq) ^{137}Ba radioactive source. For full-EXO R&D, it should be possible to replace the tantalum plate with a tip. In this case, ^{137}Ba ions could be used in the liquid Xenon trap to study the ions release from the tip.

In our basic setup, Cs and Ba ions are certainly Cs and Ba ionic compounds, as I took no special precautions to keep Cs^+ and Ba^+ stable. All processes have to be done in ultrahigh vacuum, with rare gases and using ultraclean materials (plates, tip, etc...) if stable Ba^+ is needed.

Several other possibilities to build a barium source are under investigation within the EXO collaboration :

- build a ^{137}Ba plasma and extract a barium ions flux [7].
- Chemical reactions in a solution of $^{137}CsCl$ and Na, leading to $NaCl$ and $^{137}Cs(^{137}Ba)$.

Bibliography

[1] Absorption spectra of alkali halide molecules in the vacuum ultraviolet; S.Kubodera et. al.; J. Chem. Phys. 92 (1990); 5867-5874.

[2] Control of the photodissociation of CsCl; A.Glass et al., Appl. Phys. B 71 (2000); 267-276.

[3] Theoretical dissociation energies for the alkali and alkaline-earth monofluorides and monochlorides; S.R.Langhoff et. al.; J. Chem. Phys. 84 (1986); 1687-1695.

[4] Measurements of the electric dipole polarizabilities of the alkali halide dimers; R.Kremens et. al.; J. Chem. Phys. 81 (1984); 1676-1681.

[5] Alkali halide photofragment spectra. III Alkali chloride bond energies and excited states symmetries at 266 nm; T.Min et. al.; J. Chem. Phys. 72 (1980); 6632-6636.

[6] Collisional dissocoation and chemical relaxation of alkali halide molecules : 2000-4000K; R.Milstein et. al.; J. Chem. Phys. 80 (1984); 6025-6037.

[7] Ion beam generation froma thermal contact ionization plasma source; I.Katsumata et. al; Rev. Sci Instrum. 65 (1994); 1392-1394.

Chapter 4

Micropatterned LEM and scintillation in TPC

This chapter will discuss R&D in view of a gaseous version of EXO-full.
Particles crossing a Time Projection Chambers (TPC) ionize the fiducial volume of gas or liquid, generating electrons and the corresponding ions along the particle's track. Photons are also emitted during this process, called primary scintillation. An electric field ($100 - 200\ V \cdot cm^{-1} \cdot bar$) drift these electrons towards an amplification grid. The important electric field in this region ($10 - 50\ kV \cdot cm^{-1} \cdot bar$) accelerates the electrons such that they form electromagnetic showers. Each single electron from the initial particle's ionization generates n secondary electrons, during what is called the avalanche. n is the gain of the grid, and typically in the range $100 < n < 10^4$. Photons are also generated in the avalanche, and this is known as secondary scintillation. Figure 4.1 shows the different processes involved. Various amplification systems exist :

- Wires chambers, developed at CERN [1]
- Micromegas, developed at CERN and Saclay [2]
- GEM (Gaseous Electron Multiplication), developed at CERN [3]

And a lot of variations between these (such as SGG [5]), including

- LEM (Large Electron Multiplication), developed in Neuchâtel [4]

The LEM has several advantages compared to GEM; its robustness makes it easy to handle and to operate. It is very reliable and not affected by discharges.

4.1 SILEM : Strips integrated LEM

The original LEM was a vetronite substrate 1 mm thick with copper layers on both sides, in which 500 μm holes were mechanically drilled. Figure 4.1 shows the principle. It was very robust but not really optimized. A Maxwell/Garfield simulation of the LEM shows that some drift lines are driving electrons on the

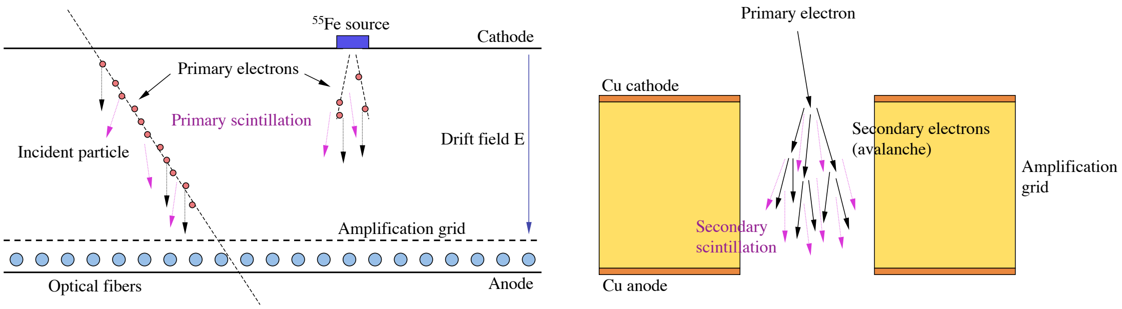

Figure 4.1: TPC principle, with charge and scintillation readout systems.

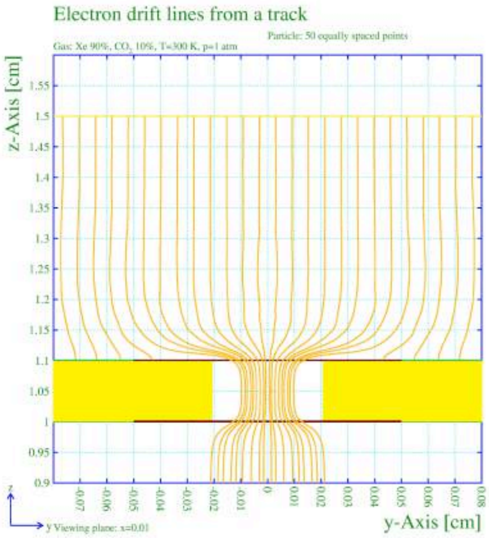

Figure 4.2: LEM drift lines simulation.

copper anode instead of driving them through the LEM holes. This means that some electrons from the initial particle's track are lost. Figure 4.2 shows this problem.

Simulation of various grid geometries — i.e. holes size, holes pitch, thickness — has been done to solve this problem and to optimize the gain. This has been done on the new SILEM. Moreover, the SILEM integrates an $x - y$ detection plane directly on the amplification grid (SILEM : LEM with integrated strips). This system is thus able not only to amplify the electronic signal but also to tell us through which hole the electron are going. Various designs were built

- x-strips on one side of the LEM and y-strips on the other side.
- x and y strips on the same LEM side, separated by a 20 μm kapton substrate. This design allows a readout of both x and y at ground (Figure 4.3)
- x and y pixels on the same LEM side. This allows a readout of both x and y at ground and moreover there is no crossover between both. This pixel design is shown on Figures 4.3 and 4.4. Each pixel has 4 holes, corresponding

to 1 mm^2. Figure 4.3 shows pictures of the first fabrication batch, made by Cicorel SA. The second batch, made at CERN has some variations : a 400 μm thickness vetronite substrate, instead of 300 μm kapton substrate. The increased thickness allow to have a larger gain. The upper layer is etched on the CERN grid, so that pixels under the first 20 μm substrate are "opened".

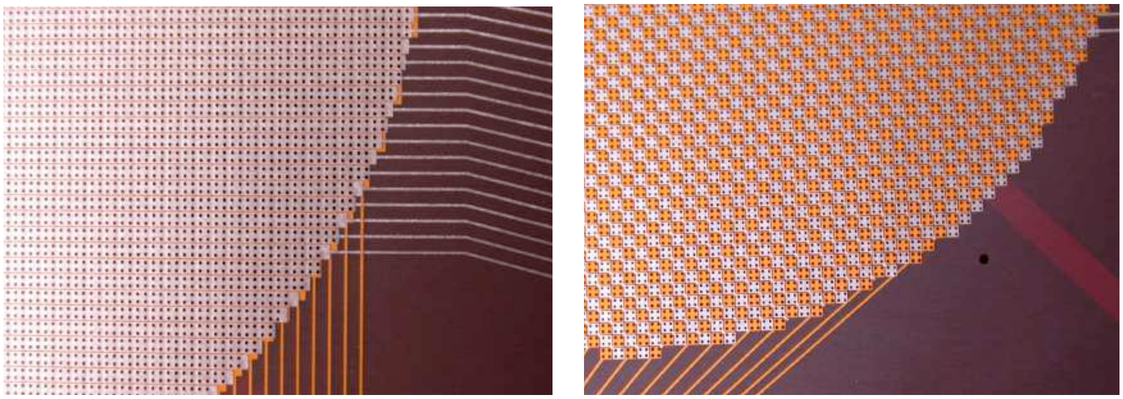

Figure 4.3: SILEM designs : $x-y$ strips version (left) and $x-y$ pixels version (right)

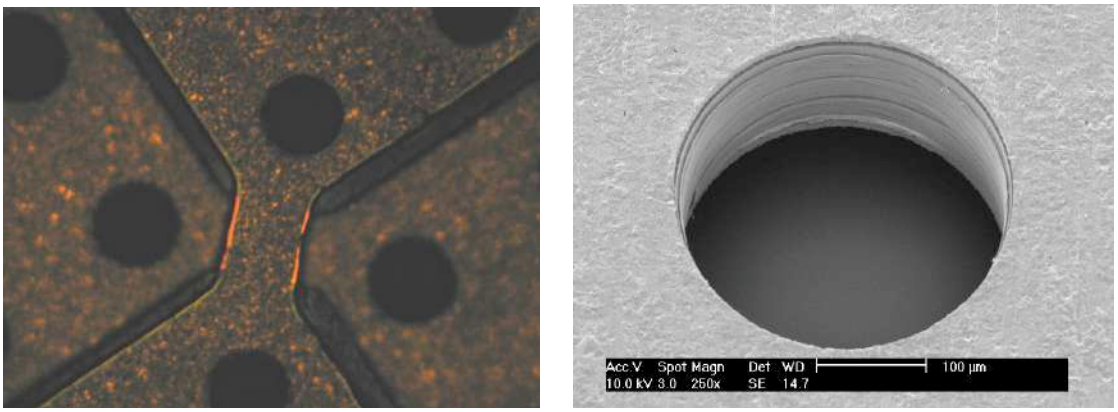

Figure 4.4: SILEM larger views; $x-y$ pixels (left). Hole detail (right)

4.2 Fabrication

SILEM are made of vetronite (printed circuit board) 400 μm thick with 18 μm copper on both sides. The micropattern is engraved in Cu with photolithography techniques. For the case with both $x-y$ readout pixels on the same side, a 20 μm kapton substrate with 18 μm Cu layer on one side is also engraved. It is then aligned and glued on the main vetronite substrate. Square cuts on this 20 μm kapton substrate are cut to open the pixels of the main substrate behind it. These cuts are made by photolithography and never with laser techniques, because laser abrasion

makes conductive bridges between both Cu planes.
LEM holes of 300 μm are then mechanically drilled and a chemical etching of copper is necessary to clean the surface and remove Cu chips near holes borders. This treatment has to be done to avoid "needle" effects, generating breakdowns. Figure 4.5 shows an electron microscope (SEM) picture of a SILEM hole before copper etching.

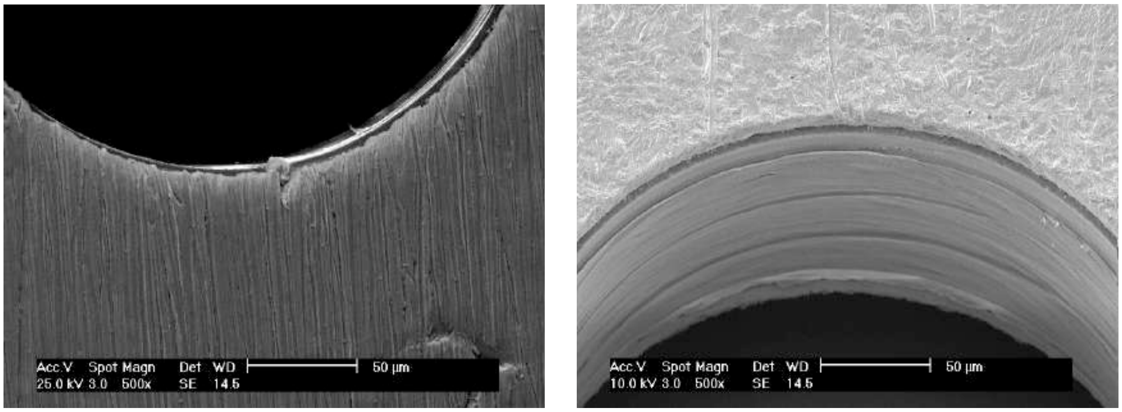

Figure 4.5: SILEM hole before and after Cu etching

A glue stable in time must be chosen. CERN uses a particularly stable Epoxy for this purpose. A bad glue slowly migrates towards LEM surfaces and makes it inoperative.

4.3 Simulation

The LEM was optimized with the Maxwell/Garfield simulation tool from CERN. This is a finite elements analysis software. An irreducible LEM element is drawn, representing the whole grid when applying symmetries. A drift volume with 200 V/cm is represented above the LEM. Geometry, materials and applied voltages are defined in Maxwell. The volume is then segmented in tetrahedrons ($27'000$ tetrahedrons : finite elements) and define a mesh. This is shown on Figure 4.6. Several consecutive calculations are necessary to define these tetrahedrons properly; they have to be as small as possible in the interesting regions (SILEM holes) in order to have the most precise simulation.

Once geometry and tetrahedrons are defined, the applied voltages on the different parts of the grid can be set and modified (drift field, LEM voltage). For each of these adjustments, Maxwell calculates two "field maps", i.e a datafile containing all informations about the geometry of the simulated objects, the mesh, the applied voltages, etc.

1. v : electric potential
2. e : electric field

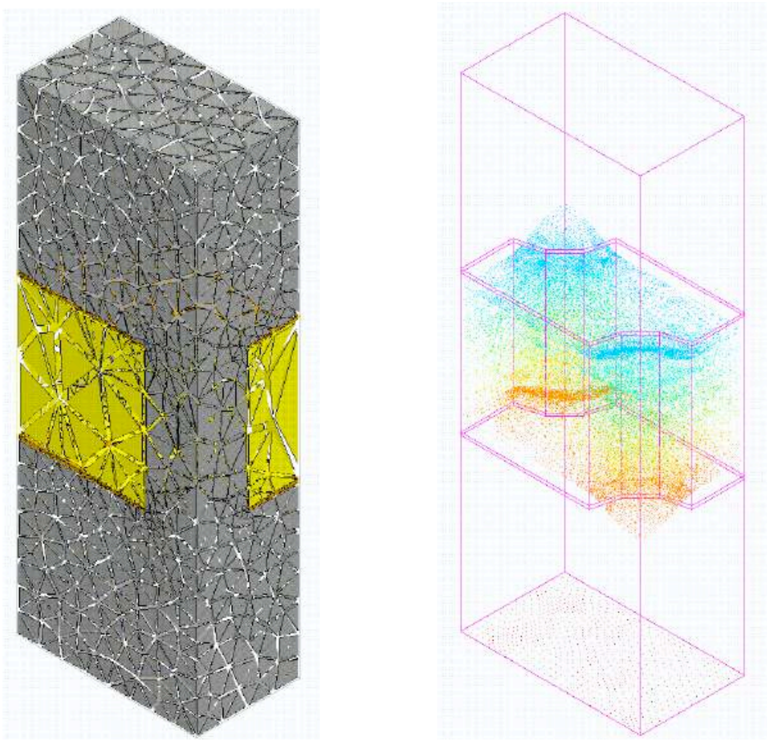

Figure 4.6: SILEM mesh in Garfield/Maxwell (left). The yellow elements represent the insulator substrate (vetronite) and the grey tetrahedrons represent the gas volume, i.e drifting volume + SILEM holes. The right figure shows the field map simulation; the colors represent the electric field values.

Figure 4.6 (right) represents the electic field values simulated in the SILEM element, and particularly in and around the SILEM holes.

Geometry and field maps are then imported in Garfield; a script defines the simulation to be made and the desired output. The used gas (and its pressure, temperature) must be defined; For CF_4 or gas mixtures such as $P10$ ($Ar-90\%$ $CH_4-10\%$), a gas "map" must be calculated.
The output of the simulation were the electric potential and the drift lines in and around the LEM holes, (Figure 4.7), the electric field $\vec{E}$ (Figure 4.8), the grid gain and the avalanche from a single electron deposited in a LEM hole (Figure 4.9). The electric potential, driftlines and electric field depend on grid geometry only, while gain and avalanche depend also on the defined gas and its parameters.

Several LEM geometries were simulated and the optimal ratio between LEM thickness (t) and hole diameter (d) was found to be

$$1 \leq \frac{t}{d} \leq 2$$

- When $t/d < 1$ the development of the electromagnetic shower is too small to ensure a sufficient gain.
- When $t/d > 2$, the hole is too long and the electromagnetic shower stops against the hole walls; moreover, the ion flux shields the hole and obstruct the

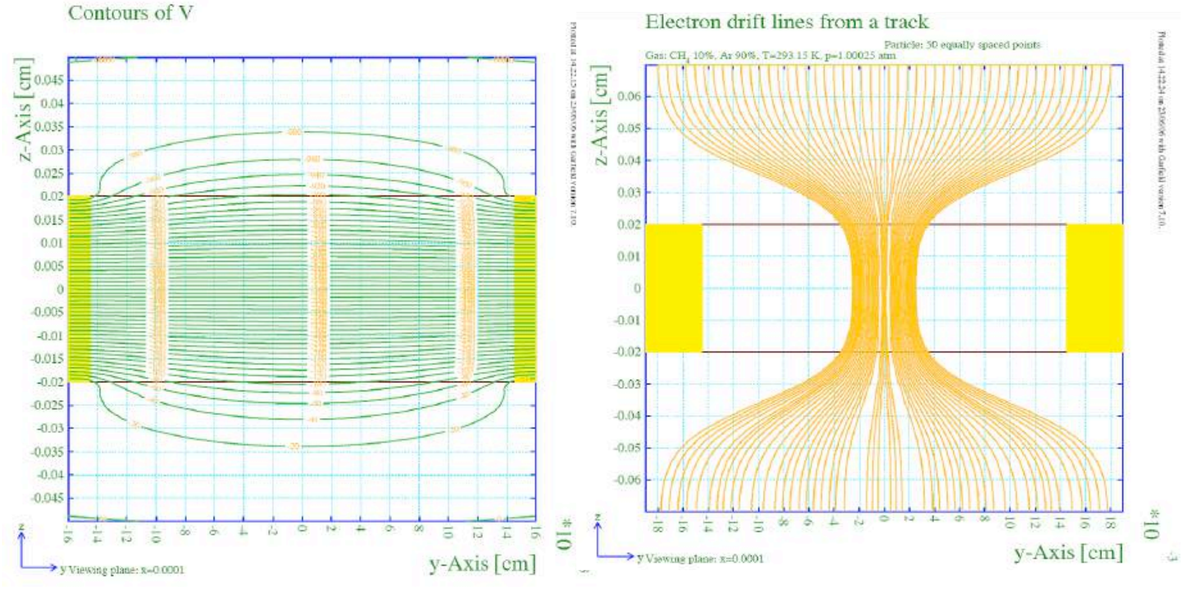

Figure 4.7: SILEM electric potential (left) and driftlines (right).

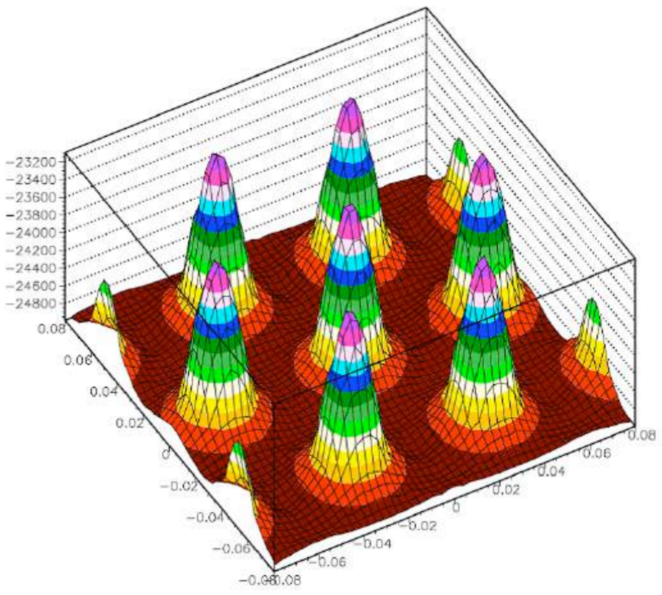

Figure 4.8: Electric field simulated for the SILEM grid.

electrons income.

Gain of the SILEM grid was calculated for $P10$, CF_4 and Xe; a simulation was performed at different gas pressures : 0.1 bar, 0.5 bar, 1.0 bar, 1.5 bar and 2.0 bar at various LEM voltages. Drift field was always 200 V/cm. Figure 4.10 represents the SILEM gain simulated in $P10$.

Maxwell/Garfield gives quantitative results but it does not represent the breakdowns appearing when LEM voltage is too important. A comparison with experi-

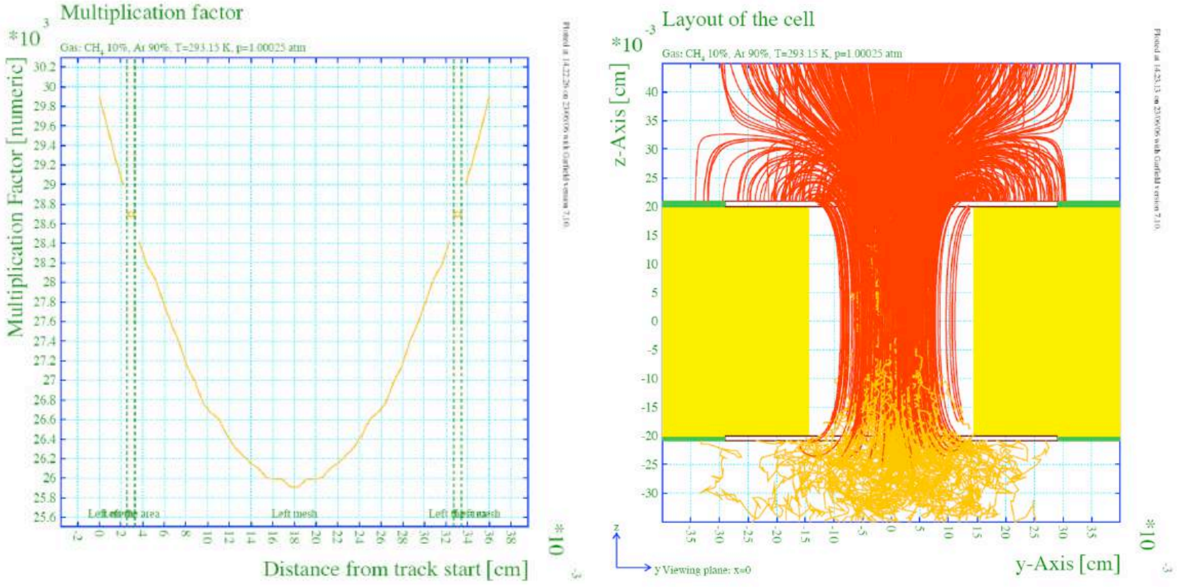

Figure 4.9: SILEM gain (left) and avalanche (right).

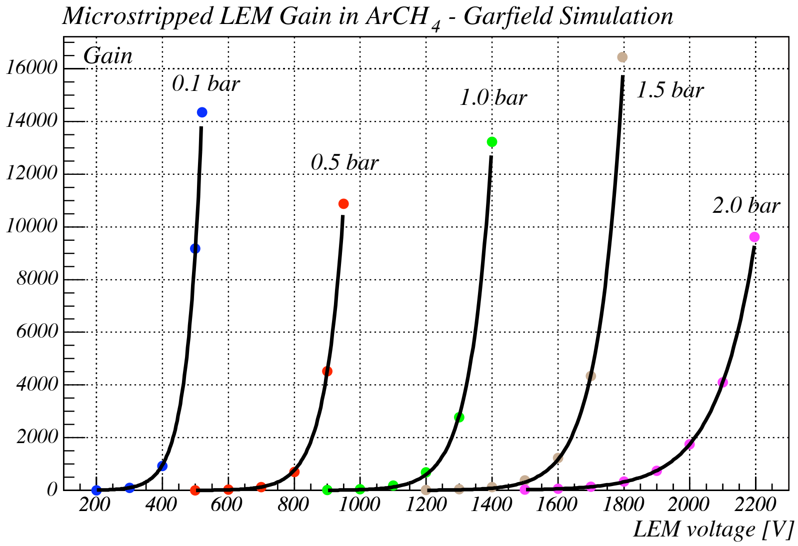

Figure 4.10: SILEM simulation with Maxwell/Garfield in $P10$.

mental values can be found in section 3.5.

4.4 Experimental setup

Amplification grids were tested and characterized in a custom made TPC of ~ 20 liters ($\oslash = 30\ cm$, height $\cong 30\ cm$), equipped with four $2-$inches ConFlats (CF) and three $3-$inches CF feedthroughs. $2''$ CF are used for HV and readout feedthroughs, one $3''$ CF is used for the optical fibers feedthroughs and one $3''$ CF for Xenon recovery.

Vacuum and gas feedthrough are disposed on the removable hat, screwed on the

TPC. A viton o-ring maintains the tightness. Figure 4.11 shows this TPC. The pumping is done with a turbopump; a vacuum of $\sim 10^{-6}$ $mbar$ is achieved. 32 scintillation optical fibers come out off the TPC and are connected on a single anode PMT (Phillips XP2020).

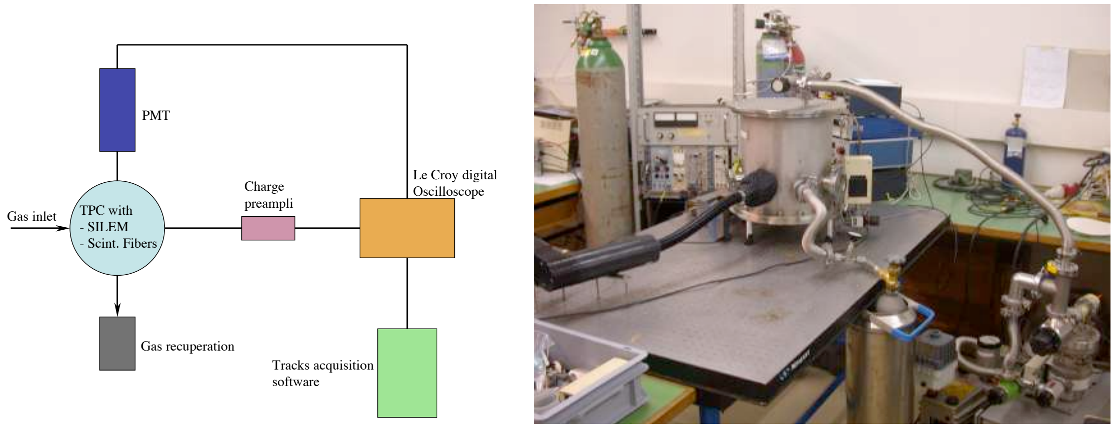

Figure 4.11: Technical drawing of the experimental setup (left). Custom made TPC for SILEM and scintillation light tests (right).

4.4.1 ETHZ charge preamplifier for LEM's

A custom made charge preamplifier from ETHZ was used for the latest measurements with the LEM. This preamplifier was designed especially for LEM's and some parameters such as input impedence were adjusted for SILEM. Figure 4.28 in the Appendix section shows a schematic of this preamplifier. This preamplifier is protected against breakdowns. The amplification factor is ~ 2000 and the output polarity is reversed.

4.4.2 Leakage current

The readout of a charge signal on a LEM needs a very low leakage current, typically $1 - 10$ pA. A clean setup was installed to measure the leakage currents. Cables handling only can induce currents of the nA scale. A LEM cleaning is necessary in a number of cases, in order to have an acceptable leakage current :

- An intensive use of LEM with sparks burns one or more holes. Generally a hole burns when its border is not properly etched.
- When LEM becomes dirty with greasy compounds (fingerprints, etc) or water.

Different cleaning methods are used at CERN, depending on the leakage current

- $10\ pA \leq I_{leak} \leq 100\ pA$: Ultrapure deionized water or isopropanol
- $100\ pA < I_{leak} < 100\ nA$: Potassium permanganate ($KMnO_4$)
- $I_{leak} \geq 100\ nA$: Chemical etching of Cu

4.4.3 ^{55}Fe x-ray source

An x-ray source of ^{55}Fe was used to ionize the gas and generate events in the grid. X-rays from ^{55}Fe are 5.9 keV. They ionize the gas — mainly by photoelectric effect at these energies — generating electrons and their corresponding ions. The electrons are drifted to the amplification grid thank to the drift electric field; ions are thus drifted to the cathode and were not considered in our setup.

4.4.4 Electron drift

Spatial resolution in a TPC depends on electron velocity in the drifting volume. Good energy resolution is obtained with large electron velocity and small transverse diffusion (perpendicular to electron drift). Electron velocity depends on the gas, on its pressure, and on the drift field. Figure 4.12 shows electron velocity in $P10$ gas, as a function of drift electric field and $P10$ pressure.

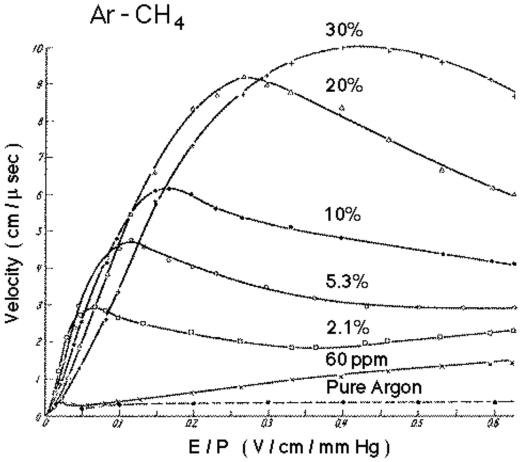

Figure 4.12: Velocity of electrons in P10.

In the case of $P10$, which is Argon with 10% of CH_4, the largest velocity is obtained for

$$\frac{E}{p} \approx 114 \, \frac{V}{cm \cdot bar}$$

These parameters were used to minimize the transverse diffusion.

4.5 Experimental results : characterization of SILEM in $P10$

The SILEM grid was characterized in P10 gas ($Ar - 90\%$, $CH_4 - 10\%$).
Charge signals can be measured on the upper side of LEM (ions) or on the bottom side (electrons). Figure 4.13 represent ions and electrons charge signals.

If charge signals are measured on the side which is at a potential, the output signal has to be decoupled. It can be measured directly on the side which is at

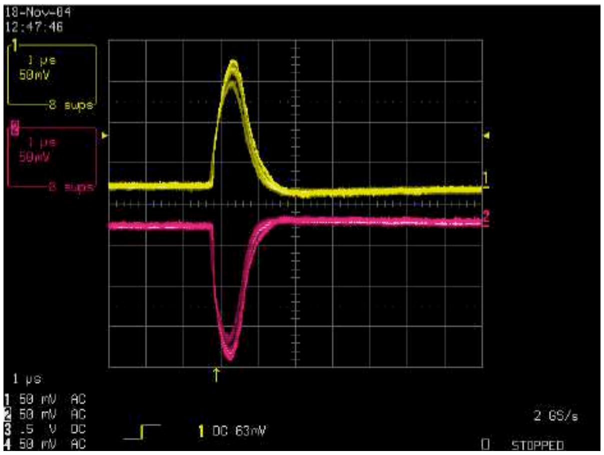

Figure 4.13: Charge signals on SILEM; ions (yellow) and electrons (red).

ground potential. The signal is then amplified with ETHZ charge preamplifier. It is sent to an oscilloscope. A custom-made software records all signals in a datafile. The amplitude of each peak is stored, as shown on Figure 4.14.

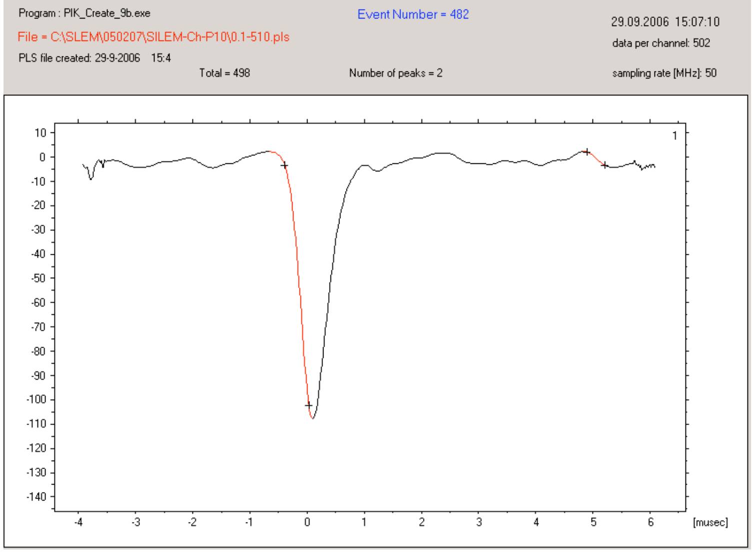
Program : PIK_Create_9b.exe
Event Number = 482
29.09.2006 15:07:10
File = C:\SLEM\050207\SILEM-Ch-P10\0.1-510.pls
data per channel: 502
PLS file created: 29-9-2006 15:4
Total = 498
Number of peaks = 2
sampling rate [MHz]: 50

Figure 4.14: SILEM charge signal in $P10$.

The same software is then able to fill histograms with the stored data; a scatter plot in time is shown on Figure 4.15. Charge events have time $t \simeq 0$ and amplitudes (in mV) above background. It is also possible to select only the interesting events on the scatter plot, as shown on Figure 4.15. ~ 1000 events are stored for each SILEM voltage. The mean amplitude defines the gain of the given voltage and the RMS value of the peak allows to calculate the resolution for the given parameters. A charge signal peak is shown on Figure 4.16.

Data were recorded for various LEM parameters

- gas : $P10$, CF_4 and Xe

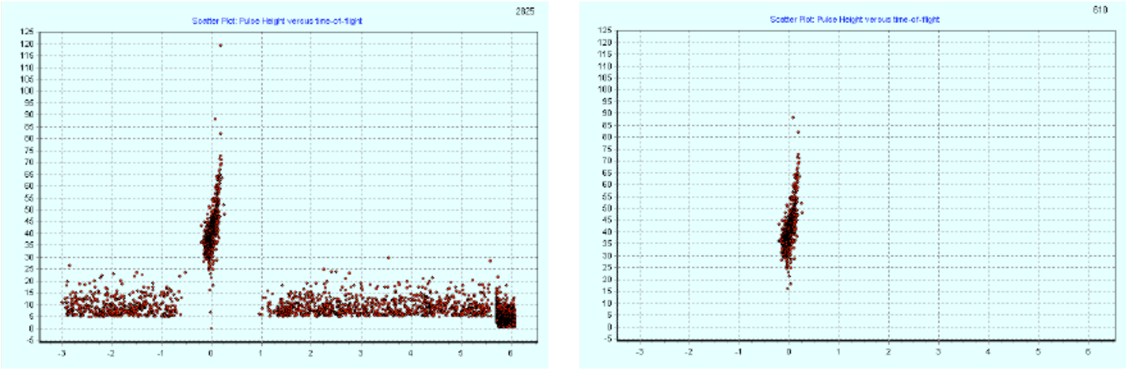

Figure 4.15: Scatter plot of SILEM charge signals with background (left) and with supressed background (right). The amplitude of the signals (in mV) are plotted as a function of the time position (μs).

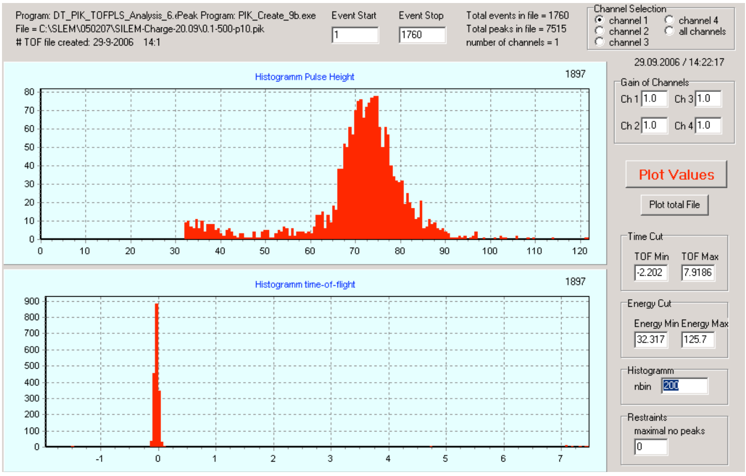
Program: DT_PIK_TOFPLS_Analysis_6.‹Peak Program: PIK_Create_9b.exe
File = C:\SLEM\050207\SILEM-Charge-20.09\0.1-500-p10.pik
# TOF file created: 29-9-2006 14:1

Event Start: 1
Event Stop: 1760

Total events in file = 1760
Total peaks in file = 7515
number of channels = 1

Channel Selection
● channel 1 ○ channel 4
○ channel 2 ○ all channels
○ channel 3

29.09.2006 / 14:22:17

Gain of Channels
Ch 1: 1.0 Ch 3: 1.0
Ch 2: 1.0 Ch 4: 1.0

Time Cut
TOF Min: -2.202 TOF Max: 7.9186

Energy Cut
Energy Min: 32.317 Energy Max: 125.7

Histogramm
nbin: 200

Restraints
maximal no peaks: 0

Figure 4.16: SILEM charge signals in $P10$ (0.1 bar, 500 V, ^{55}Fe source). A plot of the signals amplitude is represented on the upper part. The time plot is represented on the bottom part.

- gas pressure : $0.1 - 2.0\ bar$
- SILEM voltages.

The 5.9 keV peak of ^{55}Fe in $P10$ is represented on Figure 4.17. A gaussian was fitted for each peak; the gain for given parameters (gas, pressure, voltage) is proportional to the mean amplitude of the peak, while the resolution R is given by

$$R = \frac{\sigma_{fit}}{center} = \frac{RMS}{mean}$$

A is the charge signal amplitude of the peak and $\sigma(A)$ the error on this amplitude, given by the RMS value of the fit.

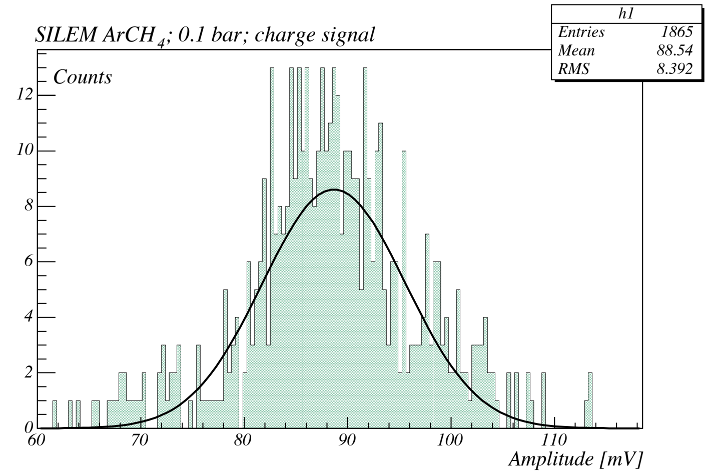

Figure 4.17: SILEM resolution with ^{55}Fe source.

4.5.1 SILEM Gain

The gain G of a LEM (or multiplication factor) is related to the amplitude of the charge signal with the following relation

$$G = \frac{C\ w}{e\ E}\ U$$

where C is the preamplifier input capacitance, w the ionization energy of the gas E the x-ray energy and U is the signal amplitude before preamplification. In our case, we have

- $C = 1\ pF = 1\ 10^{-12}\ F$
- $w = 26.2\ eV$ for $P10$
- $E = 5.9\ keV$
- $e = 1.6\ 10^{-19}\ C$

In the case of $P10$, this makes $G = 2.775\ 10^4\ U$.

Figure 4.18 shows the SILEM gain at various $P10$ pressures. The gain was measured until breakdowns were observed. The point with the higher voltage on each curve represent the limit before breakdowns. Our preamplifier allows us to measure gains down to ~ 500. It was possible to measure charge signals in $P10$ with pressures up to 2 $bars$.

Although errors on the gain almost fit the simulation, the differences between data and simulation can be explained with two factors

- The diffusion in Garfield is simulated with an error of ±20% compared to real data.

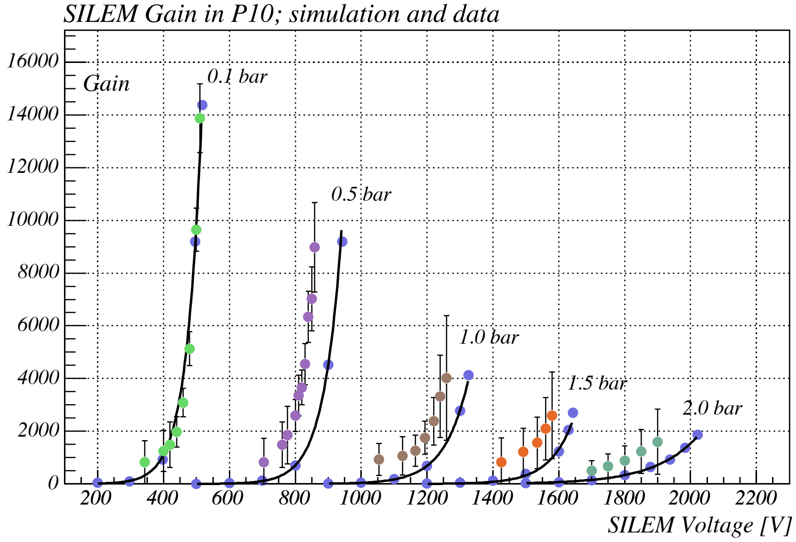

Figure 4.18: SILEM gain in $P10$. Measured gain has error bars and simulation has an exponential fit.

- Garfield simulation of SILEM was done with $400 + 18\mu m$ thickness (vetronite + 2 copper layers of 9 μm), but did not took into account the thin kapton+Cu layer of 20 μm. A thinner simulated grid (20%) makes a corresponding smaller gain.

SILEM resolutions in $P10$ are shown on Figure 4.19.

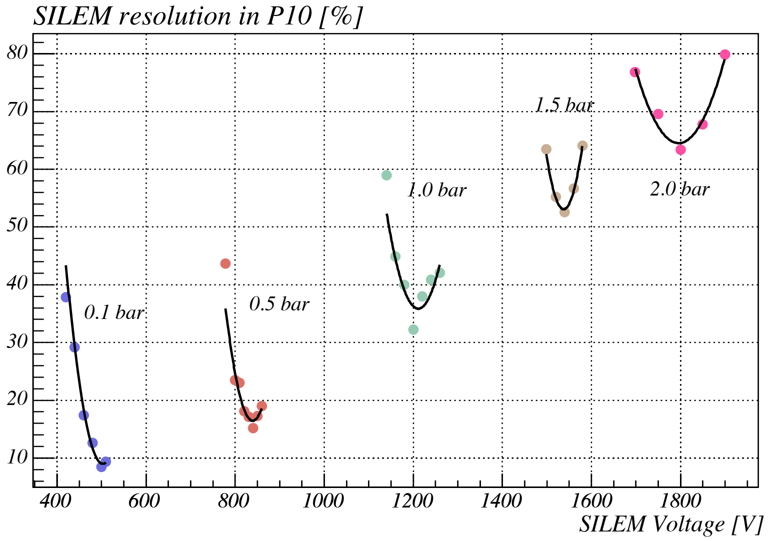

Figure 4.19: SILEM resolution in $P10$.

One can see on Figure 4.20 that the gain is inversely proportional to the gas pressure

$$G \propto \frac{|\vec{E}|}{p}$$

which is a typical behavior of GEM and LEM.

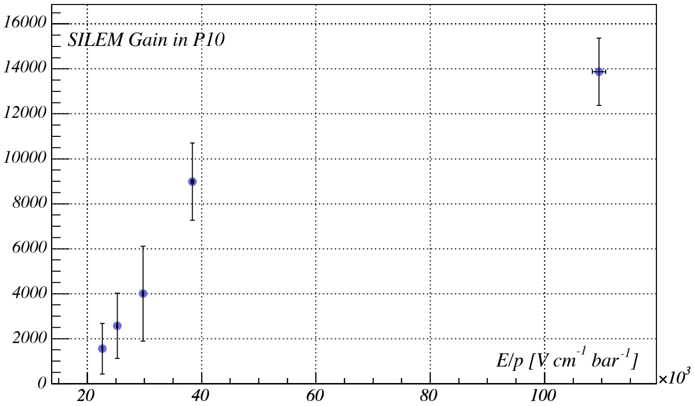

Figure 4.20: SILEM Gain in $P10$, as a function of the parameter E/p.

4.5.2 Strips acquisition

${}^{55}Fe$ source was collimated to make a $\sim 4 \times 4\ mm^2$ spot on the LEM, i.e to irradiate $\sim$ 4 pixels of the SILEM grid. Charge signals were measured in $x - y$ pixels under the collimation region. 10 pixel lines were measured in the x direction and 10 others in the y direction. Strips were measured successively.

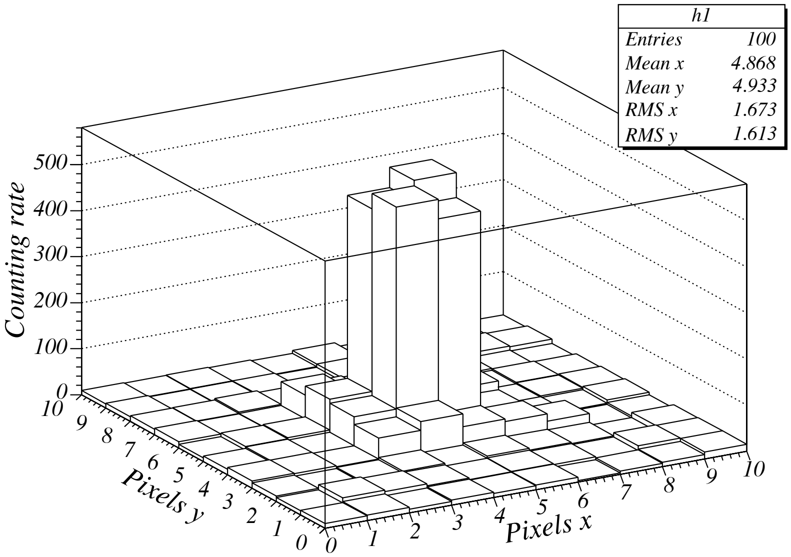

Figure 4.21: SILEM Gain in $P10$, as a function of the parameter E/p.

Figure 4.21 shows the counting rate of each individual pixels of the SILEM grid. Horizontal diffusion of primary electrons originated from ${}^{55}Fe$ x-rays source can

explain the counting rate of the neighbouring pixels.
The SILEM allows to know through which holes the primary electrons went, and thus reconstruct an $x - y$ projection of the original particle's track. The SILEM resolution is submillimeter.

4.6 Scintillation in a TPC

An array of 32 scintillating optical fibers [1] was installed in the TPC. The initial goal was the realisation of a readout plane with 32 x and 32 y fibers, connected to 64 channels photomultipliers, and the corresponding electronics, such as the one developped in the OPERA collaboration with Hammamatsu 3840 PMT's [10]. The first step was then a measurement of secondary scintillation, i.e. photons generated during avalanche in the amplification grid, with scintillating fibers.

4.6.1 Physics of the scintillation process

Light emission during de-excitation and ion recombinations is a complex process. Various transitions can occur

- *Optical levels*; the atom A returns to the ground state with successive allowed transitions to lower excited states.
- *Resonnance levels*; the atom is able to return directly to the ground state, without passing through intermediate excited states.
- *Metastable levels*; the transition to lower levels — and in particular to ground level — are forbidden by quantum selection rules.The lifetime is only limited by collisions.
- *Excited dimers*; Double and triple collisional processes with metastable excited atoms.

Primary scintillation

Evolution of atomic state in rare gases strongly depends on the gas pressure.

- At very low pressures, $p < 10^{-4} mbar$, one has direct transitions from resonnant states to ground states optical levels, with typical times of $10 - 100$ ns.

$$A^*_{resonnance} \longrightarrow A + h\nu \ (VUV)$$

- At low pressures, $p < 10 mbar$, the lifetime of atomic lines increases because of radiation retention [7]. Resonnant radiation with $1 - 10 \mu s$ hardly goes out because it is reabsorbed by atoms in the ground state. Intensity of atomic

---

[1] Saint-Gobain; type BCF-12; $1mm$

lines decreases from $p > 10^{-4} mbar$ and other radiation channels appear, such as diffusion in the gas or on the walls, proportional to the pressure

$$A^{**} + A \longrightarrow A_2^{+} + e^{-}$$

One has also Hornbeck-Molnar reactions

$$A^{*}_{metastable} + A \longrightarrow A + A + E_{cin}$$

occuring for every noble gases at every pressures, but need excitation energies above a given value, i.e. $23.18 eV$ in the case of He.

- For pressures $p > 150 mbar$, atomic lines vanish and reactions such as

  $$A^{**} + A \longrightarrow A^{*} + A + E_{cin}$$

  appear, together with Hornbeck-Molnar reactions. Three-bodies reactions are responsible for primary scintillation of rare gases [8]

  $$A^{*} + 2A \longrightarrow A_2^{*} + A$$

  where

  $$A_2^{*} \longrightarrow A + A + h\nu \ (VUV)$$

  These ultraviolet photons are emitted in an energy continuum. The ground state of the molecule is repulsive; and according to relative position of atoms within the molecule when emission takes place, the potential will be more or less repulsive, allowing a broad range of photon energies. For the same reason, the scintillation will not be reabsorbed in the gas, because the is no molecule in the ground state (Excited dimers).

  Adding impurities in very small quantities ($< x\ ppm$) has two effects

  1. *Ionization increase*, due to decreasing of the w-value, mean energy to create a pair electron-ion (Jesse effect, [6]).
  2. *Scintillation intensity decreases*, proportionnaly to the impurity concentration C_{imp} and total pressure p

     $$L^{VUV}_{mix} = L^{VUV}_{pure} \cdot C^{-p}_{imp}$$

     The scintillation lifetime is also decreasing, proportionnaly to impurity partial pressure.

Secondary scintillation

The high electrical field in the amplification region is able to give electrons enough energy between collisions to excite and ionize the gas atoms; the radiative desexcitation is called secondary scintillation. A threshold value of E/p can be calculated, necessary for having secondary scintillation. In the case of $P10$ and Xe, one has

$$\frac{E}{p} \geq 750 \ \frac{V}{cm \cdot bar}$$

Secondary scintillation emits much more photons than primary scintillation; this factor is proportional to the gain of the amplification stage. The consequence is a better resolution. The light emitted in the secondary scintillation varies with gas pressure as [8]

$$\frac{L}{p} \sim \left[\frac{E}{p}\right]^{1.5-2.5}$$

4.6.2 Experimental setup

Secondary scintillation was measured using scintillating optical fibers Saint-Gobain, type BCF-12. Figure 4.22 represents absorption and emission spectra of BCF-12 fibers.

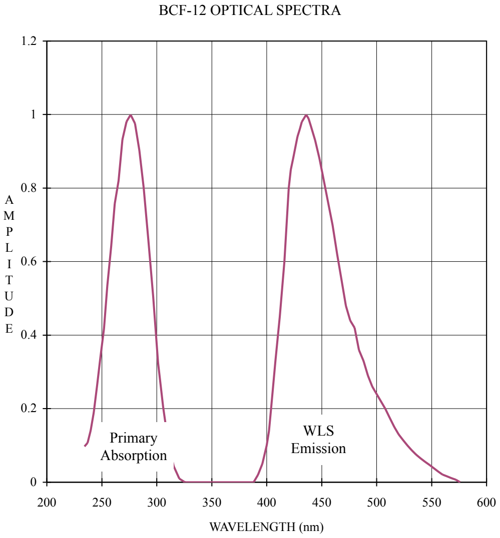

Figure 4.22: Absorption and emission spectra of BCF-12 fibers.

This fiber is able to detect soft UV photons from ~ 170 nm (with poor efficiency). It was thus possible to measure 178 nm photons from Xe scintillation. The large scintillation emission in Xe compensates the poor absorption efficiency of the fibers in that case.

Feedthroughs for optical fibers was a technical problem in order to have a tight TPC; the 32 fibers are passing through a delrin machined piece; they have 2 o-rings on each side of the delrin and 2 plates are screwed on each side and press this sandwich together, so that o-rings are under pressure, ensuring tightness of the TPC. This setup is shown on Figures 4.23 and 4.24.

4.6.3 Secondary scintillation measurements in P10

The scintillation spectrum in $P10$ has 3 main peaks : 315 nm, 390 nm and 430 nm, as represented on Figure 4.25.

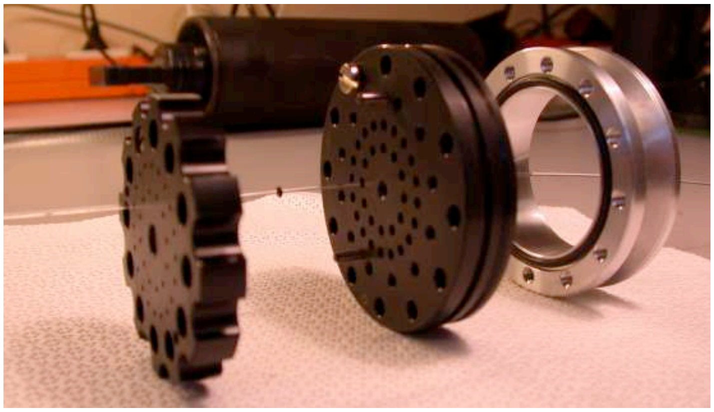

Figure 4.23: Feedthroughs for optical fibers.

Figure 4.24: Feedthroughs for optical fibers; detail.

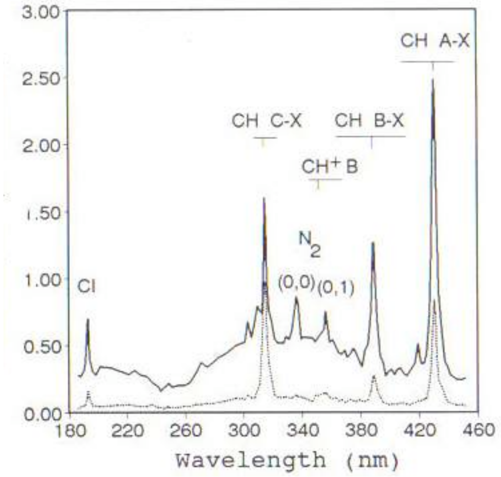

Figure 4.25: Emission spectrum of $P10$ gas.

Both charge and secondary scintillation signals were recorded. Figure 4.26 shows charge signals (down) and scintillation (up) for two different gains; at low gain (corresponding to $V_{SILEM} = 580\ V$) on the left image and a higher gain (corresponding to $V_{SILEM} = 630\ V$) on the right image. Figure 4.26 shows permanent tracks recorded on the oscilloscope. The colors depend on the occurence of a track depending on its position. The red track is the last recorded.

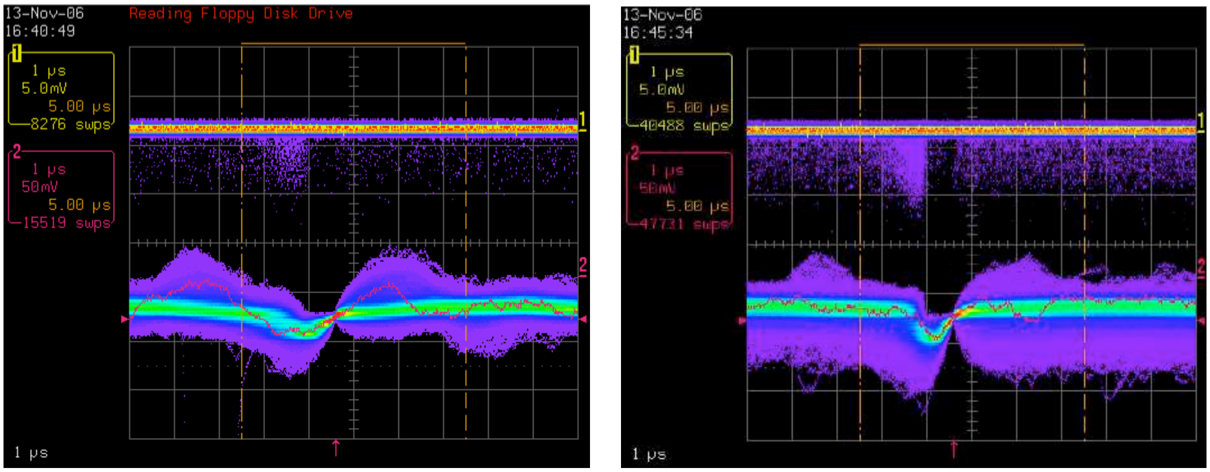

Figure 4.26: SILEM Charge and Light signals in $P10$; Low gain (left) and higher gain (right).

At low gain (left), the charge signal is small and we measure a few scintillation signals during the avalanche time, which is $\sim 1-2\ \mu s$. At higher gain (right), the charge signal is bigger and we measure much more scintillation. Scintillation signals have rise times of $\sim 1-3\ ns$, which is consistent with BCF-12 decay time of 3.2 ns. The amplitude of the scintillation signals remain constant with increasing gain, which indicates that we are measuring individual photons signals in the fibers during the avalanche. The amplitude of scintillation signal increases by a factor n ($n = 2, 3$) when n photons are measured at the same time in the fiber.

A plot of the light yield (number of scintillation signals per time unit) as a function of the LEM voltage, represented on Figure 4.27, shows that the secondary scintillation is following the SILEM gain. We have thus a correlation between ionization and secondary scintillation.

Electrons resulting from the avalanche have energies of 5.9 keV. These electron energies are not large enough to generate a scintillation of the fibers; a clear signal can be measured in the fibers with a ^{90}Sr source (electrons of $\sim 2\ MeV$), but no signal for ^{137}Cs source, which have electrons of $\sim 1.1\ MeV$.
One therefore checked it in the TPC by adding a 100 μm mylar film between the amplification grid and the optical fibers. Mylar is transparent to photons from the UV to the visible, but electrons with 6 keV penetrate only $\sim 3\ \mu m$ in plastics, so that they are stopped by the mylar film. One observed the same signal with and without the mylar film. This confirms that the optical fibers are measuring photons from the avalanche and the signal is not due to electrons.

4.6.4 Primary scintillation

It was not possible to measure primary scintillation in $P10$ with our optical fibers. A configuration without amplification system (LEM) was used, with only a cathode,

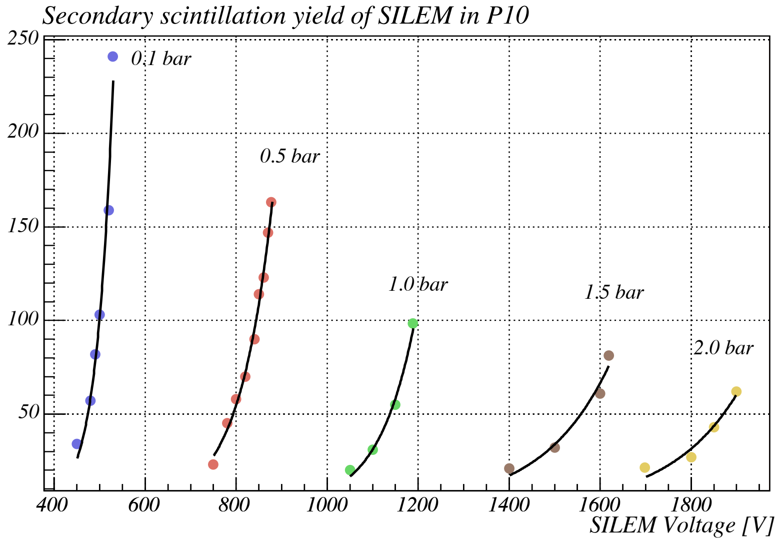

Figure 4.27: LEM secondary scintillation in $P10$, measured with optical fibers array.

an anode and the optical fibers array in between. The weakness of primary scintillation signal made it impossible to detect.

4.7 Discussion

- SILEM grid is a suitable "all-in-one" system for electron amplification and readout. It was optimized for better gains and works in $P10$ with pressures up to 2.0 bars. Moreover, it was possible to perform an $x - y$ readout of secondary electrons with a resolution of the size of a pixel ($1\ mm^2$). The next step would be the track detection of real particles crossing the TPC, such as cosmic muons. This would need an electronic acquisition system with at least 16 channels. Theoretical extrapolated resolutions around 2 MeV, suited for double-beta experiments show exhibit promising results. In the case of ^{136}Xe, the Q value of $0\nu\beta\beta$ is 2457.83 keV, leading to SILEM resolutions around :

  $$R@2\ bar \sim 0.15\%$$

  Machining of large SILEM seems realizable, as standard photolithography techniques allow structures patterning up to 60 cm. Larger grids could be machined with several lithography steps. An alignment of $\sim 100\mu m$ would be enough. Holes are drilled mechanically, so that grids are essentially not limited in size.

- Optical fibers represent a possible complementary readout plane, allowing secondary scintillation photons measurements, working in $P10$, CF_4 and Xe. 32 other fibers, perpendicular to the existing array, combined with a multianode photomultiplier would form an efficient 64 channels readout plane.

4.8 Appendix

Figure 4.28 shows a scheme of the pramplifier used for these tests; it was optimized for charge measurements with LEMs.

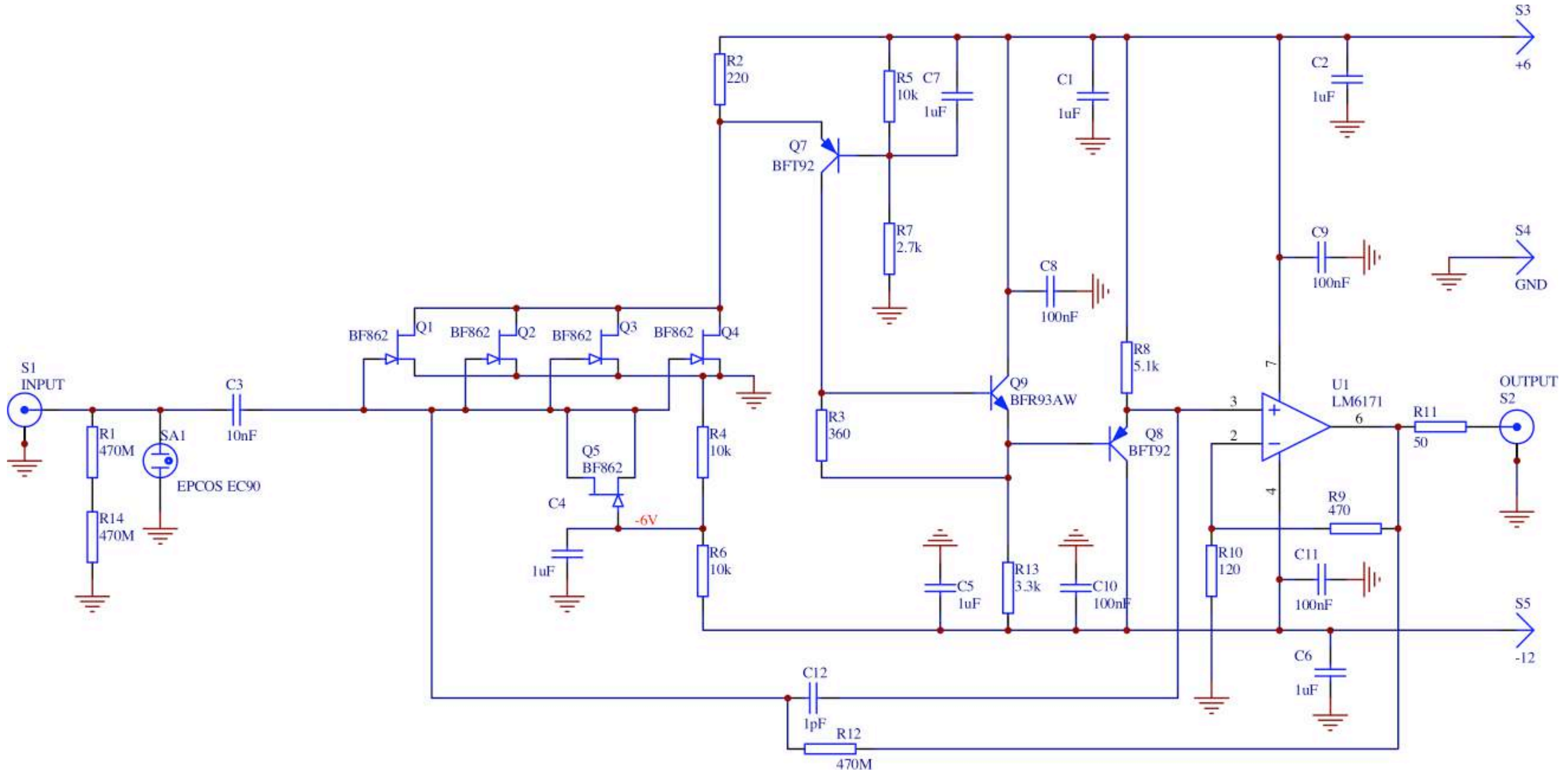

Figure 4.28: ETHZ charge preamplifier for LEM's.

Bibliography

[1] A.Oed; NIM A 263 (1988), 351.

[2] I.Giomataris et. al; NIM A 376 (1996), 29-35.

[3] GEM : A new concept for electron amplification in gas detectors; F.Sauli; Nuclear Instruments and Methods NIM A 386 (1997), 531-534.

[4] Time projection chambers and detection of neutrinos; Thesis from the Physics Dept. of Neuchâtel University; P.Jeanneret

[5] The sand-glass gas detector (SGG); P.Majewski et. al; NIM A 478 (2002); 190-195.

[6] Ionization by alpha particles in mixtures of gases; Jesse et al.; Phys. Rev. 100 (1955); 1755.

[7] Imprisonement of resonance radiation in gases; T.Holstein; Phys. Rev. 83 (1951); 1159.

[8] Pressure dependence of light output in rare gases and their mixtures; Leite et al.; NIM 198 (1981); 587.

[9] Correlated fluctuations between luminescence and ionization in liquid xenon; E.Conti et. al., EXO collaboration; Phys. Rev. B 68 (2003)

[10] The OPERA experiment target tracker; OPERA collaboration; submitted to NIM

Chapter 5

Germanium data counting for EXO

Background reduction is a crucial task in experiments such as double-beta decay. Events are so rare that they cannot be lost in radioactive background events. In this sense, rare-event detectors are designed to have a background signature as small as possible and thus, detector parts have to be made in ultra-low radioactivity materials.

Materials for EXO detector have to be carefully selected. Samples of material candidates are measured with different techniques :

- Mass Spectrometry (AMS); Canadian Standards
- Germanium gamma counting; University of Neuchâtel
- Neutron activation; University of Alabama
- Radon emanation; Laurentian University

Mass spectrometry is the most sensitive, but germanium gamma counting really measures the photons decaying in the sample. In this sense, this technique is the most realistic. Moreover, germanium measurements take into account the whole decay chains of Uranium-238 and Thorium-232. This allow to tell if these chains are in equilibrium or not.

5.1 Germanium detector

Our Germanium detector is a p-doped 400 cm^3 low-noise made fom Eurisys-Mesures. It is located in the road tunnel of "La Vue-des-Alpes", above Neuchâtel [2] [1], providing a shielding against cosmics, corresponding to 600 meters water equivalent, reducing the muon flux by a factor 1000. The detector is also shielded against the rock radioactivity with ultraclean lead (20 cm) and copper (15 cm), as shown on Fig 5.1.

A protection was added last year above the detector to avoid dust from the lab entering the detector when it is opened. Figure 5.2 shows this protection

---

[1] webpage : http://www.unine.ch/phys/

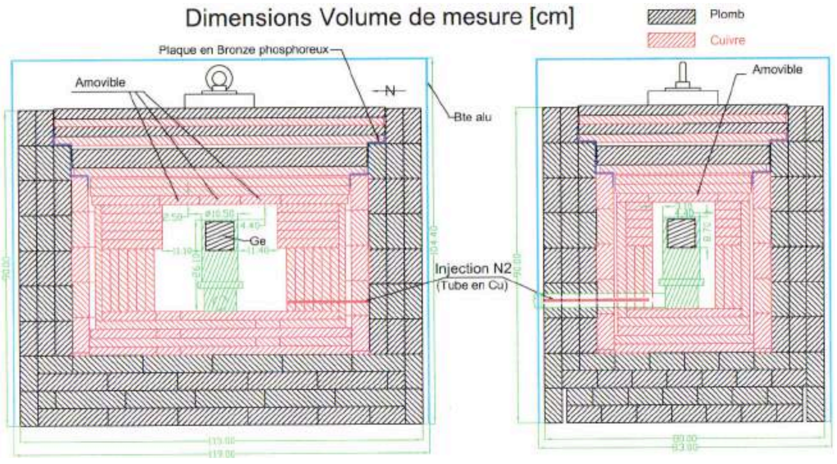

Figure 5.1: Germanium detector scheme.

Figure 5.2: Germanium protection against dust.

The detector is finally shielded from the remanent radon present in the air of the lab, thank to a nitrogen overpressure replacing the air around the Ge in a few hours.

After substraction of the radioactive background due to Pb and Cu shielding, one can achieve sensitivities down to $\sim 10^{-10} g/g$ for natural decay chains of ^{238}U, ^{232}Th, ^{40}K and $\sim 10^{-20} g/g$ for short-lived radioisotopes such as ^{137}Cs, ^{60}Co and ^{22}Na

5.2 Isotopes measured

Radioactivity of a sample comes from different sources [1]

- **Natural gamma activities :** natural decay chains of ^{238}U, ^{232}Th and ^{40}K. All decays involved in those chains are present in any material containing ^{238}U, ^{232}Th and ^{40}K. Almost every sample contains those unstable isotopes. Moreover, radon (^{222}Rn, from the ^{238}U chain) dissolved in the air is an important source of background and this has to be taken into account. Radon decay leads to the next isotopes in the uranium decay chain, and shows in particular important activities for the ^{214}Pb and ^{214}Bi decays. An overpressure is kept in the detector volume, avoiding radon to enter. A "radon reset" is performed after 24 h of counting, i.e sample counting begins after 24 hours , time needed to expel ^{222}Rn out from the germanium volume (see section Radon shielding 4.7).

- **Artificial gamma activities :** long lived fission products coming from human activities and from the Tchernobyl accident for example. ^{137}Cs, ^{134}Cs and ^{152}Eu are such isotopes.
- **Neutron cosmogenic activation :** The detector is shielded against cosmic neutrons, but the samples and the detector parts were exposed to the neutron flux before they came in the tunnel. The copper used for the shielding has been activated by neutrons and this leads to nuclear reactions that emits gammas. In particular, ^{56}Co, ^{57}Co, ^{58}Co, ^{60}Co and ^{54}Mn are representative isotopes.
- **soldering :** The solders used for electrical connections contain unstable isotopes, in particular ^{125}Sb, ^{207}Bi and ^{110m}Ag.

Those unstable isotopes have been listed in Table 6.1. Figure 5.8 shows ^{238}U natural decay chain and the corresponding emitted photons that we measure.

The relative intensity (I_{rel}) is the probability to have a photon in a given decay. Beside these direct lines, other peaks (indirect) can be observed on the gamma spectra

- 511 keV peak due to e+/e- annihilation of β^+-emitters
- escape peaks : $E_\gamma - 511\ keV$
- pile-up peaks : $511\ keV + E_\gamma$

5.3 Monte-Carlo simulation

A quantitative analysis needs to take into account various parameters such as self-absorption and Germanium efficiency as a function of sample geometry. A Monte-Carlo simulation is done on each sample for this purpose. This Monte-Carlo runs under GEANT3, a particles physics tool from CERN. The implemented parameters are sample mass, dimensions and chemical composition. An efficiency parameter is then given for each gamma peak. Figure 5.3 represents Germanium efficiency (with no sample) as a function of energy.

For any sample added in the simulation, one has a shielding or self-absorption factor decreasing the global efficiency factor. The values are thus always smaller when a sample is placed in the detector. Figure 5.4 represents simulated efficiency parameters calculated with GEANT 3. This example shows seven meteorites of the same type L5 (see Chapter 5). They have thus the same density and chemical composition. The only varying parameters are the dimensions (and mass). One can clearly see the influence of the sample geometry on the efficiency simulation.

	Isotope	$T_{1/2}$	γ energy (keV)	Rel. Intensity
^{238}U	^{214}Bi	19.7 min	295.2	19.5%
	^{214}Pb	26.8 min	351.9	37.6%
	^{214}Bi	19.7 min	609.3	46.1%
	^{214}Bi	19.7 min	1120.3	15.1%
	^{214}Bi	19.7 min	1764.5	15.4%
^{238}U	^{226}Ra	1590 yr	186.2	3.6%
	^{234}Pa	1.14 min	1001.5	0.03%
^{232}Th	^{212}Pb	10.64 h	238.6	100%
	^{228}Ac	6.15 h	338.3	11.3%
	^{208}Tl	3.05 m	583.2	28.1%
	^{208}Tl	3.05 m	860.6	12.5%
	^{228}Ac	6.15 h	911.2	25.8%
	^{228}Ac	6.15 h	968.9	15.8%
	^{208}Tl	3.05 m	2614.5	38.0%
^{40}K	^{40}K	1.27 10^{9} yr	1460.9	99.5%
Artificial	^{152}Eu	13.2 yr	344.3	24.5%
	^{152}Eu	13.2 yr	1112.0	12.0%
	^{137}Cs	30.2 yr	661.7	85.0%
	^{134}Cs	2.1 yr	604.6	97.0%
Cosmogenic activation	^{65}Zn	244.1 day	1124.5	51.0%
	^{60}Co	5.3 yr	1332.5	100%
	^{60}Co	5.3 yr	1173.2	100%
	^{58}Co	70.8 day	810.8	99.0%
	^{56}Co	78.8 day	846.8	100%
	^{56}Co	78.8 day	1238.3	67.6%
	^{54}Mn	312.2 day	834.8	100%
Other	^{207}Bi	38.3 yr	1063.4	74.0%
	^{125}Sb	2.7 yr	635.9	11.5%
	^{110m}Ag	252.2 day	884.7	75.0%
	^{110m}Ag	252.2 day	937.5	33.0%

Table 5.1: Principal unstable isotopes.

5.4 Germanium detector background

The germanium detector is shielded with 15 cm lead and 20 cm low activity copper. Even if these materials were selected for their ultralow radioactivity, some unstable isotopes still remain in very small quantities, leading to a radioactive background, as shown on Figure 5.5. This spectrum is a 510 hours (21.28 days) measurement, and this is ~ 3 times the counting time of a standard measurement.

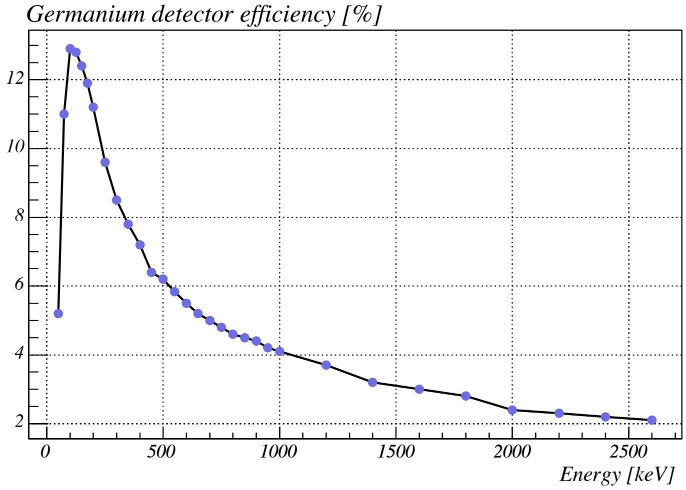

Figure 5.3: Germanium detector efficiency (without sample).

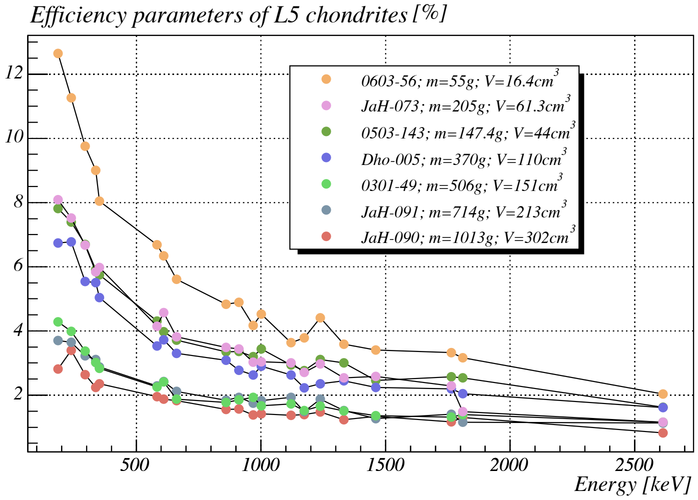

Figure 5.4: GEANT 3 simulation of germanium detector efficiency parameters. This ilustrate the effect of the sample size and mass on the simulation

5.5 Measurement method

5.5.1 Sample preparation

Samples with biggest mass are chosen to achieve best sensitivities. However, the volume around the detector is limited, so that a compromise has to be found. Samples are cleaned in ultrasonic bath of pure isopropanol with heating. Cleaning time is typically 15 minutes.
One observed a ^{137}Cs activity on various phosphor-bronze samples. In order to ensure that this was not a surface contamination of the samples, we performed a chemical etching of the surface with the corresponding solution : Phosphoric acid 69.7% - Nitric acid 42^o Baumé 23.2% - Acetic acid 6.6% - hydrochloric acid 0.4%); this provided an etching rate of 2 $\mu m/min$.

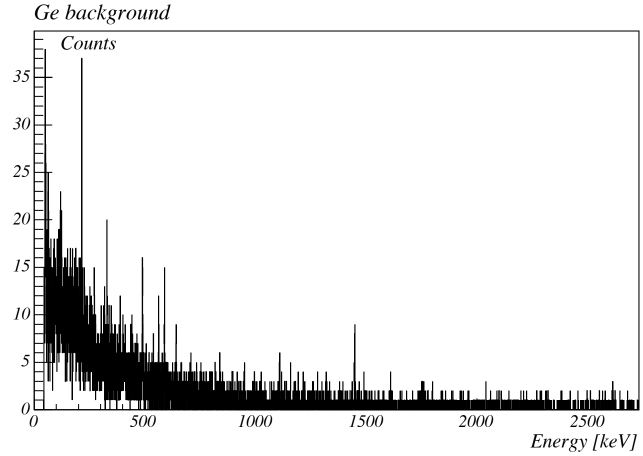

Figure 5.5: Germanium detector radioactivity background. Counting time: $t = 510\ h$.

The samples are then stored in a polyethylene bag that has no incidence on counting. It is placed on top of the germanium detector. Standard counting time is usually one week per sample.

5.5.2 Analysis

Gamma peaks are counted manually; this suits better to reality, in comparison with softwares that plot a gaussian on each peak. Softwares are useful for well defined peaks, but in the case of low-radioactivity samples, there is an important difference between the effective number of counts and the surface under a fitted gaussian.

The width (number of channels) of the different peaks were defined with a rather radioactive sample showing well characterized peaks. Each peak has thus a given width (c channels). The number of counts in these c channels is given, as well as the error, which is defined as the counts in the c channels next to the peak. The error is generally taken to the right of the peak (there is often Compton background to lower energies). A mean on $2c$ or $3c$ channels is also possible to minimize the error. The peak has thus $N_1 \pm \Delta N_1$ counts, and the background, next to the peak $N_2 \pm \Delta N_2$ counts. As $\Delta N_i = \sqrt{N_i}$ for a Poisson distribution, we have

$$N = N_1 - N_2$$

$$\Delta N = \sqrt{\Delta N_1^2 + \Delta N_2^2} = \sqrt{N_1 + N_2}$$

The number of counts is then divided by the counting time t and the relative intensity of the peak

$$\frac{N \pm \Delta N}{t\ I_{rel}}\ (counts/day)$$

The same procedure is applied on the Germanium background spectrum. Each gamma peak has thus a given number of Counts/day and the corresponding error $(G \pm \Delta G)$

The Ge background is then substracted from the sample, and one has

$$(N - G) \pm \sqrt{\Delta N^2 + \Delta G^2}$$

Finally, this is divided by the efficiency parameter and by the sample mass. The units are also set to have the result in Becquerel (counts/sec). A 90% $C.L$ upper limit is calculated when the value are defined with a poor statistics ($< 2\sigma$). An example is summarized in Table 5.5.2

sample	peak	counts	error	I_{rel}	time	counts/day	error
Pb	609.3 keV	57	17	0.461	12.92	3.10	0.67
Ge only	609.3 keV	93	29	0.461	21.28	3.01	0.52

Pb - Ge	error	Efficiency	mass	activity	error	Limit
counts/day		*%*	*kg*	$\mu Bq/kg$		*90% C.L.*
0.09	0.84	4.6	34	6.55	62.48	230 $\mu Bq/kg$

Table 5.2: Example of sample activity calculation for the case of a lead candidate (plombum) for EXO-200.

Five daughter nuclei of ^{238}U are used to calculate $Uranium - 238$ activity (Table 6.1), and seven for $Thorium - 232$. A mean of these peaks ($x_i \pm \sigma_i$) is calculated according to

$$\langle x \rangle = \frac{\sum_{i=1}^{n} \frac{1}{\sigma_i^2} x_i}{\sum_{i=1}^{n} \frac{1}{\sigma_i^2}}$$

$$\Delta\langle x \rangle = \sqrt{\frac{1}{\sum_{i=1}^{n} \frac{1}{\sigma_i^2}}}$$

$Cobalt - 60$ has also two gamma lines and a mean is calculated.
$Uranium - 238$ activity is estimated with its daughter nuclei. But this method is valid only if the sample has reached a secular equilibrium, which was the case for almost all samples. We used the 1001 keV peak from ^{234m}Pa and $186.2 keV$ from ^{226}Ra to check it, as these isotopes appear at the beginning of $Uranium - 238$ decay chain.

The first 24 hours of counting are deleted, that's what we call a "radon reset". Radon present in the detector — when opened for loading the sample — is flushed away in $\sim 5 - 6$ hours thank to the N_2 circulation (see section Radon shielding 4.7).

5.6 Cosmogenic activation of copper

Copper activation under cosmogenic exposure is important during not-shielded phases. It was the case in EXO when the copper cryostat was built and transported from France to Stanford. Although ground transportation was choosen, some activation ispotopes can be observed after exposing copper to cosmics, as shown in Table 5.3. Neutron activation of copper leads to unstable isotopes such as ^{54}Mn, ^{56}Co, ^{57}Co,

^{58}Co, ^{59}Fe and ^{60}Co. An example of neutron activation to ^{60}Co is shown on Figure 5.6, although these cross-sections are not well understood.

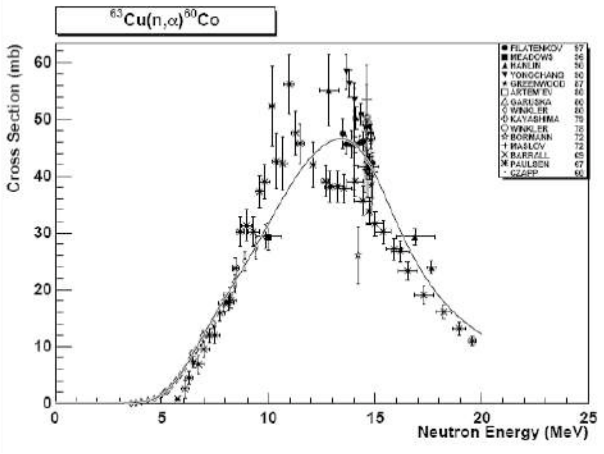

Figure 5.6: Neutron activation of ^{63}Cu (from IAEA-Tecdoc; Reference neutron activation library

A 3.35 kg low-activity copper brick (from the cryostat batch) was measured unexposed, i.e. directly after delivery. The brick was then exposed for 49 days under cosmics and measured for a new week in the germanium detector. This was repeated with 114 days and 149 days total exposure of this same brick.

Isotope	Unexposed Cu	Cosmogenics exposed Cu		
		49 days	114 days	149 days
	[mBq/kg]	[mBq/kg]		
^{60}Co	< 0.036	< 0.066	< 0.082	< 0.128
^{59}Fe	< 0.138	< 0.094	< 0.257	< 0.603
^{58}Co	< 0.167	< 0.236	0.33 ± 0.18	0.24 ± 0.12
^{57}Co	< 0.277	< 0.250	0.61 ± 0.28	0.50 ± 0.24
^{56}Co	< 0.050	< 0.85	< 0.372	< 0.142
^{54}Mn	< 0.104	< 0.131	< 0.257	< 0.155

Table 5.3: Cosmogenics exposed NOSV Copper

One can notice activation products of copper (^{58}Co and ^{57}Co) with values clearly above background. The exposure time of the cryostat was thus minimized, as well as the exposure of the copper plates for other EXO-200 elements.

5.7 Radon shielding

N_2 flushing the detector volume expel the air — charged with radon — out of the detector volume. This allow a measurement without any radon contamination. Radon expel was measured; the detector was opened for 10 minutes in order to fill it with air charged in radon. It was then closed and one measured (during 2 hours) the radon quantity with N_2 flux turned off. Nitrogen was then turned on and air expel began. The gamma spectrum was recorded every hour.

Figure 5.7 (left) shows the total number of counts of the gamma spectrum as a function of the counting time. One can see that the count rate is important for the first 4 hours and then it stabilizes on $25 - 30$ counts/hour, corresponding to the detector background.

The evolution with time of daughter nuclei from ^{222}Rn were measured. The gamma peaks are $295.2\ keV$, $351.9\ keV$, $609.3\ keV$, $1120.3\ keV$ and $1764.5\ keV$ from $Uranium-238$ decay chain. The initial radon activity corresponds to $5.84\ Bq$. With N_2 circulation, this activity decreases exponentially, while ^{226}Ra activity remains stable. As radon comes after ^{226}Ra in the decay chain, activity from ^{226}Ra represents the ^{238}U activity of the detector's background, while the other ^{238}U daughter nuclei can be used to determine the evolution of radon. It is thus expelled out from the germanium environment in $5-6$ hours after N_2 circulation, as one can see on Figures 5.7.

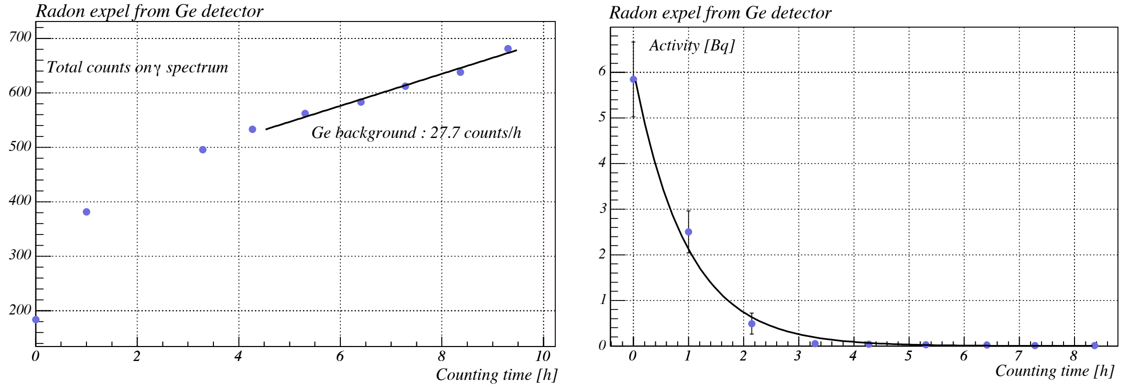

Figure 5.7: Total counts on γ-spectrum (left) and radon activity with N_2 circulation (right).

5.8 Activities in g/g :

Activities are often given in g/g or in ppm, ppb, ppt (10^{-6}, 10^{-9}, 10^{-12} g/g). The conversion is given by

$$a[g/g] = \frac{A}{N_{Av}} \frac{T_{1/2}}{log2}\, a[Bq/g]$$

where a is the activity in g/g or in Bq/g, A is the atomic number of the isotope, $T_{1/2}$ its half-life and N_{Av} is the Avogadro number.

Table 5.4 summarizes the conversion factors for the main isotopes used.

Isotope	Conversion factor
^{238}U	$1\ mBq/kg = 8.00\ 10^{-11}\ g/g$
^{232}Th	$1\ mBq/kg = 2.40\ 10^{-10}\ g/g$
^{226}Ra	$1\ mBq/kg = 2.73\ 10^{-17}\ g/g$
^{40}K	$1\ mBq/kg = 3.233\ 10^{-8}\ g/g$
^{137}Cs	$1\ mBq/kg = 3.106\ 10^{-18}\ g/g$
^{60}Co	$1\ mBq/kg = 2.404\ 10^{-20}\ g/g$

Table 5.4: conversions from mBq/kg to g/g

5.9 Results for EXO samples

A broad range of samples were analyzed for EXO, from the cryostat copper and the lead shielding, to the high voltage cables of the TPC. Table 5.6 summarizes the measured activities in terms of ^{238}U, ^{232}Th, ^{40}K, ^{60}Co and ^{137}Cs. The MD entry refers to Material Database on EXO website[2].

5.10 Discussion

Germanium gamma analysis is a powerful tool to investigate low radioactivity. This was essential for EXO-200 and allows to select or reject samples for the detector construction. Combined with other low counting techniques, we were able to calculate EXO-200 background, induced by the radioactivity of the used materials. The global background of EXO-200 has been calculated to be 20 $events/year$ around the $Q_{\beta\beta}$ value ($\pm 2\sigma$) of ^{136}Xe.

Moreover, Germanium gamma counting allow us to have informations on the possible activation of copper during "non-shielded" phases, such as machining and transportation. Activation isotopes were measured in a copper sample exposed to cosmics after $\sim$ 100 days.

And finally, gamma analysis can be also very interesting in some applications, such as meteorite analysis, as described in the next chapter.

---

[2] *http://grattalab3.stanford.edu/exo_elog/*

Sample	MD	^{238}U	^{232}Th	^{40}K	^{137}Cs	^{60}Co
		$[mBq/kg]$				
Superisolation; Teril IR 305, Jehier		49.07 ± 24.63	< 5.54	575.6 ± 233.7	< 12.66	< 12.03
NOSV copper; Nordeutsche Affinerie		< 0.40	< 0.07	< 2.15	< 0.03	< 0.14
Lead; JSC Industrial Corporation		58.25 ± 3.52	1.62 ± 0.86	7.27 ± 4.85	< 0.13	< 2.47
Lead VG2; Plombum		< 0.14	< 0.14	< 0.53	< 0.01	0.02
Washers bronze/ph; SOLON 8L80PB		13.26 ± 0.96	3.74 ± 0.48	< 4.71	< 0.16	< 0.38
Brazing Ag/Cu; CERN		< 303.6	720.5	< 8630.2	< 125.91	< 360.00
Helicoils; stainless steel		< 1.38	< 0.17	< 5.46	42.55 ± 1.42	< 0.56
Flat cable; Stanford		< 148.22	< 15.1	1270 ± 768	< 13.9	< 25.25
Thermocouples	MD87	< 7.44	< 20.11	153.2 ± 82.7	< 4.86	< 2.66
Aluminum for APD's; Pechinay	MD12	< 1.11	< 0.21	15.12 ± 8.18	< 0.13	0.36
Copper wire (cryostat heater)	MD71	< 0.21	< 0.04	< 2.43	< 0.09	< 0.08
Bolts bronze/Si; C65100	MD86	1.29 ± 0.73	< 0.53	< 14.72	< 0.17	< 0.35
Teflon; Saint-Gobain		3.18 ± 1.46	< 0.35	< 22.00	< 0.21	< 0.60
Seal viton		907.0 ± 15.02	133.6 ± 4.8	2427 ± 110	< 2.71	< 6.44
Espanex cable	MD1	< 1.19	< 0.85	$< 17.74 \pm 7.27$	< 0.17	< 1.38
LXe sensors	MD19	274.9 ± 51.5	372.2 ± 94.6	1054.1 ± 155.2	< 10.95	< 3.47
LXe sensors not encapsulated	MD19	1891.7 ± 296.4	1363.3 ± 382.1	3136.6 ± 488.0	< 20.44	< 16.56
Resistive paste 1108; DuPont PAG-092	MD18	141.55 ± 26.82	< 13.29	167.7 ± 62.1	< 3.25	< 4.37
Conductive paste 6160; DuPont PCP-135	MD18	$\pm$	$<$	$\pm$	$<$	$<$
Teflon 6472; DuPont		11.5 ± 2.4	< 1.2	11.1 ± 5.8	< 1.2	< 155.9
Resin 828; Hexonche	MD2	< 2.4	< 0.5	< 4.8	< 0.4	< 0.4
Velcro superinsulation; Jehier		6.8 ± 3.9	< 5.3	95.6 ± 42.0	< 3.1	< 1.1
Pb coating; Glasurit MS-Klarlack; Goslar	MD29	9.82 ± 0.93	< 0.55	22.39 ± 7.73	< 0.35	< 0.40
Pb cutting oil; Goslar		45.1 ± 7.2	< 2.5	2896 ± 177	< 9.1	< 1.4

Table 5.5: Samples measured for EXO

Sample	MD	^{238}U	^{232}Th	^{40}K	^{137}Cs	^{60}Co
				$[mBq/kg]$		
Etched Espanex	MD53	< 0.95	< 0.13	< 3.86	< 0.49	< 0.44
Espanex	MD52	< 0.45	< 0.84	< 3.52	< 1.00	< 0.50
Cu tubing 1/2”	MD66	< 1.10	< 2.57	< 4.25	< 22.62	< 0.37
Cryostat Uline Foam	MD62	393.30 ± 69.22	< 62.73	< 348.13	< 22.62	< 18.01
Inconel; Jetseal		< 35.69	< 4.62	< 280.08	< 11.53	< 3.04
Bronze/ph APD spiders	MD34	1.20	< 0.44	< 11.24	1.16 ± 0.72	< 0.20
Copper lot; SLAC	MD50	< 0.42	< 0.11	< 0.39	1.79 ± 0.35	< 0.05
Copper lot; SLAC	MD49	< 0.28	< 0.06	3.12 ± 1.94	2.47 ± 0.39	0.40 ± 0.11
Cu tubing 1”		< 1.56	< 0.14	12.60 ± 7.38	< 0.79	< 0.49
Bronze/ph 3/4-hard for cryostat door seal	MD48	< 1.64	< 0.25	< 8.77	4.37 ± 0.88	< 0.47
Bronze/ph 1/2-hard for cryostat door seal	MD47	< 1.32	< 0.26	< 7.68	< 1.28	< 0.30
Ancamide Resin 506		5.56 ± 1.60	< 0.35	< 23.92	< 1.12	< 0.37
Teflon tubing (cryostat heater)	MD72	< 28.41	< 2.27	< 155.16	< 8.45	< 4.51
HV cable candidate	MD65	427.10 ± 7.51	147.57 ± 3.27	595.05 ± 39.51	< 1.02	< 1.27

Table 5.6: Samples measured for EXO

5.11 Appendix

Figure 5.8 shows ^{238}U natural decay chain and the emitted photons we used for Germanium analysis. Arrows pointing to the left were used for α-decays and arrows pointing to the right for β-decays.

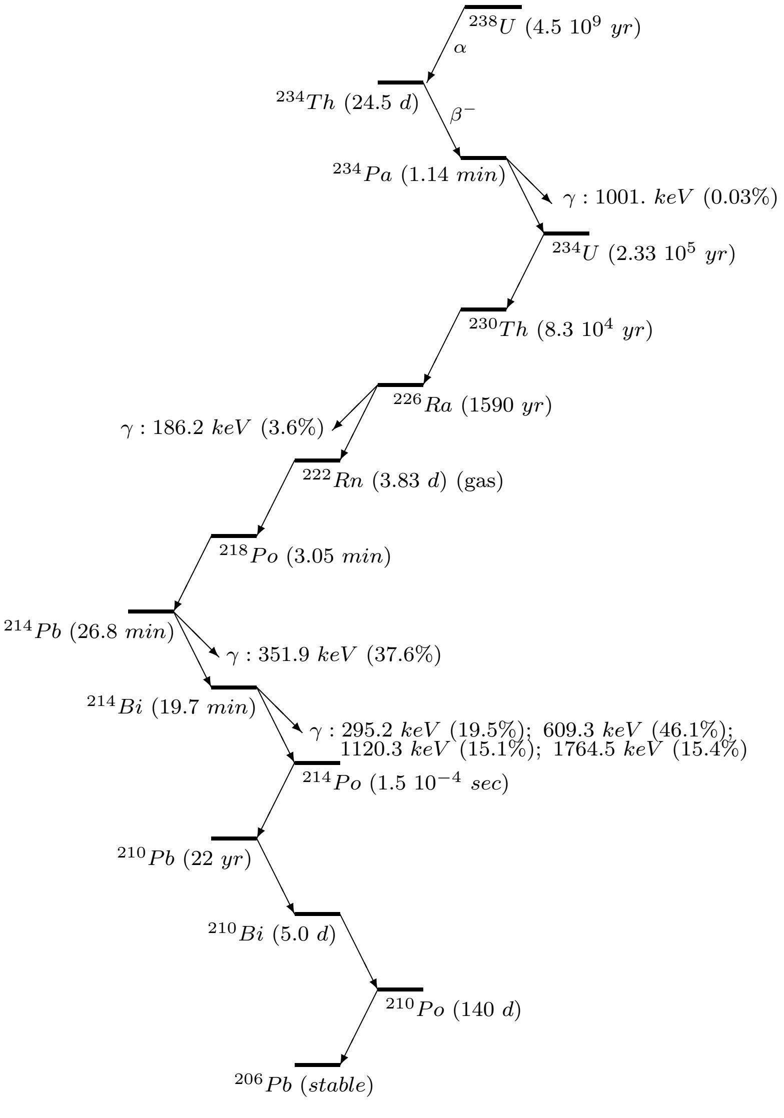

Figure 5.8: ^{238}U natural decay chain with the corresponding emitted photons.

Bibliography

[1] Final report on the search for neutrinoless double-β decay of ^{76}Ge from the Gotthard underground experiment; D.Reusser et al; Phys. Rev. D 45 (1992), 2548-2551.

[2] The "La Vue-des-Alpes" underground laboratory; Y.Gonin et al; Rev. Scientific Instruments 74 (2003), 4663-4666.

Chapter 6

Germanium gamma analysis of meteorites

Gamma spectroscopic analyses of meteorites were carried out in our low-background Germanium detector. This can be seen as an application of our germanium measurements. Gamma spectroscopic analysis of meteorites is complementary to "standard" analysis, such as mass spectrometry, and is able to measure a range of radioisotopes present in the meteorite. Germanium analysis of meteorites were achieved in various labs, providing only activity values for radionuclides present in large amounts, such as ^{40}K, which was slightly above germanium background [7]. Thank to its very low background characteristics, our germanium detector makes a powerful tool to probe various radionuclides with numerous details.

Meteorites are classified in three main classes : *stony meteorites*, including chondrites (85.7% of observed falls) and achondrites (7.1%), *stony-iron meteorites* (1.5%) and *iron meteorites* (5.7%). Various meteorites were measured in the germanium detector, most of them were chondrites ($H5$ and $L5$ type; H means a "high" concentration of Fe, while L means a "low" concentration), except one iron meteorite. Radioisotopical analysis of chondrites aims at various goals

- Efficient proof of extra-terrestrial nature of unknown samples.
- Terrestrial age determination (decay of cosmogenic radionuclides, increase of contamination with terrestrial radionuclides).
- Position indication of fragments from an original meteorite and radius of this original meteorite.

6.1 Isotopes of interest for meteorites

Various isotopes were measured and are summarized in Table 6.1. Daughter nuclei from the $Uranium - 238$ decay chain were measured and give a value for ^{238}U under the assumption of secular equilibrium. $Thorium - 232$ was also measured, as well as $Potassium - 40$, $Cobalt - 60$, $Ceasium - 137$, $Aluminum - 26$. Some short-lived isotope are interesting for the case of meteorites with very small terrestrial age

— i.e. El Hammami, Bassikounou and Noktat Addagmar —. These isotopes are $Sodium-22$, $Cobalt-57$, $Cobalt-58$, $Cobalt-59$, $Cobalt-60$, $Manganese-54$, etc.

Beside these direct lines, other peaks (indirect) can be observed on the gamma spectra :

- 511 keV peak due to e+/e- annihilation of β^+-emitters (^{26}Al, ^{22}Na, etc.)
- escape peaks : $E_\gamma - 511\ keV$: 951 keV for ^{40}K escape, 1298 keV for ^{26}Al
- pile-up peaks : 511 $keV + E_\gamma$ from β^+ emitters ^{22}Na and ^{26}Al

Isotope	Daughter nucleus	Energy [keV]	Rel. Intensity [%]
^{238}U	^{214}Bi	295.2	19.3
	^{214}Pb	351.9	37.6
	^{214}Bi	609.3	46.1
	^{214}Bi	1120.3	15.1
	^{214}Bi	1764.5	15.4
^{238}U	^{226}Ra	186.2	3.6
^{232}Th	^{212}Pb	238.6	100
	^{228}Ac	338.3	11.3
	^{208}Tl	583.2	28.1
	^{228}Ac	911.2	25.8
	^{228}Ac	968.9	15.8
	^{208}Tl	2614.5	38
^{40}K	—	1460.8	11.5
^{60}Co	—	1173.2	100
	—	1332.5	100
^{137}Cs	—	661.2	85.1
^{26}Al	—	1129	2.5
	—	1809	99.8
^{22}Na	—	1274	99.9

Table 6.1: Radioisotopes of interest for meteorites.

6.2 Production of radionuclides in meteorites

Radionuclides are produced in meteorites by cosmogenic activation of their elements. Solar cosmic rays (SCR) — mainly protons — from $E \simeq 1 - 200\ MeV/A$ produce a negligible amount of secondary particles in the meteorite, and only on its surface, while Galactic cosmic rays (GCR) — protons and heavy particles — can produce cosmogenic nuclides in a meteorite, due to the higher energies involved $E \simeq 0.1 - 10\ GeV/A$.

The production P_j of cosmogenic nuclide in a meteorite with radius R at a depth d by particles with energy E is given by

$$P_j(R,d,E) = \sum_{i=1}^{N} c_i \frac{N_A}{A_i} \sum_{k=1}^{3} \int_0^{\infty} \sigma_{j,i,k}(E) \cdot J_k(E,R,d)\ dE$$

where N_A is Avogadro number, A_i is the mass number of the target element i, c_i is the abundance of element i in $[g/g]$ and k is an index for the reaction particle type : primary protons, secondary protons and secondary neutrons. $\sigma_{j,i,k}(E)$ is the excitation function for the production of nuclide j from target element i, with reactions induced by particles of type k. Finally, J_k is the differential flux density of particles of type k and is given by

$$J_k = \int_0^{4\pi} \exp\Big[-\frac{d}{\lambda_k}\Big]\ d\Omega$$

d is the depth in the direction $d\Omega$ and λ_k is the mean free path.

Figure 6.1 shows the calculated Galactic cosmic rays production rates of ^{26}Al in ordinary chondrites with radii between 5 *cm* and 120 *cm*.

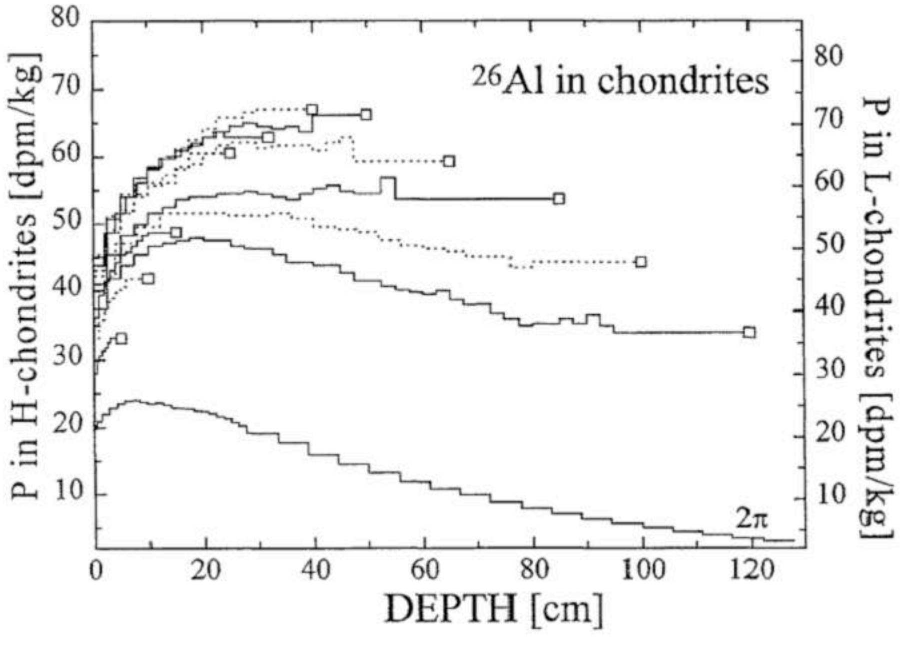

Figure 6.1: GCR production rates of ^{26}Al in ordinary chondrites with radii between 5 *cm* and 120 *cm* [8]. Each curve represent given meteorite radius.

6.3 Measured meteorites

Several meteorites were analysed, with different histories. El Hammami is a meteorite with very small terrestrial age, fallen on Earth in 1995. The analysed sample

is a fragment with reference BE-627. Bassikounou and Noktat Addagmar are meteorites with smaller assumed terrestrial ages, and they were measured only a few months after their assumed time of fall.
All other meteotires were collected during consecutive campains in the Oman desert by a Swiss-Omani meteorite search team [1], [2] [1]. JaH-090 (Jiddat al Harasis), JaH-091, 0503-134 and 0503-143 are paired fragments and were found in a large strewnfield of $\sim 50km$ length[3]. 0301-49 is a meteorite with large terrestrial age, as well as Dho-005 (Dhofar) and Shisr-017. A fragment from JaH-073 strewnfield, named 0201-68 was used to compare the values calculated with our method, and thus check our calibration. 0603-56 is a meteorite with low terrestrial age. All of them are chondrites (H5 for El Hammami and L5 for the other ones). Shisr-043 is an iron meteorite. And SaU-094 (Sayh al Uhaymir) is a martian meteorite. Finally a sample of the sand of the Oman desert — 0503-128B — was measured. Table 6.2 summarizes the different meteorites counted in our germanium detector. The gamma spectra of those chondrites are attached in the Appendix section.

Meteorite	Type	Mass [g]	ρ [g/cm^3]	Terrestrial age [kyr]	Comment
El Hammami	H5	1091.5	3.70	0.011	low terrestrial age
Bassikounou	L5	5.8	3.35	$3\ 10^{-4}$	fallen on October 12, 2006
Noktat Addagmar	L5	511.6	3.35	$6\ 10^{-4}$	fallen on June 30, 2006
0603-56	L5	55	3.35	1.0 ± 1.0	low terrestrial age
JaH-090	L5	1013	3.35	19.3 ± 1.3	large strewnfield
JaH-091	L5	714	3.35	19.3 ± 1.3	paired to JaH-090
0503-143	L5	147.4	3.35	19.3 ± 1.3	paired to JaH-090
0503-134	L5	625	3.35	19.3 ± 1.3	paired to JaH-090
0301-49	L5	506	3.35	38.2 ± 2.4	high terrestrial age
Dho-005	L5	370	3.35	> 47	high terrestrial age
Shisr-017	L5	1026	3.35	> 50	high terrestrial age
JaH-073	L5	205.3	3.35	18.0 ± 1.0	used for comparison
Shisr-043	iron	321.8	7.94	< 10.0	iron meteorite
0503-128B	—	420	—	—	sand from Oman desert
SaU-094	mars	163.5	3.206	12.0 ± 1.0	meteorite from Mars

Table 6.2: Meteorites measured in the Ge detector

6.4 Results

This section reports on the results from the spectrum analysis of the measured meteorites. The meteorites composition [6] implemented into the Monte-Carlo simulation was the following :

- H chondrites : Fe 29%, Si 18%, Mg 15%, O 38%.
- L chondrites : Fe 22%, Si 18%, Mg 15%, O 43%, S 2%.
- Iron meteorites : Fe 91.0%, Ni 8.07%, Co 0.50%.

---

[1] Dr Beda Hofmann, Curator, Earth Science Department, Natural History Museum, Bernastrasse 15, CH-3005 Bern

- Mars meteorite : O 44.68%, Si 22.45%, Fe 13.27%, Mg 12.97%, Ca 3.99%, Al 2.64%.

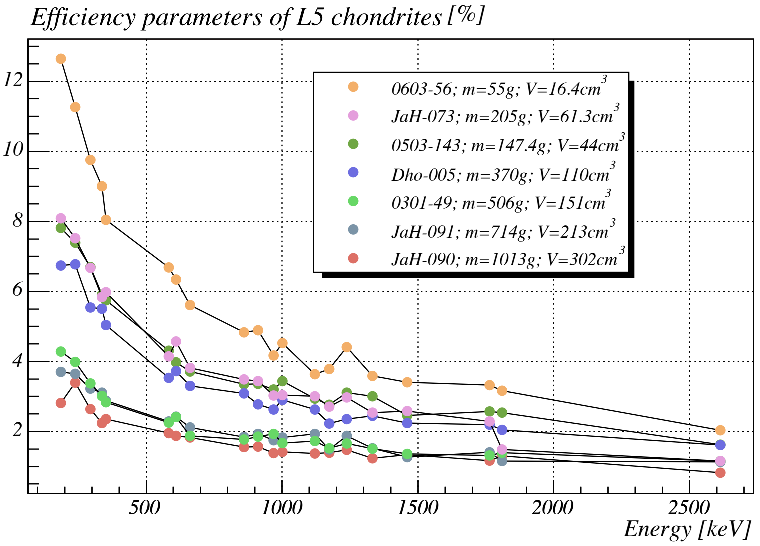

Figure 6.2: GEANT-3 simulation of efficiency parameters for analysed L5 chondrites.

Figure 6.2 shows the simulated efficiency parameters for seven analyzed L5 chondrites. One can notice the influence of chondrite dimensions (volume, mass) on the efficiency parameters. Simulated efficiency values are summarized in Table 6.12 in the Appendix section.

Table 6.3 shows the results of paired meteorite fragments, measured in our germanium detector and Table 6.4 meteorites with low or high terrestrial ages. Radioactivity values are given in mBq/kg. Radionuclides are usually given in dpm/kg in the literature. A conversion into dpm/kg (dpm : decay per minute) can be found in the Appendix section (Tables 6.13 to 6.15).

Isotope	JaH-090 $(19.3 \pm 1.3\ kyr)$ $[mBq/kg]$	JaH091 $(19.3 \pm 1.3\ kyr)$ $[mBq/kg]$	0503-143 $(19.3 \pm 1.3\ kyr)$ $[mBq/kg]$	0503-134 $(19.3 \pm 1.3\ kyr)$ $[mBq/kg]$
^{238}U	187.22 ± 5.55	186.90 ± 5.96	199.95 ± 9.57	159.00 ± 10.74
^{226}Ra	321.96 ± 112.47	244.23 ± 104.36	559.34 ± 134.56	458.34 ± 187.55
^{232}Th	101.24 ± 3.20	91.64 ± 3.41	77.16 ± 4.94	81.57 ± 6.19
^{40}K	25058 ± 176	27997 ± 233	25853 ± 349	22144 ± 425
^{137}Cs	7.49 ± 3.40	10.42 ± 3.42	< 11.45	< 7.02
^{60}Co	5.55 ± 2.18	< 4.70	< 8.73	< 12.11
^{26}Al	777.22 ± 10.69	962.37 ± 15.35	605.65 ± 17.96	581.85 ± 23.09
^{22}Na	< 4.94	< 4.81	< 6.11	< 10.06

Table 6.3: Results from paired meteorites, measured in the Ge detector. Upper limits are given with 90% $C.L.$

Isotope	El Hammami ($11\ yr$) [mBq/kg]	0301-49 ($38.2 \pm 2.4\ kyr$) [mBq/kg]	Dho-005 ($> 47\ kyr$) [mBq/kg]	JaH073 ($18.0 \pm 1.0\ kyr$) [mBq/kg]	Shisr-017 ($> 50\ kyr$) [mBq/kg]
^{238}U	122.38 ± 4.05	220.88 ± 7.78	310.46 ± 7.96	302.98 ± 10.44	418.61 ± 5.73
^{226}Ra	190.77 ± 70.46	628.09 ± 116.27	990.47 ± 106.81	518.93 ± 137.32	1233.0 ± 80.5
^{232}Th	62.89 ± 2.35	100.59 ± 4.36	115.28 ± 3.84	85.63 ± 5.12	88.24 ± 2.59
^{40}K	22902 ± 142	30559 ± 301	22931 ± 239	25684 ± 347	21061 ± 159
^{137}Cs	< 4.15	21.26 ± 5.31	19.14 ± 4.21	< 11.74	19.36 ± 2.77
^{60}Co	13.89 ± 1.74	< 9.16	< 5.96	< 7.51	< 5.19
^{26}Al	733.86 ± 9.10	546.33 ± 13.63	540.48 ± 13.07	791.42 ± 27.56	567.62 ± 8.85
^{22}Na	214.89 ± 5.58	< 5.75	< 10.67	< 16.01	< 4.64

Table 6.4: Results from meteorites with low/high terrestrial ages, measured in the Ge detector. Upper limits are given with 90% $C.L.$

Isotope	0603-56 ($1.0 \pm 1.0\ kyr$) [mBq/kg]	Sand from Oman [mBq/kg]	SaU-094 ($12.0 \pm 1.0\ kyr$) [mBq/kg]	Bassikounou ($3\ months$) [mBq/kg]	Noktat Addagmar ($6\ months$) [mBq/kg]
^{238}U	486.69 ± 29.50	11073 ± 37.05	506.55 ± 11.41	148.98 ± 24.93	227.47 ± 5.05
^{226}Ra	714.14 ± 288.96	24088 ± 384	1586.8 ± 125.2	< 249.94	711.04 ± 65.24
^{232}Th	99.74 ± 12.31	5541.81 ± 21.10	44.68 ± 3.48	< 26.3	93.14 ± 2.63
^{40}K	27712 ± 881	176836 ± 593	5001.1 ± 153.6	23614 ± 597	22168 ± 176
^{137}Cs	106.7 ± 20.07	540.89 ± 15.35	49.58 ± 5.55	< 15.28	4.75 ± 2.20
^{60}Co	18.87 ± 9.70	10.84 ± 7.04	< 3.54	46.59 ± 10.49	1.92 ± 1.74
^{26}Al	709.37 ± 4.96	—	423.56 ± 14.70	524.93 ± 35.03	511.44 ± 8.90
^{22}Na	26.81 ± 11.90	—	< 5.22	593.45 ± 33.64	< 3.21

Table 6.5: Other meteorites. Upper limits are given with 90% $C.L.$

6.4.1 Quantitative analysis with JaH-073

A fragment of JaH-073 strewnfield, named 0201-68, was measured by Kees Welten[2] with mass spectrometry (AMS). We measured this same sample with the germanium detector, in order to check the values calculated with our method by comparing ^{26}Al activities.

Measurement type	^{26}Al activity [dpm/kg]
AMS, Berkeley	50.3 ± 1.6
Germanium, Neuchâtel	47.35 ± 1.65

Table 6.6: AMS and Germanium comparison for JaH-073 fragment.

We can observe a very good correlation of both measurements (Table 6.6). Our germanium measurements give thus precise quantitative values.

6.4.2 El Hammami : low terrestrial age meteorite

Table 6.10 summarizes some interesting radioisotopes for El Hammami BE-627 sample. The current radioactivity and the calculated activity at the time of fall are given. Table 6.8 shows the values in dpm/kg.

---

[2] University of California, Berkeley

Isotope	Actual activity $[mBq/kg]$	Activity at the time of fall $[mBq/kg]$
^{26}Al	733.86 ± 9.10	733.86 ± 9.10
^{22}Na	214.89 ± 5.58	1388.95 ± 36.10
^{60}Co	13.89 ± 1.74	34.88 ± 4.37

Table 6.7: Measured activities and calculated values at the time of fall for El Hammami $[mBq/kg]$.

Isotope	Actual activity $[dpm/kg]$	Activity at the time of fall $[dpm/kg]$
^{26}Al	44.03 ± 0.55	44.03 ± 0.55
^{22}Na	12.89 ± 0.33	83.34 ± 2.17
^{60}Co	0.83 ± 0.10	2.09 ± 0.26

Table 6.8: Measured activities and calculated values at the time of fall for El Hammami $[dpm/kg]$.

In the case of low terrestrial age meteorites, some parameters, such as the averaged cosmic-ray produced $^{22}Na/^{26}Al$ take typical values, between 1.0 and 1.8 for both H and L chondrites [9]

We would like to check this in the case of El Hammami meteorite; for our fragment BE-627 (H chondrite), we calculate a ratio $^{22}Na/^{26}Al \cong 1.89$. Ratios higher than expected values can be due to several reasons

1. Short exposure age or fragmentation shortly before the fall ($< 2Myr$) such that ^{26}Al has not reached secular equilibrium
2. Cosmic-ray gradient within the heliosphere

To the contrary, low $^{22}Na/^{26}Al$ ratios can be explained by solar production of ^{26}Al through the reactions

$$^{26}Mg\ (p,n)\ ^{26}Al$$

$$^{25}Mg\ (p,\gamma)\ ^{26}Al$$

$Cobalt-60$ is mainly produced through thermal neutron capture on $Cobalt-59$ and, since thermalization of secondary neutrons is strongly mass dependent, $Cobalt-60$ is a good depth indicator. Depth means here the position of a fragment in the inititial meteorite. As ^{60}Co is a short-lived radioisotopes with $T_{1/2} = 5.27\ yr$, the secular equilibrium is reached in meteorites and assuming a uniform and isotropic cosmic flux, the initial ^{60}Co concentration is identical for every meteorite with the same Co concentration. Theoretical predictions and experimental profiles of ^{60}Co activity have been published [4]. It is shown in Figure 6.3.

According to these results, ^{60}Co concentration of El Hammami sample BE-627 gives us an indication of its position in the initial meteorite. In the case of BE-627, we have an activity of $2.09 \pm 0.26\ dpm/kg$, which corresponds to a surficial position of this sample.

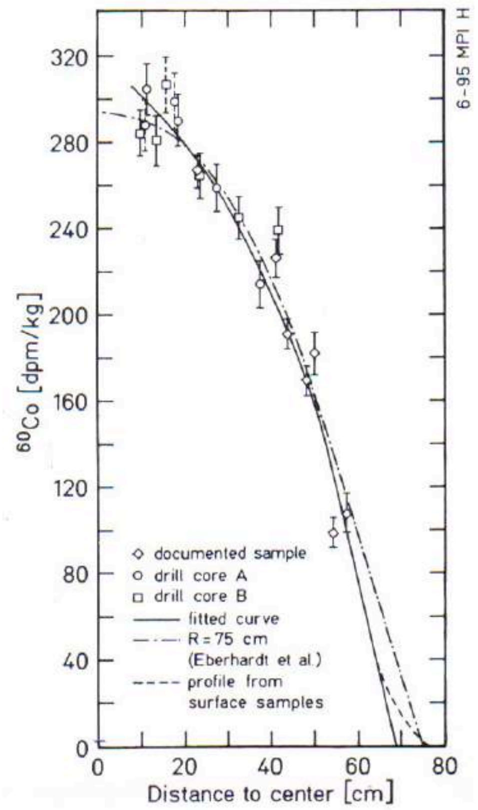

Figure 6.3: ^{60}Co activity as a function of the distance to the chondrite center [4].

6.4.3 High terrestrial age meteorites

Terrestrial age determination is traditionally done thank to ^{14}C measurements. However, this method is valid for meteorites with terrestrial ages smaller than 50 kyr, due to ^{14}C half-life ($T_{1/2} = 5730\ yr$). As an alternative to ^{14}C, the accumulation of terrestrial elements, including radioisotopes, may be used as a measure for the terrestrial age [10], [11], [12]. ^{238}U and ^{232}Th are present in the meteorites before the fall, but these concentrations increase with the time meteorites have spent in soils on Earth, due to chemical absorption. An estimate of the terrestrial age could then be possible with Uranium and Thorium (or daughters) concentrations present in the measured meteorites. Figures 6.4, 6.5 and 6.6 show a first indication of a correlation between ^{238}U — ^{232}Th concentrations versus meteorites terrestrial ages.

We can observe an increase in ^{238}U daughters and $Thorium - 232$ related to the terrestrial age of meteorites. One measured meteorite was excluded on these plots : 0603-56, which has different values. The higher values for ^{238}U daughters in this meteorite may be related to the rapid uptake of Ra (both uranogenic and thorogenic isotopes) during initial weathering.

Shisr-017 is a typical meteorite fragment interesting to estimate its terrestrial age. $Carbon - 14$ gives a value $> 50\ kyr$. According to our plots (Figures 6.4 to 6.6), the $Uranium - 238$ and $Thorium - 232$ content of Shisr-017 gives us the

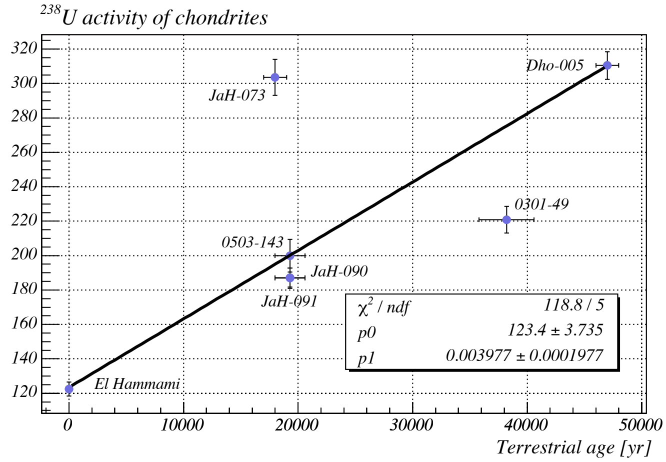

Figure 6.4: ^{238}U activity (daughter nuclei) in mBq/kg of various measured chondrites.

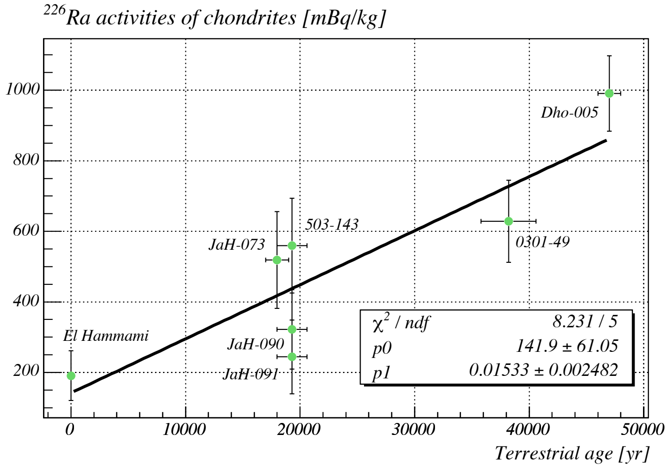

Figure 6.5: ^{226}Ra activity (^{238}U) of measured chondrites.

following terrestrial ages :

$$^{238}U : 74229 \pm 4071\ yr$$

$$^{226}Ra : 71177 \pm 13274\ yr$$

$$^{232}Th : 19991 \pm 3352\ yr$$

$Uranium - 238$ daughter nuclei and $Radium - 226$ lead to comparable results. $Radium - 226$ statistics is not as well defined as $Uranium - 238$, because the low energy line of $radium - 226$ (186.2 keV has more background.

However, the $Thorium - 232$ activity leads to a very different terrestrial age. This age does not fit with the $Carbon - 14$ value, so that one might think that $Thorium - 232$ (and its daughters) is not suited to estimate terrestrial ages. A possible reason for it would be that $Thorium - 232$ only exists in the insoluble tetravalent form that cannot be absorbed by iron oxides of the meteorite. To the contrary, $Uranium - 238$

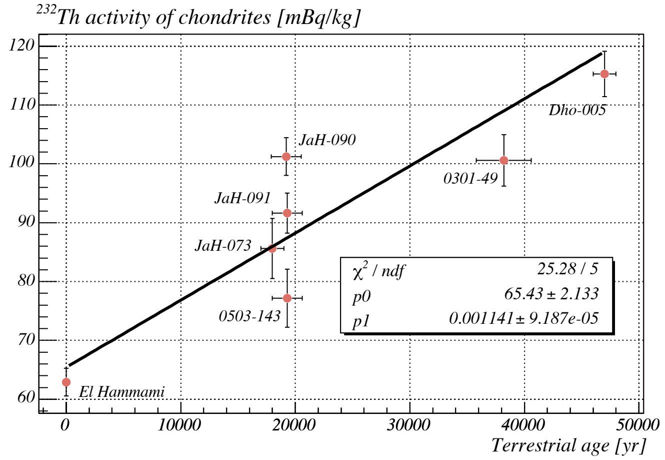

Figure 6.6: ${}^{232}Th$ activity of measured chondrites.

also exists, under oxidizing conditions, ion the hexavalent form (uranyl ion), which is easily soluble in water and therefore very mobile. Also, assuming accumulation of intermediate daughter elements such as relatively mobile radium, ${}^{226}Ra$ from $Uranium-238$ decay has a much longer half-life (1600 years) than the thorogenic radium isotopes ${}^{228}Ra$ (5.8 yr) and ${}^{224}Ra$ (3.6 days), leading to an equilibrium concentration of ${}^{226}Ra$ after several 1000 years while unsupported ${}^{232}Th$ daughters have no chance to accumulate to significant levels. Therefore, ${}^{232}Th$ daughters likely reflect true, while ${}^{238}U$ daughters do not.

6.4.4 Paired meteorites

Large meteorites often crumble when entering the Earth atmosphere. Fragments are found in large strewnfields, distributed in regions with elliptic shapes, as shown on Figure 6.7. A noble gases analysis is performed on fragments to bring a definitive evidence of pairing.

Paired fragments were measured in the germanium detector : JaH-090, JaH-091, 0503-143 and 0503-134. These samples show similar concentrations of ${}^{238}U$ and ${}^{232}Th$, which is logical as terrestrial ages of the different fragments are identical.
We have seen that $Cobalt-60$ is a good indicator of fragments position in the original meteorite. However, this isotope is only useful for meteorites with low terrestrial ages, as ${}^{60}Co$ has $T_{1/2} = 5.27\ yr$. For meteorites with larger terrestrial ages, we can use ${}^{26}Al$ ($T_{1/2} = 7.2\ 10^5\ yr$) in a similar way. $Aluminum-26$ is an isotope formed only with neutron activation on meteorites due to cosmic irradiation (Extra-galactic protons, mainly). This isotope is negligible on earth and gives us a clear signature of an extraterrestrial material. Moreover, ${}^{26}Al$ concentration varies with meteorite depth [8]. Figure 6.8 shows ${}^{26}Al$ profile as a function of the depth of the meteorite, i.e the position of the fragment from the meteorite surface. Table 6.9 represents ${}^{26}Al$ concentrations for the measured paired fragments. According to Figure 6.8, an estimation of the depth in the original meteorite can be given.

One can see that JaH-091 is a fragment that come from near the meteorite rim ($\sim 20\ cm$), JaH-090 is a little bit more deeper, as well as 0503-143, which is even

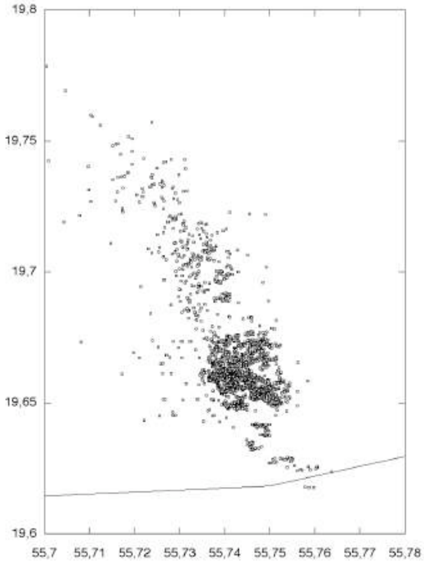

Figure 6.7: JaH-073 strewnfield ($\sim 8 \times 22\ km^2$) in the Oman desert. x and y axis represent longitude and latitude coordinates.

Meteorite	Actual activity	Activity at the time of fall		Depth
	$[mBq/kg]$	$[mBq/kg]$	$[dpm/kg]$	[cm]
JaH-091	962.37 ± 15.35	980.42 ± 15.64	58.82 ± 0.94	~ 20
JaH-090	777.22 ± 10.69	791.80 ± 10.89	47.51 ± 0.65	~ 32
0503-143	605.65 ± 17.96	617.01 ± 18.30	37.02 ± 1.10	~ 75
0503-134	581.85 ± 23.09	592.76 ± 23.52	35.56 ± 1.41	~ 120

Table 6.9: Measured ^{26}Al activities and calculated values at the time of fall for chondrites paired to JaH-090.

deeper. Finally, 0503-134 fragment comes from near the meteorite center. One can notice also that these measurements allow to give an approximative value of the original meteorite radius : JaH-090 paired fragments come from a meteorite that has :

$$Radius \simeq 120\ cm$$

Figure 6.8 shows the activity of various paired fragments measured in the germanium, as a function of depth in the original meteorite.

6.4.5 Meteorite from Mars

The evidence for a martian origin of SaU-094 is brought by mineral chemistry and oxygen isotopes [13]Moreover, the $^{40}K/^{232}Th$ ratio based on the gammaspectroscopy results of 15400 is in the range of Mars meteorites, e.g, the paired SaU-005 [14].

The high concentration of ^{238}U in SaU-094 indicates a significant uptake of uranium by this Martian meteorite in the desert environment, even though the concentration of reactive iron, and thus, iron hydroxides, is lower than in chondrites.

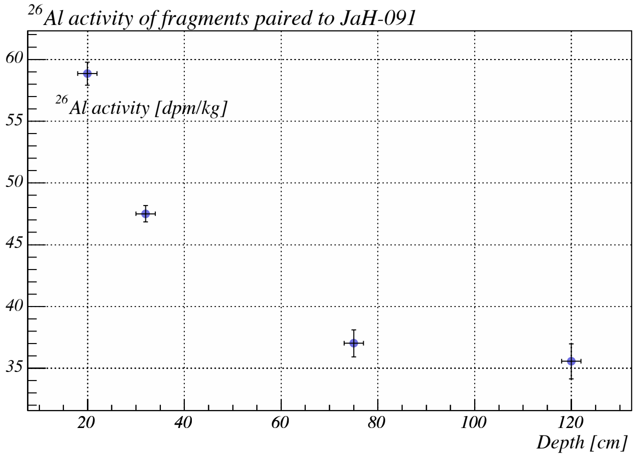

Figure 6.8: ^{26}Al activity of fragments paired to JaH-091.

Concentrations of ^{232}Th and ^{40}K should not be significantly affected, however.

6.4.6 Recently fallen meteorites

Two meteorites were measured only a few months after their assumed time of fall : Bassikounou, fallen on October 12, 2006, and Noktat Addagmar, fallen on June 30, 2006. The interest of measuring meteorites with very low terrerstrial ages lies in the fact that short-lived radioisotopes are still present and measurable. Table 6.10 summarizes the various short-lived isotopes that one may find in such meteorites.

Isotope	Energy $[keV]$	$T_{1/2}$ $[days]$	I_{rel} $[\%]$
^{52}Mn	1434.3	5.6	100
	744.2	5.6	90
	935.5	5.6	94.5
^{48}V	983.5	16.0	100
^{51}Cr	320.1	27.7	100
^{7}Be	477.6	53.3	10.5
^{58}Co	810.8	70.8	99
^{56}Co	846.8	78.8	100
^{46}Sc	889.3	83.9	100
^{57}Co	122.1	271.4	85.6
	136.5	271.4	10.7
^{54}Mn	834.8	312.2	99.98

Table 6.10: Short-lived radioisotopes present in meteorites with very low terrestrial ages [5].

Bassikounou

The Bassikounou meteorite fell on Earth on October 12, 2006 in Mauretania, 60 km from the Mali border. Although the sample we measured has only $5.8g$, a relatively long measurement time (24 days) gives us a good statistics. A lot of short-lived radioisotopes can be observed in the spectrum, confirming the recent fall of this meteorite. Their current activities (measured during January, 2007) are reported in Table 6.23, as well as the activities calculated for the time of fall, representing actually the saturation values for each of the given radioisotopes.

Isotope	Current activity		Activity at the time of fall	
	$[mBq/kg]$	$[dpm/kg]$	$[mBq/kg]$	$[dpm/kg]$
^{52}Mn	< 9.77	< 0.59	—	—
^{48}V	24.42 ± 10.62	1.47 ± 0.64	1205.2 ± 524.1	72.31 ± 31.45
^{51}Cr	25.15 ± 11.86	1.51 ± 0.71	239.15 ± 112.77	14.35 ± 6.77
^{7}Be	329.43 ± 122.93	19.77 ± 7.38	1061.87 ± 396.15	63.71 ± 23.77
^{58}Co	103.84 ± 15.61	6.23 ± 0.94	250.63 ± 37.67	15.04 ± 2.26
^{56}Co	49.02 ± 12.32	2.94 ± 0.74	108.20 ± 27.19	6.49 ± 1.63
^{46}Sc	55.28 ± 13.79	3.32 ± 0.83	116.28 ± 29.00	6.98 ± 1.74
^{57}Co	124.98 ± 10.96	7.50 ± 0.66	157.28 ± 13.79	9.44 ± 0.83
^{54}Mn	1509.69 ± 42.79	90.58 ± 2.57	1843.61 ± 52.25	110.62 ± 3.13
^{22}Na	593.45 ± 33.64	35.61 ± 2.02	633.74 ± 35.92	38.02 ± 2.16

Table 6.11: Short-lived radioisotopes measured in the Bassikounou meteorite.

Noktat Addagmar

Noktat Addagmar was supposed to fall on Earth on June 30, 2006 in the border area between the Western Sahara and Mauretania. A $591g$ fragment was measured in the germanium detector at the end of January, 2007. However, the absence of any of the short-lived radioisotope described in Table 6.23 shows that Noktat Addagmar is not a recent fall.

6.5 Discussion

Although only a few meteorites were measured up to now, interesting results can be carried out from these first measurements. One first checked the calibration of our calculation by comparing our results for JaH-073 with an AMS measurement made on the same meteorite fragment.

The new idea of determining (or at least estimating) the terrestrial age of meteorites with ^{238}U and ^{232}Th seems promising and useful when ^{14}C is unefficient or impossible, which is the case for meteorites with high terrestrial ages (> 50 kyr).

The position of a fragment in the original meteorite thank to radionuclides formed by cosmogenic activation — such as ^{26}Al — can be determined, as well as an estimation of the original meteorite radius, which present a real interest.

Finally, the measurement of short-lived radioisotopes can bring the proof of a recently fallen meteorite.

6.6 Appendix

Energy	Efficiency parameter from simulation [%]						
[keV]	JaH-090	JaH-091	0503-143	Dho-005	0301-49	0603-56	JaH-073
186	2.79	3.70	4.26	6.73	4.27	12.62	8.07
239	3.39	3.64	4.27	6.77	3.99	11.27	7.52
295	2.64	3.22	3.52	5.54	3.37	9.76	6.67
338	2.24	3.11	3.21	5.51	3.02	9.00	5.84
352	2.36	2.88	3.03	5.04	2.83	8.04	5.98
583	1.95	2.29	2.40	3.53	2.25	6.68	4.15
609	1.88	2.42	2.52	3.72	2.41	6.34	4.57
661	1.83	2.12	2.44	3.30	1.87	5.61	3.82
860	1.56	1.84	1.78	3.08	1.77	4.83	3.48
911	1.57	1.93	1.98	2.78	1.85	4.89	3.44
969	1.38	1.75	2.01	2.63	1.93	4.17	3.03
1001	1.42	1.83	1.95	2.90	1.67	4.53	3.04
1120	1.37	1.93	1.73	2.63	1.73	3.63	3.00
1238	1.47	1.88	1.78	2.36	1.66	4.41	2.97
1173	1.39	1.49	1.76	2.23	1.52	3.78	2.71
1332	1.23	1.52	1.52	2.45	1.51	3.59	2.54
1460	1.34	1.27	1.65	2.24	1.36	3.41	2.58
1764	1.17	1.41	1.40	2.19	1.32	3.33	2.29
1809	1.30	1.15	1.31	2.05	1.40	3.17	1.49
2614	0.82	1.13	1.07	1.61	1.16	2.04	1.15
Mass [g]	1013	714	147.4	370	506	55	205.3
$\rho[g/cm^3]$	3.35	3.35	3.35	3.35	3.35	3.35	3.35
O	43%	43%	43%	43%	43%	43%	43%
Mg	15%	15%	15%	15%	15%	15%	15%
Si	18%	18%	18%	18%	18%	18%	18%
Fe	22%	22%	22%	22%	22%	22%	22%
S	2%	2%	2%	2%	2%	2%	2%
Count. time [s]	530984	508593	519209	428816	433258	170353	356386

Table 6.12: Efficiency parameters simulated with GEANT 3 for measured meteorites.

Radionuclide activities are usually given in dpm/kg (decay per minute $/kg$) in the litterature. Tables 6.13, 6.14 and 6.15 is a transcription in dpm/kg of Tables 6.3, 6.4 and 6.5, respectively.

Isotope	JaH-090 (19.3 ± 1.3 kyr) [dpm/kg]	JaH091 (19.3 ± 1.3 kyr) [dpm/kg]	0503-143 (19.3 ± 1.3 kyr) [dpm/kg]	0503-134 (19.3 ± 1.3 kyr) [dpm/kg]
^{238}U	11.23 ± 0.33	11.21 ± 0.36	12.00 ± 0.57	9.54 ± 0.64
^{226}Ra	19.32 ± 6.75	14.65 ± 6.26	33.56 ± 8.07	27.50 ± 11.25
^{232}Th	6.07 ± 0.19	5.50 ± 0.20	4.63 ± 0.30	4.89 ± 0.37
^{40}K	1503.51 ± 10.56	1679.82 ± 13.98	1551.17 ± 20.95	1328.65 ± 25.51
^{137}Cs	0.45 ± 0.20	0.63 ± 0.21	< 0.69	< 0.42
^{60}Co	0.33 ± 0.13	< 0.28	< 0.52	< 0.73
^{26}Al	46.63 ± 0.64	57.74 ± 0.92	36.34 ± 1.08	34.91 ± 1.39
^{22}Na	< 0.30	< 0.29	< 0.37	< 0.60

Table 6.13: Results from paired meteorites.

Isotope	El Hammami (11 yr) [dpm/kg]	0301-49 (38.2 ± 2.4 kyr) [dpm/kg]	Dho-005 (> 47.0 kyr) [dpm/kg]	JaH073 18.0 ± 1.0 kyr [dpm/kg]	Shisr-017 > 50 kyr [$dpm|kg$]
^{238}U	7.34 ± 0.24	13.25 ± 0.47	18.63 ± 0.48	18.18 ± 0.63	25.12 ± 0.34
^{226}Ra	11.45 ± 4.23	37.69 ± 6.98	59.43 ± 6.91	31.14 ± 8.24	73.98 ± 4.83
^{232}Th	3.77 ± 0.14	6.04 ± 0.26	6.92 ± 0.23	5.14 ± 0.31	5.29 ± 0.16
^{40}K	1374.10 ± 8.52	1833.55 ± 18.07	1375.86 ± 14.37	1541.04 ± 20.79	1263.7 ± 9.6
^{137}Cs	< 0.25	1.28 ± 0.32	1.15 ± 0.25	< 0.70	1.16 ± 0.17
^{60}Co	0.83 ± 0.10	< 0.55	< 0.36	< 0.45	0.19 ± 0.09
^{26}Al	44.03 ± 0.55	32.78 ± 0.82	32.43 ± 0.78	47.49 ± 1.65	34.06 ± 0.53
^{22}Na	12.89 ± 0.33	< 0.34	< 0.64	< 0.96	< 0.21

Table 6.14: Results from meteorites with low/high terrestrial ages.

Isotope	0603-56 (1.0 ± 1.0 kyr) [dpm/kg]	Sand from Oman [dpm/kg]	SaU-094 (12.0 ± 1.0 kyr) [dpm/kg]	Bassikounou (3 $months$) [dpm/kg]	Noktat Addagmar (6 $months$) [dpm/kg]
^{238}U	29.20 ± 1.77	664.36 ± 2.22	30.39 ± 0.68	8.94 ± 1.50	13.65 ± 0.30
^{226}Ra	42.85 ± 17.34	1445.31 ± 23.03	95.21 ± 7.51	< 47.37	42.66 ± 3.91
^{232}Th	5.98 ± 0.74	332.51 ± 1.27	2.68 ± 0.21	< 1.24	5.59 ± 0.16
^{40}K	1662.76 ± 52.87	10610 ± 35.56	300.07 ± 9.22	1416.8 ± 35.9	1330.1 ± 10.6
^{137}Cs	6.40 ± 1.20	32.45 ± 0.92	2.97 ± 0.33	< 2.59	0.29 ± 0.13
^{60}Co	1.13 ± 0.58	0.65 ± 0.42	< 0.13	2.80 ± 0.63	< 0.21
^{26}Al	42.56 ± 3.00	—	25.41 ± 0.88	31.50 ± 2.10	30.69 ± 0.53
^{22}Na	1.61 ± 0.71	—	< 0.20	35.61 ± 2.02	< 0.22

Table 6.15: Other chondrites. Upper limits are given with 90% $C.L.$

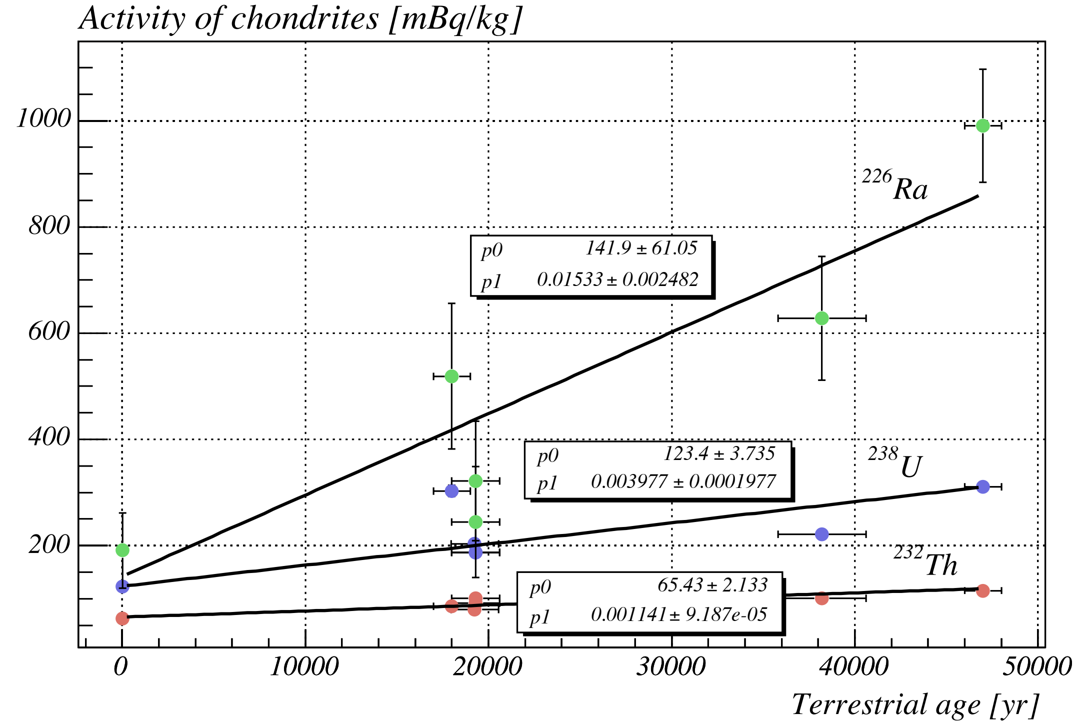

Figure 6.9: ^{238}U, ^{226}Ra and ^{232}Th activities in chondrites, as a function of terrestrial age.

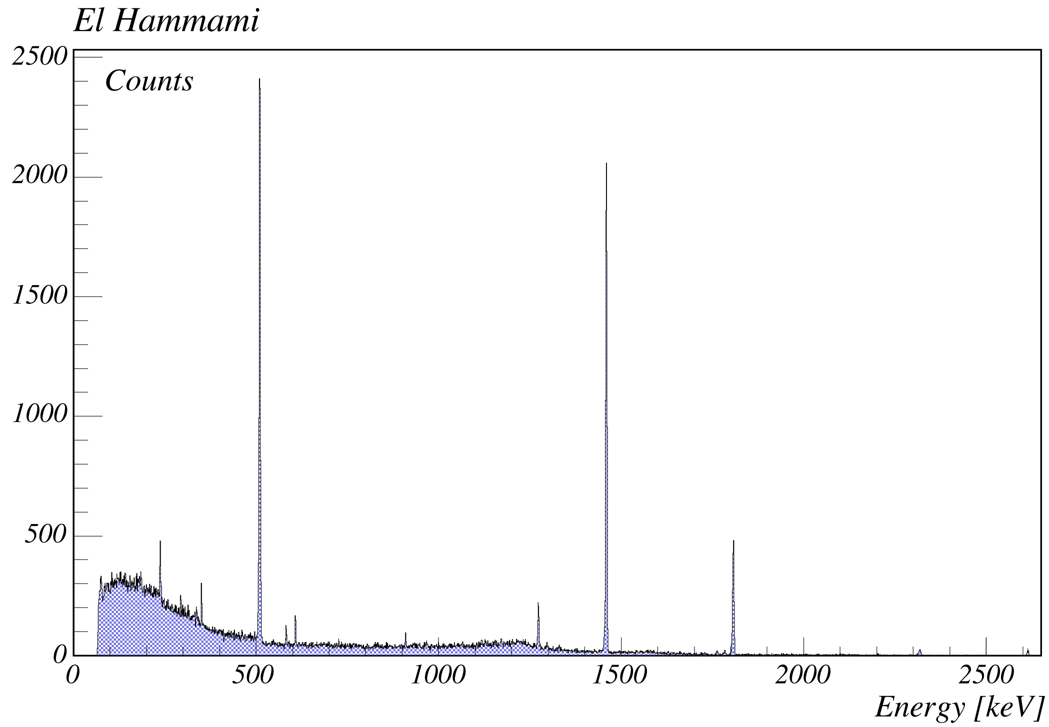

Figure 6.10: El Hammami gamma spectrum. Fragment BE-627.

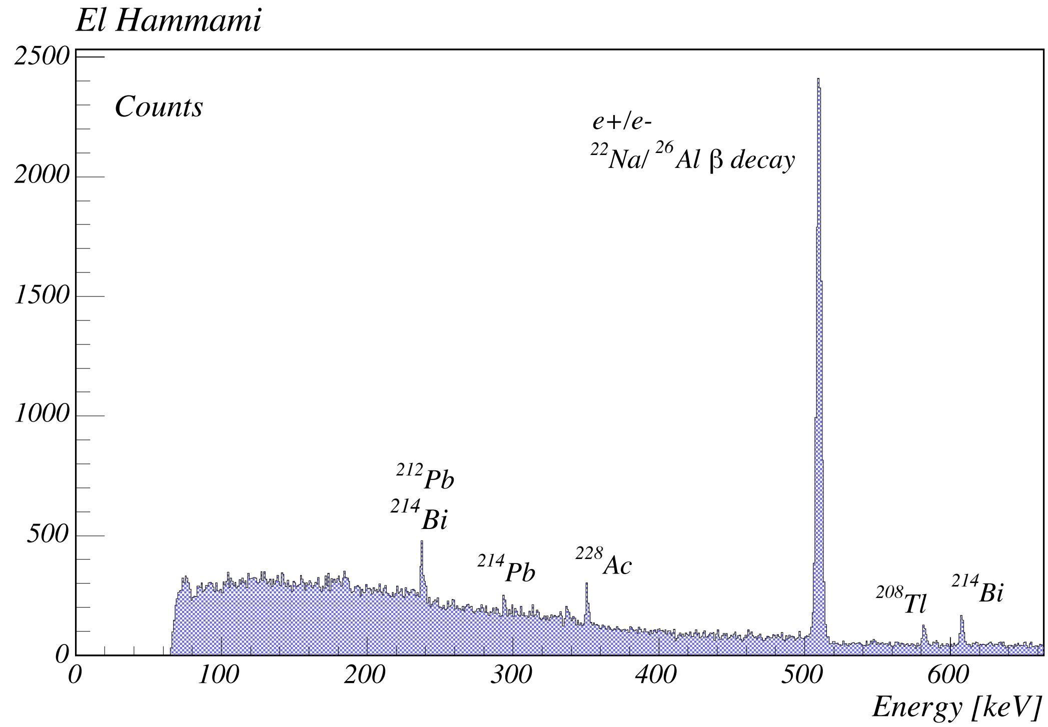

Figure 6.11: El Hammami spectrum detail : $0 - 664\ keV$.

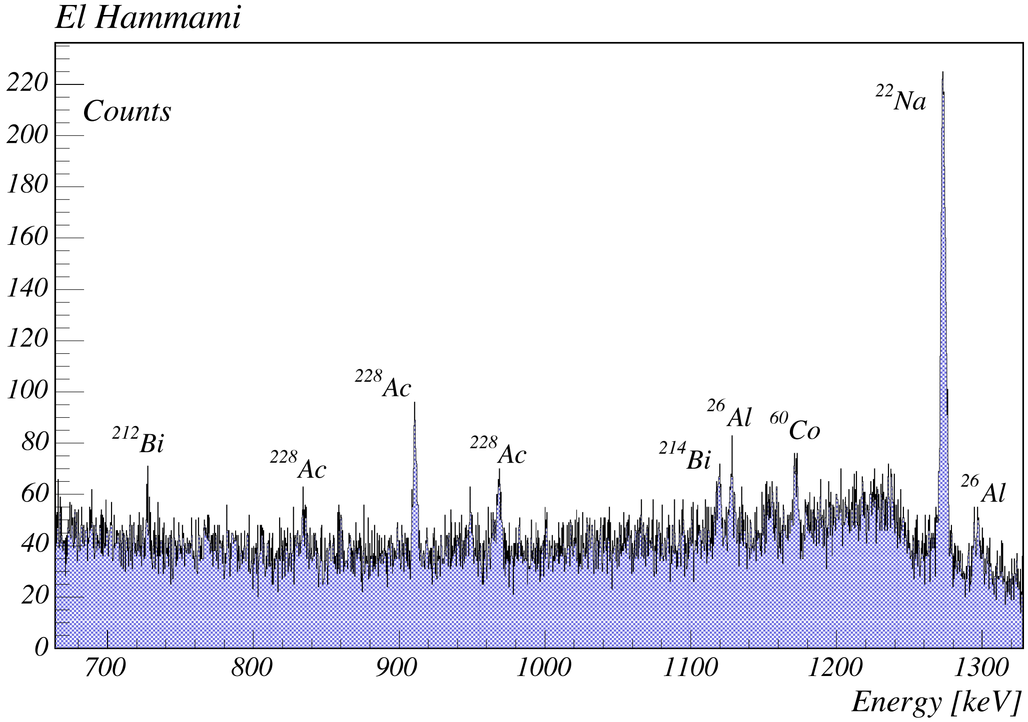

Figure 6.12: El Hammami spectrum detail : $664 - 1328\ keV$.

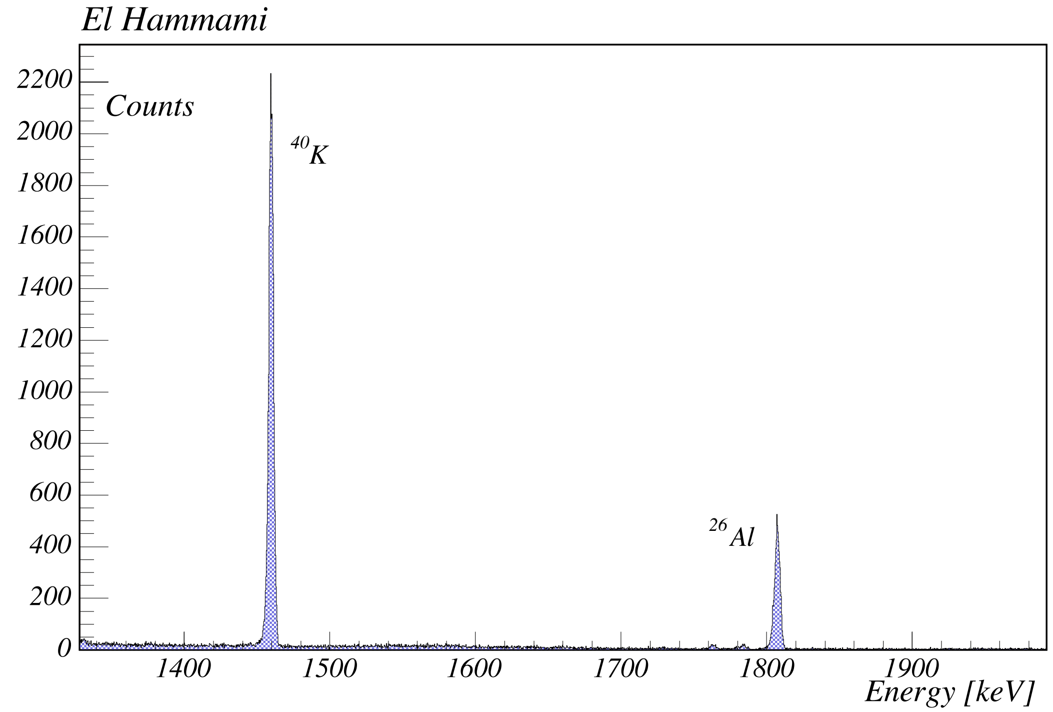

Figure 6.13: El Hammami spectrum detail : $1328 - 1992\ keV$.

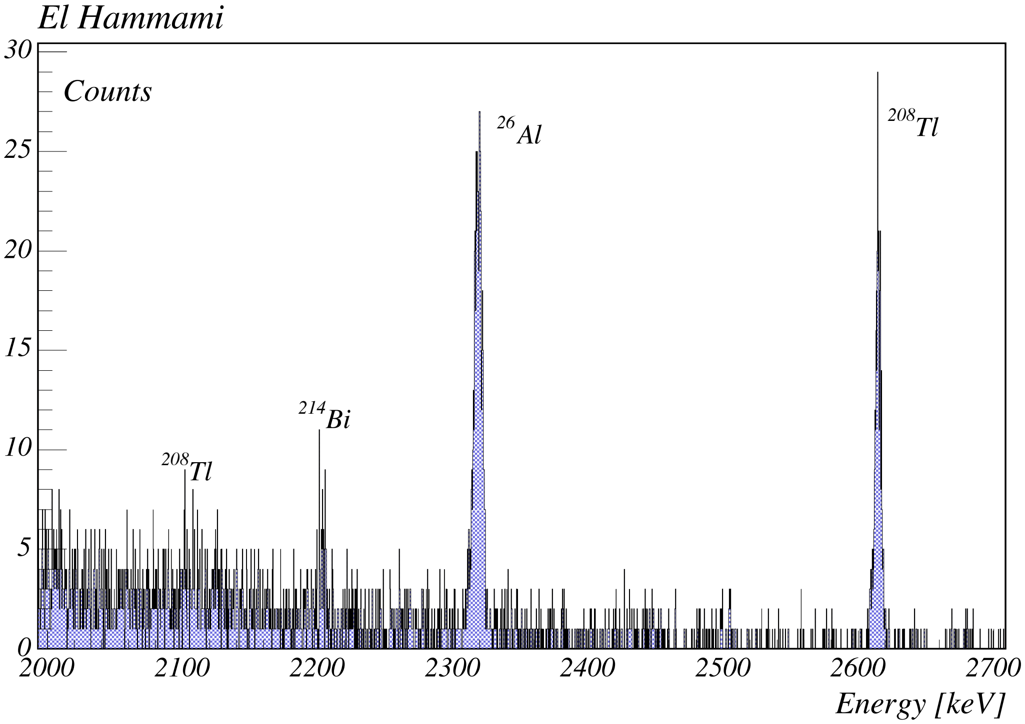

Figure 6.14: El Hammami spectrum detail : $1992 - 2650\ keV$.

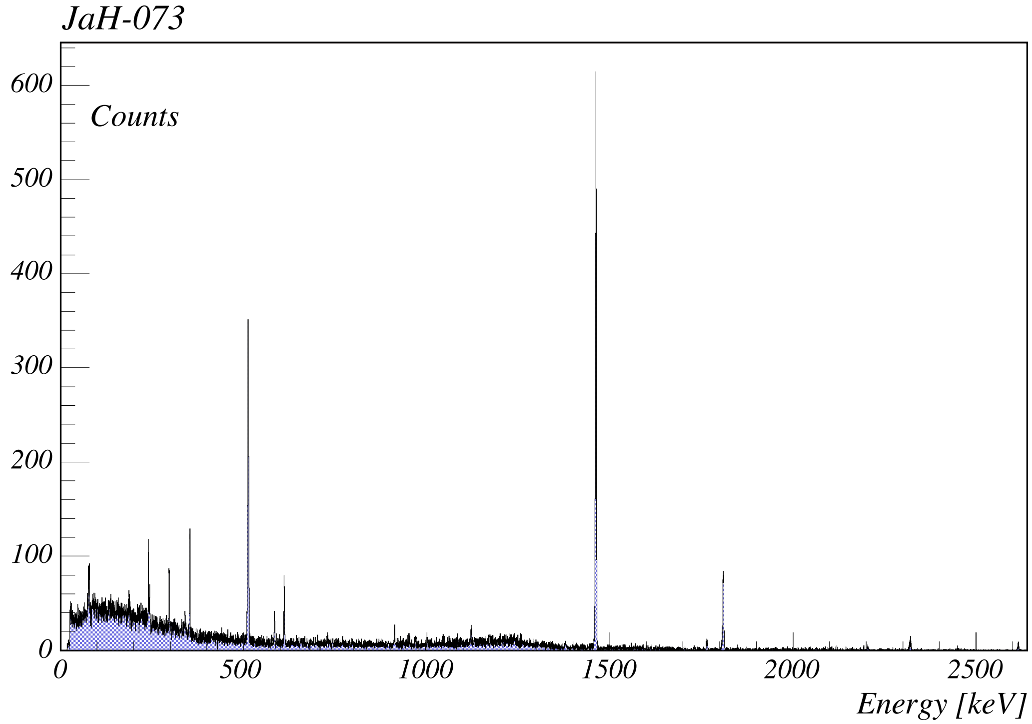

Figure 6.15: JaH-073 spectrum. This fragment of JaH-073 is identified as 0201-68.

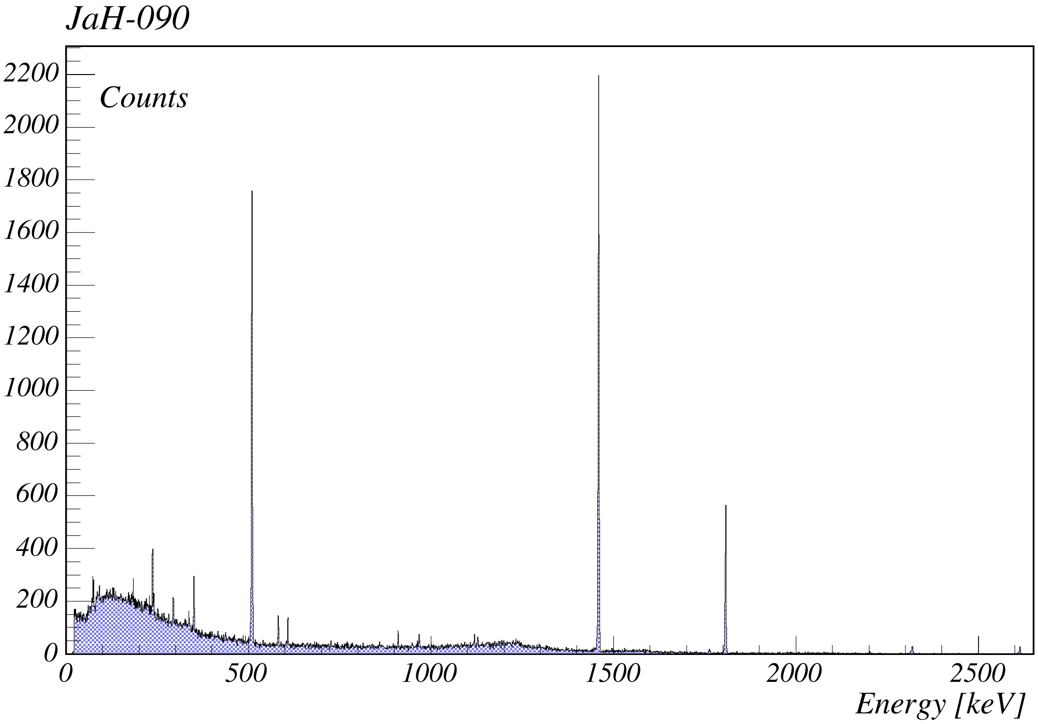

Figure 6.16: JaH-090 spectrum.

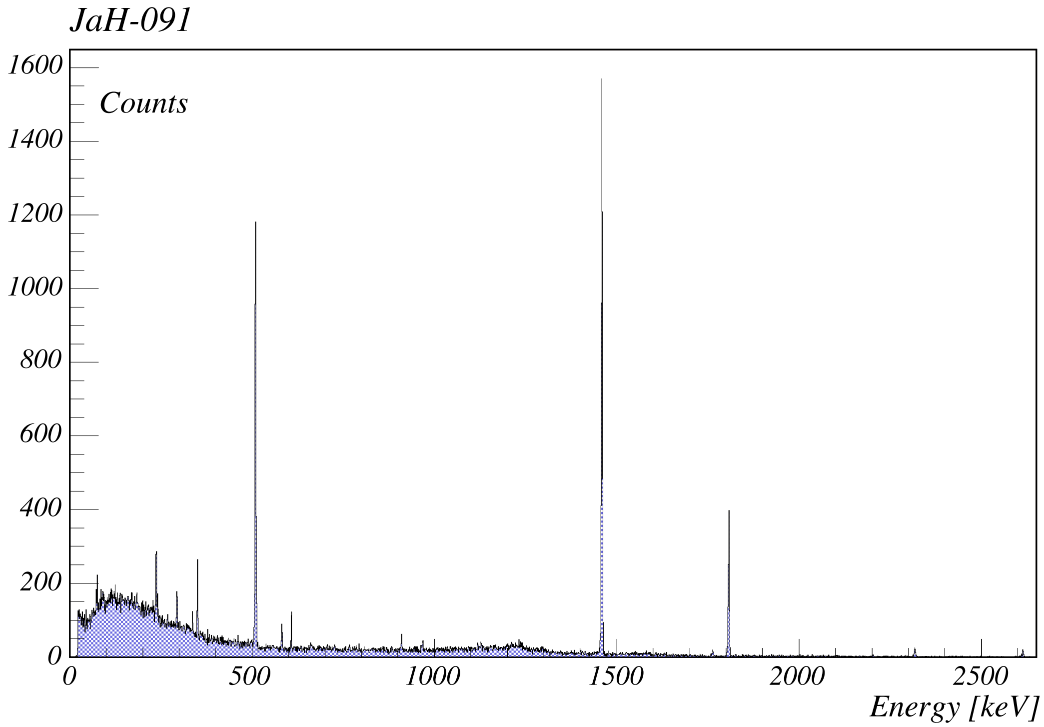

Figure 6.17: JaH-091 spectrum.

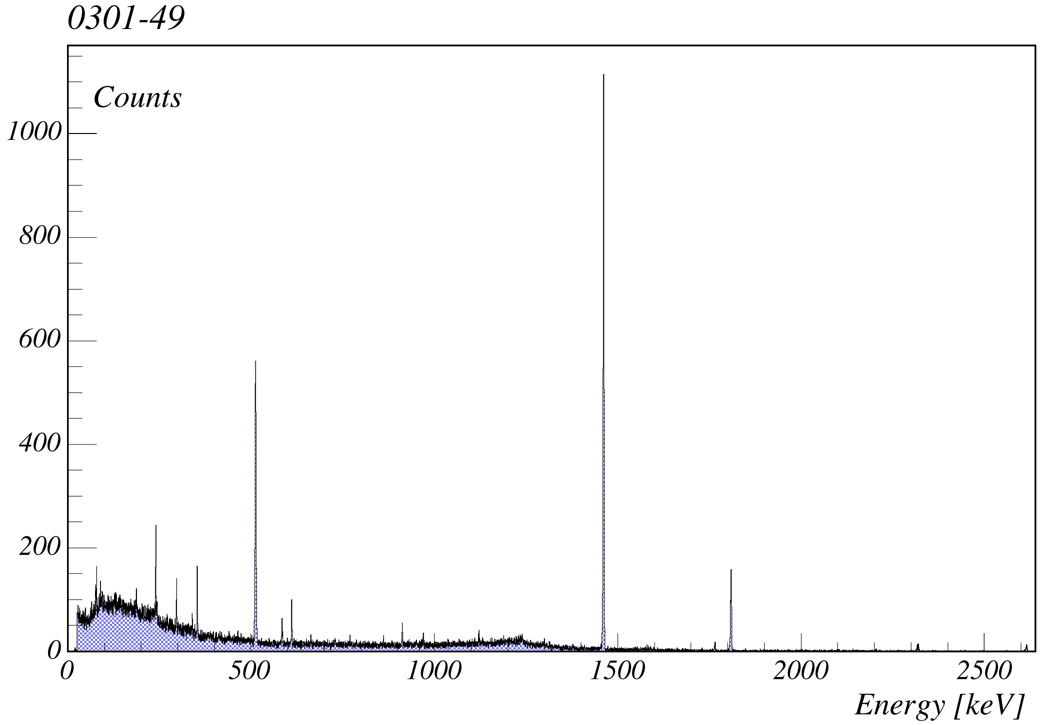

Figure 6.18: 0301-49 spectrum.

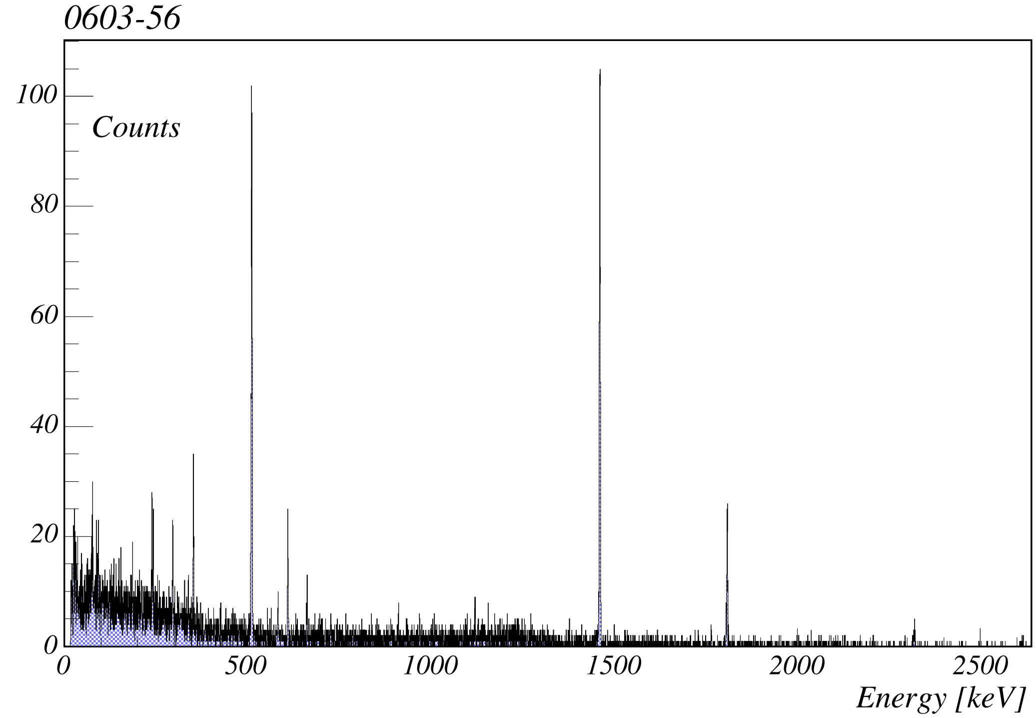

Figure 6.19: 0603-56 spectrum.

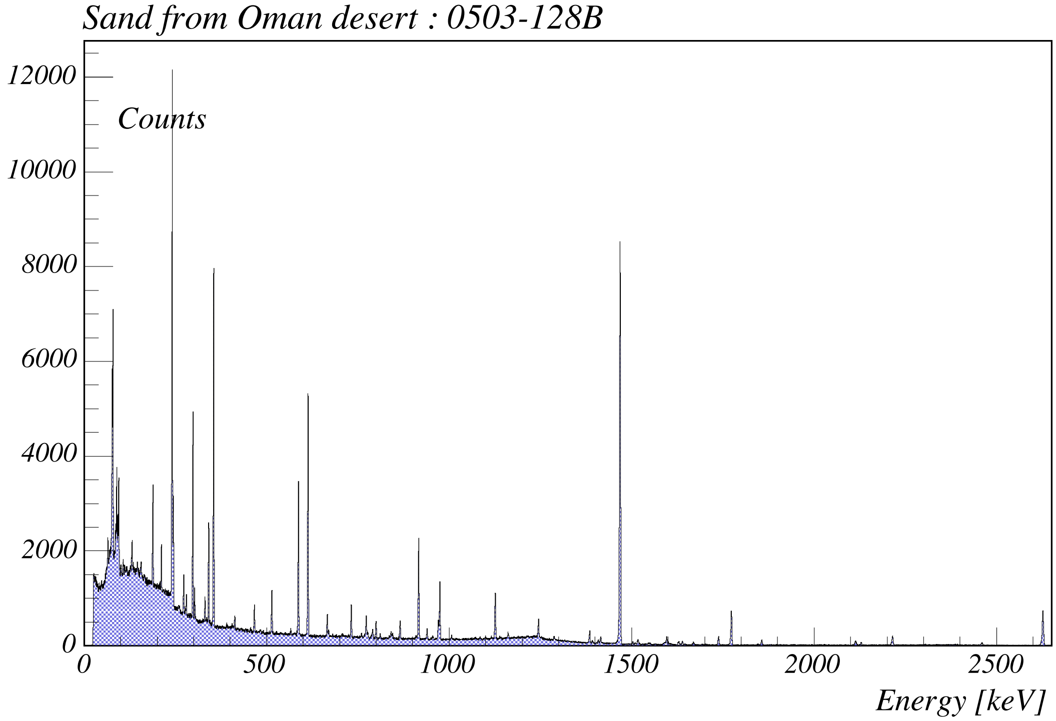

Figure 6.20: 0503-128B spectrum. Sand from the Oman desert.

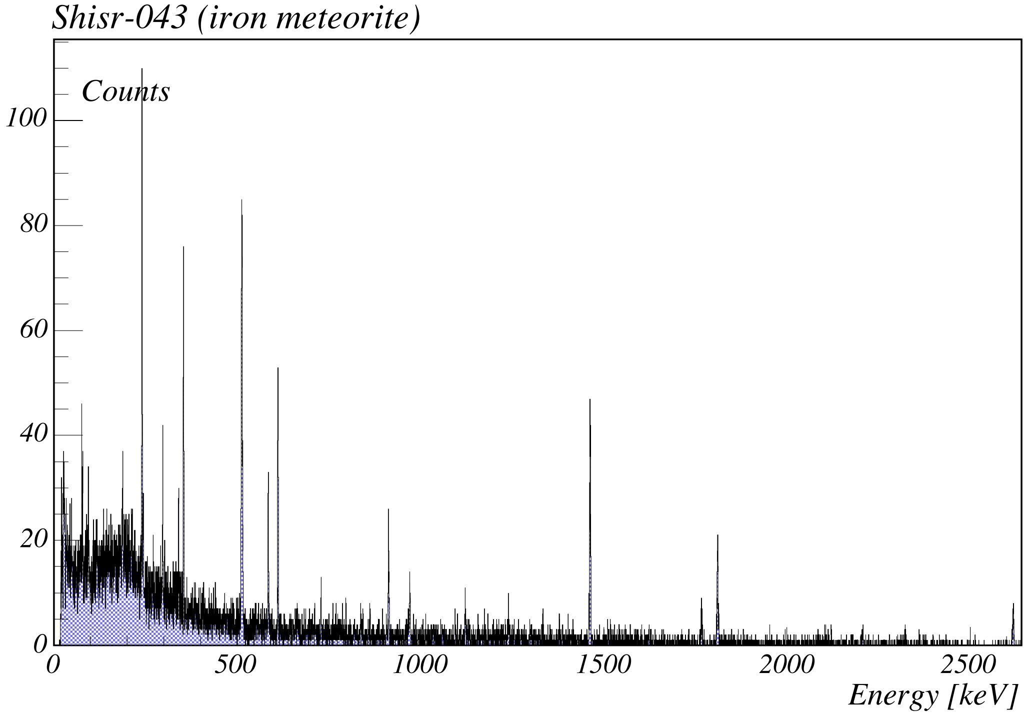

Figure 6.21: Shisr-043 spectrum. Iron meteorite.

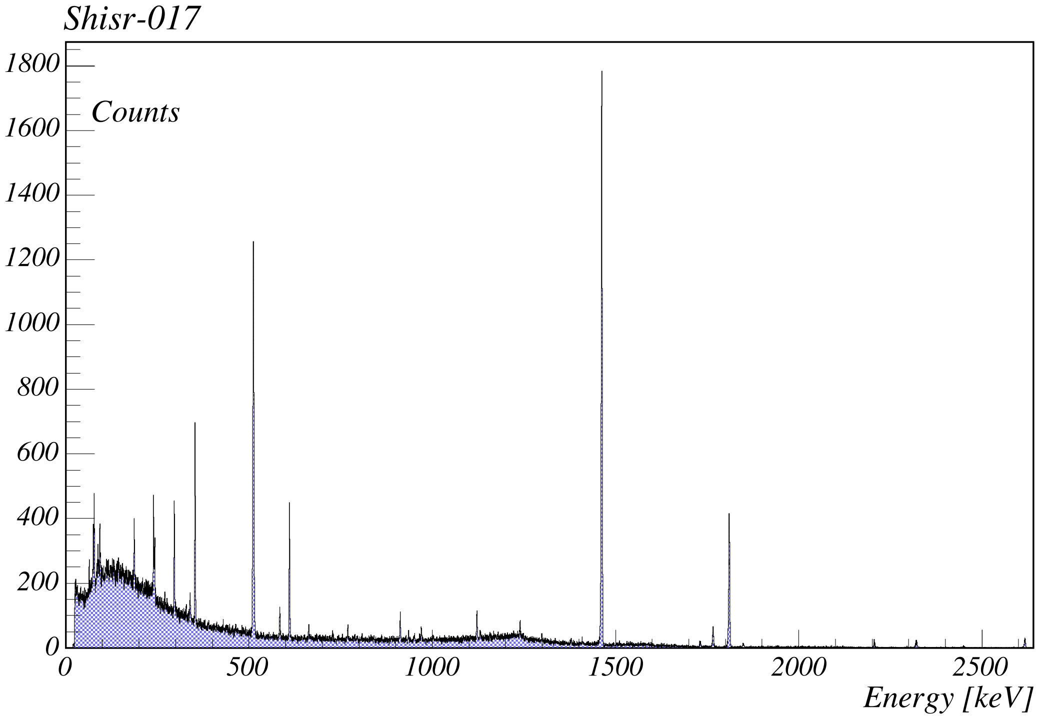

Figure 6.22: Shisr-017 spectrum.

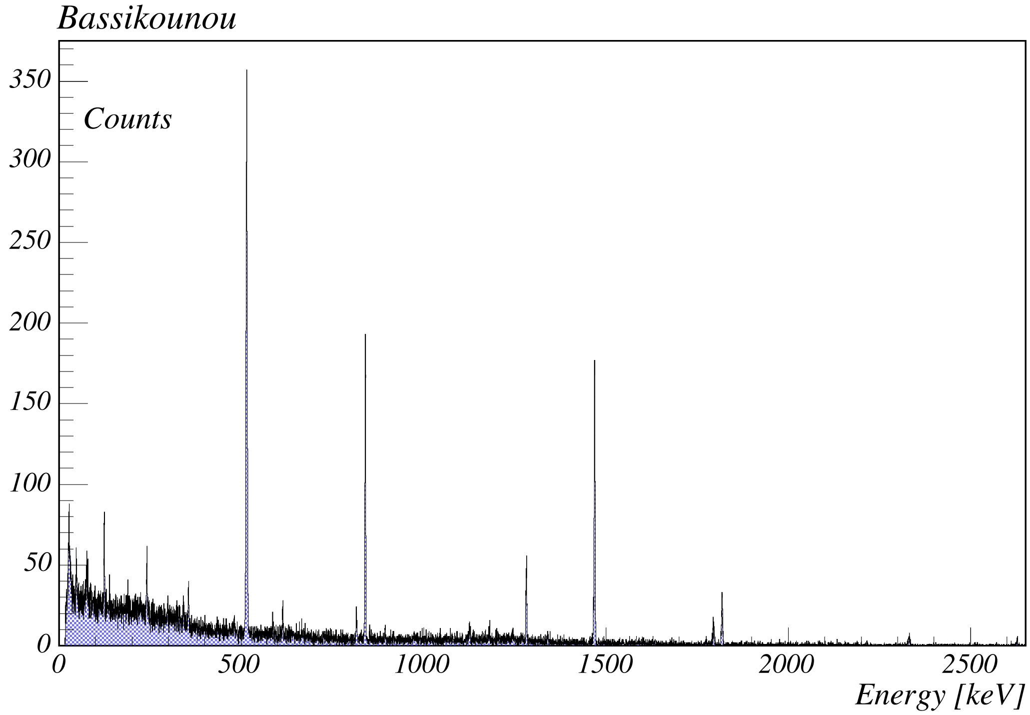

Figure 6.23: Bassikounou spectrum. Meteorite fallen on October 12, 2006.

Bibliography

[1] Harvesting meteorites in the Omani desert : Implications for astrobiology; B.A. Hofmann, E. Gnos and A. Al-Kathiri; Proc. of the III European Workshop on Exo-Astrobiology, Madrid, 10-20 Nov. 2003 (ESA-SP-545), 73-76

[2] The Omani-Swiss meteorite search project : A summary of 5 field campaigns; B.A. Hofmann, E. Gnos, A. Al-Kathiri and A.J.T Jull; Meteoritics and Planetary Science 41 (Sup), A 208 (2006)

[3] The JaH-091 strewnfield; E. Gnos, M. Eggimann, A. Al-Kathiri and B.A. Hofmann; Meteoritics and Planetary Science 41 (Sup), A 64 (2006)

[4] Aluminum-26, Sodium-22 and Cobalt-60 in two drill cores and some other samples of the Jilin chondrite, G. Heusser et al., Meteoritics and Planetary Science 31, 657-665 (1996)

[5] Itawa Bhopji (L3-5) chondrite regolith breccia : fall, classification and cosmogenic records, N. Bhandari et al, Meteoritics and Planetary Science 37, 549-563 (2002)

[6] Composition of chondrites, J.T. Wasson et al., Phil. TRans. R. Soc. Lond, A325, 535-544 (1988)

[7] Exposure histories and terrestrial ages of Antarctic meteorites; K.Welten thesis; Utrecht University

[8] The production of cosmogenic nuclides in stony meteoroids by galactic cosmic-ray particles; I.Leya et. al; Meteoritics and Planetary Science 35, 259-286 (2000)

[9] Dhingra et al; MAPS 39/8 Suppl., A121-A132 (2004)

[10] The Ordovician chondrite from Brunflo, central Sweden; B.A. Hofmann et al; III. geochemistry of terrestrial alteration. Lithos 50, 305-324 (2000)

[11] Weathering of meteorites from Oman : Correlation of chemical and mineralogical weathering proxies with 14C terrestrial ages and the influence of soil chemistry; A. Al-Kathiri, B.A. Hofmann, A.J.T Jull and E.Gnos; Meteoritics and Planetary Science 40(8), 1215-1239 (2005)

[12] Time-dependent enrichment of uranium in Oman desert chondrites; C. Stenger, U. Krhenbhl and B.A. Hofmann; Meteoritics and Planetary Science 41 (Sup), A 167 (2006)

[13] Sayh al Uhaymir 094 : A new martian meteorite from the Oman desert; E.Gnos et al.; Meteoritics and Planetary Science 37, 835-854 (2002)

[14] Chemistry of a new shergottite : Sayh al Uhaymir 005; G. Dreibus et al; Meteoritics and Planetary Science 35 (5 Suppl.), A 49 (2000)

Conclusion

The different chapters of my thesis work are directly or indirectly useful for the EXO experiment :

The barium source is an important topic in the R&D of the final version of EXO. I developed a solution that works, but not easily realizable, in the sense that the sample has to be maintained in a very clean environment — i.e under an excellent vacuum, or at least in an ultrapure atmosphere of a noble gas — and the UV laser should be coupled to a complicated setup to make the source. This work must be considered as a first approach to make a barium source and further developments would be necessary to finalize this method.

The optimization of LEM with simulation tools showed that the grid geometry leads to better gains if the ratio LEM thickness/hole diameter is bounded with the values :

$$1 \leq \frac{t}{d} \leq 2$$

The SILEM grid was designed according to these constraints, and has thus $t/d = 1.5$. It showed measurable gains up to 2 *bar* at least, with extrapolated resolutions of the order of 1% around 2 MeV, corresponding to the double-beta decay energies.
SILEM also demonstrated its abilities for track recontruction thank to its integrated $x-y$ pixel readout plane. It is now ready to measure particles crossing the TPC — such as cosmic muons — and reconstruct their tracks.
The SILEM grid could be used for large gaseous TPC's. It should be adapted to the needs of the experiment, i.e low radioactivity components, such as NOSV copper and kevlar. CERN already uses kevlar as insulator substrates for GEMs detectors. Machining of large-sized SILEM would be realizable up to 60 *cm* with "standard" photolithography techniques and large sizes have no influence on holes drilling.

It was possible to measure the secondary scintillation with optical fibers. These measurements look promising, but further developments would be needed, in order to use secondary scintillation as a complementary readout system. During the last months, a master student obtained good results with a 64 channels $x-y$ plane of optical fibers connected to a multianode PMT.

Germanium gamma analysis of more than fifty samples used for EXO-200 construction were performed. The results were very useful to the collaboration, as it allowed to select materials for building a detector with the lowest radioactive background. A simulation integrating the radioactivity of every detector part was then runned at Alabama. This led to a background of 20 $events/year$ around the $Q_{\beta\beta}$ of xenon ($\pm 2\sigma$).

The gamma analysis of meteorites was an application of low background germanium measurements. New ideas were developed and one showed some preliminary results of scientific interest, such as terrestrial age determination thank to Uranium absorption from the soil on which meteorites are lying, position of fragments in the initial meteorite, size detemination of this initial meteorite, and observations of very short-lived radioisotopes in meteorites fallen on Earth only a few weeks before the gamma measurement.

Acknowledgements

Les quelques années passées dans le groupe de physique des particules, ainsi qu'au sein de la collaboration EXO m'ont permis de participer une expérience de pointe en physique du neutrino, domaine présentement en pleine effervescence. Le travail accompli pour l'achèvement de cette thèse a été rendu possible grâce à l'aide et au soutien de nombreuses personnes que je tiens à remercier dans ces quelques lignes.

En premier lieu, je suis reconnaissant au Prof. Jean-Luc Vuilleumier de m'avoir accueilli dans son groupe et pour m'avoir donné toute l'indépendance dans la conduite de mon travail.

Je suis reconnaissant à mes collègues du groupe de physique des particules pour leur aide tout au long de ces quelques années passées à Neuchâtel, en particulier Dominique pour son aide précieuse dans la réalisations des différentes étapes de la construction de la TPC et des SILEM, ainsi que Jean-Michel pour les moments passés préparer et analyser nos échantillons lors des mesures à la Vue-des-Alpes. Merci José et Patrick J. pour les moments passés à imaginer de nouveaux détecteurs! Merci à Frédéric, Eric, Leila, Ioszef, Markus.

Je tiens également à remercier les membres du jury qui ont eu pour tâche la lecture et la correction de mon manuscrit de thèse, Roland Luescher, Frédéric Juget, Damian Twerenbold et Ralph de Voe.

Un grand merci à Beda Hofmann pour les discussions passionnantes sur les météorites.

Finalement, j'aimerais remercier mes parents ainsi que mon épouse Valérie pour son soutien tout au long de ces années faites de doutes, de joies et de peines. Nos deux enfants, Mahé, puis Capucine, sont nés durant cette période à Neuchâtel; ils sont mes plus beaux cadeaux.